Synthesis and Characterization of Vertically Aligned Single-Walled Carbon Nanotubes

垂直配向単層カーボンナノチューブ膜の合成と評価

by Erik Einarsson

A thesis presented in partial fulfillment of
the requirements for the degree of
DOCTOR OF PHILOSOPHY

東京大学大学院工学系研究科機械工学専攻

Department of Mechanical Engineering
The University of Tokyo

Dec. 2006

To my mother, to whom I owe everything,

to Dick, for teaching me the true meaning of "tenacity",

and to Kayo, for helping me find the river.

Contents

This thesis entitled "Synthesis and Characterization of Vertically Aligned Single-Walled Carbon Nanotubes", submitted by Erik Einarsson, is approved by the undersigned members of this committee.

Shigeo Maruyama

Prof. Shigeo Maruyama Thesis Adviser & Committee Chair
Dept. of Mechanical Engineering, The University of Tokyo

Prof. Takahisa Kato
Dept. of Mechanical Engineering, The University of Tokyo

Prof. Yuichi Ikuhara
Dept. of Materials Engineering, The University of Tokyo

Prof. Tatsuya Okubo
Dept. of Chemical Synthesis, The University of Tokyo

Shu Takagi

Assoc. Prof. Shu Takagi
Dept. of Mechanical Engineering, The University of Tokyo

Publications resulting from this research

Research conducted during the course of this PhD has been presented at several academic conferences, and has been published in the following peer-reviewed journal articles:

> Paulo T. Araujo, Stephen K. Doorn, Svetlana Kilina, Sergei Tretiak, **Erik Einarsson**, Shigeo Maruyama, Helio Chacham, Marcos A. Pimenta, Ado Jorio.
> "Third and fourth optical transitions in semiconducting carbon nanotubes"
> *P*hys. Rev. Lett. **98** (2006) 067401.
>
> Shohei Chiashi, Yoichi Murakami, Yuhei Miyauchi, **Erik Einarsson**, Shigeo Maruyama
> "Single-walled carbon nanotube generation by laser-heated ACCVD method" (in Japanese)
> *T*herm. Sci. Eng. **14** (2006) 61.
>
> **Erik Einarsson**, Yoichi Murakami, Masayuki Kadowaki, Hai M. Duong, Mitsuru Inoue, Shigeo Maruyama
> "Production and applications of vertically aligned single-walled carbon nanotubes"
> *T*herm. Sci. Eng. **14** (2006) 47.
>
> Yoichi Murakami, **Erik Einarsson**, Tadao Edamura, Shigeo Maruyama
> "Polarization dependent optical absorption properties of single-walled carbon nanotubes and methodology for the evaluation of their morphology"
> Carbon **43** (2005) 2664.
>
> Yoichi Murakami, **Erik Einarsson**, Tadao Edamura, Shigeo Maruyama
> "Optical absorption properties of single-walled carbon nanotubes"
> *T*herm. Sci. Eng. **13** (2005) 19.
>
> Yoichi Murakami, **Erik Einarsson**, Tadao Edamura, Shigeo Maruyama
> "Polarization dependence of the optical absorption of single-walled carbon nanotubes"
> *P*hys. Rev. Lett. **94** (2005) 087402.
>
> Shigeo Maruyama, **Erik Einarsson**, Yoichi Murakami, Tadao Edamura
> "Growth process of vertically aligned single-walled carbon nanotubes"
> Chem. Phys. Lett. **403** (2005) 320.
>
> Yoichi Murakami, Shohei Chiashi, **Erik Einarsson**, Shigeo Maruyama
> "Polarization dependence of resonant Raman scatterings from vertically aligned SWNT films"
> *P*hys. Rev. B **71** (2005) 085403.
>
> **Erik Einarsson**, Tadao Edamura, Yoichi Murakami, Yasuhiro Igarashi, Shigeo Maruyama
> "A growth mechanism for vertically aligned single-walled carbon nanotubes"
> *T*herm. Sci. Eng. **12** (2004) 77.

More recent results have yet to be published, but the following manuscripts have been or will be submitted for publication:

Erik Einarsson, Hidetsugu Shiozawa, Christian Kramberger, Mark H. Ruemmeli, Alex Grüneis, Thomas Pichler, Shigeo Maruyama
"Minimal bundling of vertically aligned single-walled carbon nanotubes and the effect on electronic properties"
*t*o be submitted

Erik Einarsson, Yoichi Murakami, Masayuki Kadowaki, Shigeo Maruyama
"An analytical growth model for vertically aligned single-walled carbon nanotubes"
*t*o be submitted

Yong-Won Song, Shinji Yamashita, **Erik Einarsson**, Shigeo Maruyama
"All-fiber pulsed lasers passively mode-locked by Transferable vertically aligned carbon nanotube film"
*s*ubmitted

Acknowledgments

First and foremost, I am very grateful for the generous funding from the Japanese Ministry of Education (Monbukagakusho) research scholarship, which made this PhD possible. Much of this research was also supported by funding from KAKENHI and the 21^{st} Century COE program, which allowed me to present results of this research at a number of domestic and international conferences.

I am very lucky to have had the chance to study in Professor Maruyama's group, and am very glad he accepted me as a research student. He has taught me too many things to begin to list here, and I thank him for his patience and understanding. I am also very grateful to Y. Murakami, who mentored me and taught me many things about being a researcher. Several other members of our laboratory have also been very good to me during these three years, and I'm glad they are both fellow researchers and friends. I am grateful to J. Shiomi and S. Chiashi for their guidance on several occasions, as well as T. Edamura, K. Miyake, M. Kadowaki, Y. Miyauchi, Zhengyi, Hai, Kei-san . . . thank you all.

There are many others with whom I collaborated on some of the work presented here, and I would like to thank them as well. In particular, T. Pichler, H. Shiozawa, C. Kramberger, A. Grüneis, M. Ruemmeli, and everyone at IFW Dresden and BESSY for their efforts. Also, H. Tsunakawa, S. Ohtsuka, and the staff at the electron microscope facility here at the Univ. of Tokyo contributed on many occasions to this research, as well as M. Sunose at Seki Technotron. I also thank T. Nishii and J. Masuyama at J-Power. Lastly, I thank the members of my thesis committee – T. Kato, Y. Ikuhara, T. Okubo, and S. Takagi – for their time and valued feedback.

Chapter 1

Introduction

1.1 Organization

This thesis begins with a brief introduction to single-walled carbon nanotubes (SWNTs), followed by a discussion of some of the physical properties of SWNTs. This will provide the foundation upon which the results presented later will be based. After the general introduction, some general techniques for characterizing and evaluating SWNTs are introduced, which will be referenced throughout this work. The history of SWNT synthesis from alcohol and the first production of vertically aligned SWNTs are then presented.

Results of the research conducted during this PhD are presented beginning in Chapter 5, which discusses the investigation of the growth process of vertically aligned (VA-)SWNT films. This study is largely based on a new method developed to measure the VA-SWNT film thickness during growth using a simple optical absorption measurement. The findings are used to develop an analytical description of the growth process. This is followed by an investigation of the optical and electronic properties of vertically aligned SWNT films. Lastly, minimal bundling of SWNTs within the vertically aligned films was indicated by electron and optical spectroscopy measurements. This was confirmed by transmission electron microscope (TEM) observation along the alignment direction of the vertically aligned SWNT films.

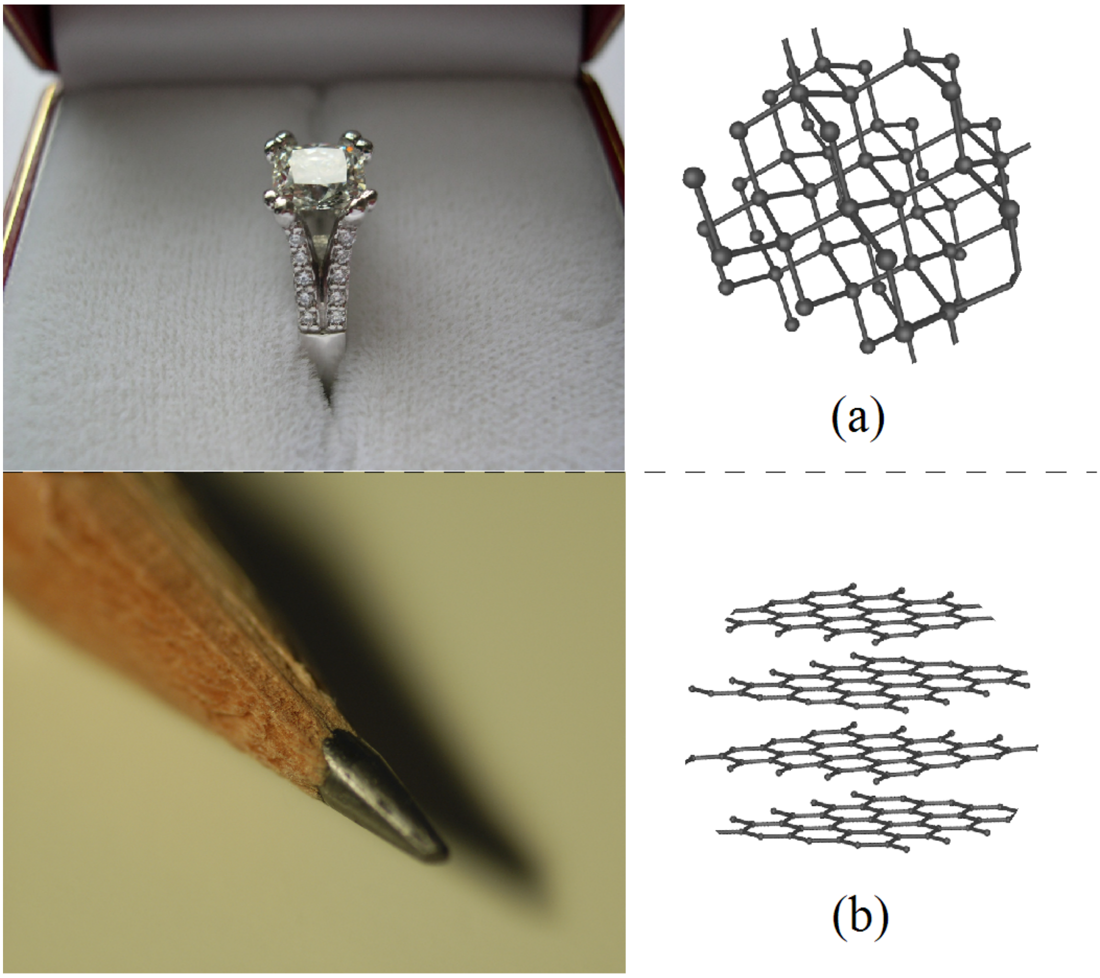

Figure 1.1: The two most well-known forms of carbon, (a) diamond and (b) graphite. (Images used with permission under the Creative Commons license.)

1.2 The many forms of carbon

Carbon can take on many forms, the most well-known being graphite – commonly found in the cores of pencils – and diamond – commonly found on engagement rings. These are the two bulk forms of carbon, illustrated in Fig. 1.1. In diamond (a), each atom shares a bond with every neighboring atom, forming a tetrahedral structure. Graphite (b), on the other hand, has a layered, planar structure. Each stacked layer comprising bulk (3D) graphite can be treated as a weakly-interacting 2D form of graphite, called *graphene*.

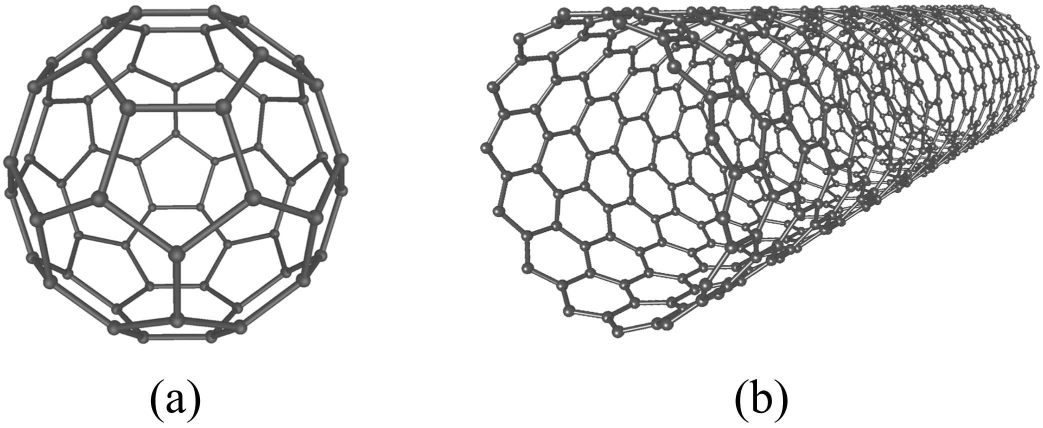

Figure 1.2: Two lesser-known, recently discovered forms of carbon, (a) C_{60} or the "buckyball", and (b) a single-walled carbon nanotube (SWNT). (Images used with permission under the Creative Commons license.)

In addition to these two forms, a new allotrope of carbon, called a fullerene, was discovered in 1985 by Robert F. Curl, Sir Harold W. Kroto, and Richard E. Smalley [1], a breakthrough for which they were awarded the Nobel prize in chemistry in 1996. The most well-known of these fullerenes is the "buckyball", or C_{60}, and is shown in Fig. 1.2a. Due to its spherical symmetry and small size (consisting of only a few dozen atoms), it is essentially a zero-dimensional (0D) material, also known as a quantum dot. With the discovery of fullerenes, members of the carbon family included the 3D forms of diamond and graphite, 2D graphene, and 0D fullerenes. So what about a one-dimensional material? One can imagine forming a 1D carbon allotrope (Fig. 1.2b) by either elongating a buckyball, or by rolling up a 2D graphene sheet into a narrow, tubular structure. This is exactly the structure discovered in 1993 [2, 3], and is known as a single-walled carbon nanotube (SWNT). In fact, both single- and multi-walled forms [4, 5] of this material exist, but the physical properties of SWNTs have proved to be much more interesting, and will be addressed in the following chapter. The properties of these new materials were intriguing enough to spawn an entire new field called nanotechnology, attracting researchers from almost all scientific disciplines.

Chapter 2

SWNT fundamentals

A carbon nanotube is exactly what its name implies, a nano-sized tubular structure made of carbon. The prefix *nano* is used because the diameter is on the nanometer scale (1 nm = 10^{-9} m). Nanotubes are categorized by the number of atomic layers contained in their walls. A single-walled nanotube (SWNT) has a wall only one atomic layer thick, and is the class of nanotubes discussed here. Nanotubes whose walls are many atomic layers thick are called multi-walled nanotubes (MWNTs). There is also a special class of MWNTs called double-walled nanotubes (DWNTs), which have properties similar to SWNTs. Despite such a small diameter, the length of a SWNT is many orders of magnitude larger (currently up to several cm long), thus a SWNT is effectively a one-dimensional object (Fig. 2.1).

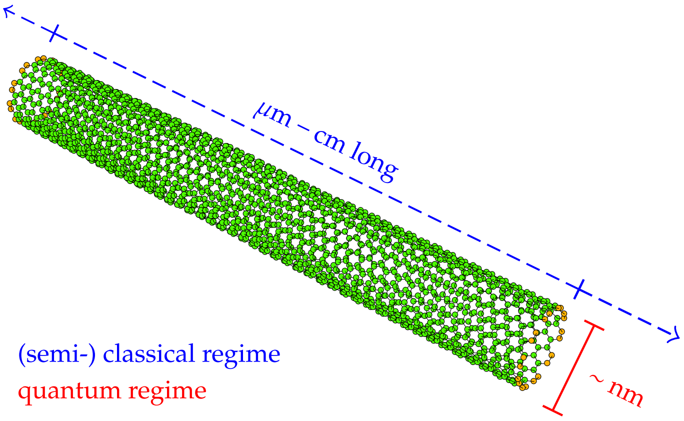

Figure 2.1: The dimensions of a SWNT (to order of magnitude).

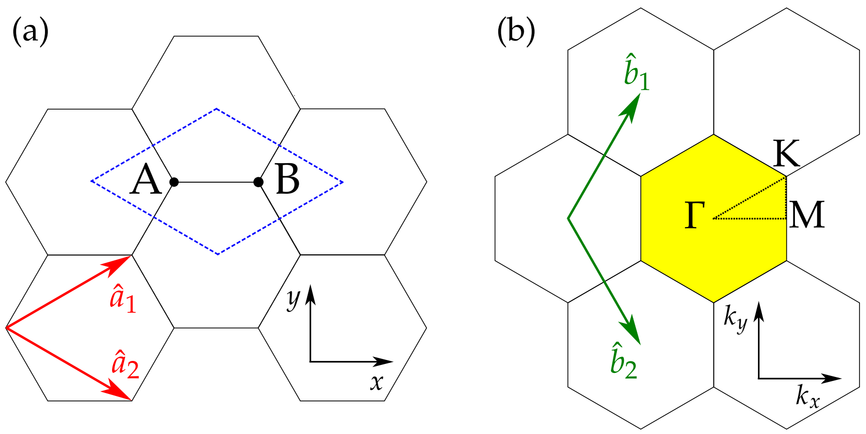

Figure 2.2: (a) The unit cell of graphene (enclosed by the dashed rhombus) contains two atoms A and B. (b) The Brillouin zone (yellow region), and high symmetry points M, K, and Γ. The real- and reciprocal-space unit vectors are shown by $\hat{a}_i$ and $\hat{b}_i$ ($i = 1, 2$).

SWNTs have many exceptional properties that arise from their unique structure. The diameter of a SWNT is small enough that quantum effects become significant, however the length of a SWNT is macroscopic in scale, making quantum effects negligible along the nanotube. This combination of length scales gives SWNTs some very interesting properties, some of which are described here. Before looking at the ways in which the electronic properties of SWNTs are affected by their low dimensionality, it is useful to present a formal description of the structure of a SWNT. As a note, most of this material in this chapter can be found in comprehensive texts such as [6, 7, 8].

2.1 Geometry of a single-walled carbon nanotube

Just as bulk (3D) graphite can be thought of as the parent material of graphene (2D graphite), in turn graphene can be considered the parent material of a SWNT. Hence, it is natural to begin a formal description of the structure of a SWNT by describing the basic structure of graphene. In the last chapter I loosely described the structure of a SWNT as a rolled-up sheet of graphene. This simple description is in fact the basis on which the nanotube structure is formally described, as is shown below.

Graphene has a hexagonal structure based on the unit cell shown in Fig. 2.2a. The basis vectors that span this hexagonal lattice space are shown in the figure by the unit

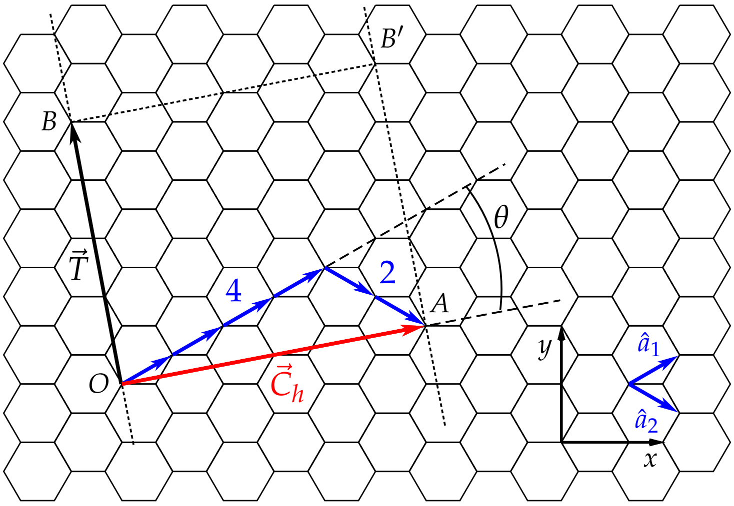

Figure 2.3: The chiral vector $\vec{C}_h$ for an (n, m) = (4,2) SWNT. The chiral angle is shown by θ.

vectors $\hat{a}_1$ and $\hat{a}_2$. In Cartesian coordinates, the x, y components of these unit vectors are

$$\hat{a}_1 = \left(\frac{\sqrt{3}}{2}a, \frac{a}{2}\right) \qquad \hat{a}_2 = \left(\frac{\sqrt{3}}{2}a, -\frac{a}{2}\right), \tag{2.1}$$

where $|\hat{a}_1| = |\hat{a}_2| = a = \sqrt{3}a_{cc}$, where a_{cc} = 1.42 Å is the distance between neighboring carbon atoms. The first Brillouin zone (BZ) of graphene is shown in Fig. 2.2b. This is the momentum space reciprocal lattice, and is spanned by the reciprocal space basis vectors $\hat{b}_1$ and $\hat{b}_2$, which are defined as

$$\hat{b}_1 = \left(\frac{2\pi}{\sqrt{3}a}, \frac{2\pi}{a}\right) \qquad \hat{b}_2 = \left(\frac{2\pi}{\sqrt{3}a}, -\frac{2\pi}{a}\right). \tag{2.2}$$

Let us now imagine rolling-up a graphene sheet into a SWNT. The structure of the SWNT can be completely described by the vector that describes the rolling direction. This vector, shown in Fig. 2.2, is called the *chiral vector*, $\vec{\mathrm{C}}_{\mathrm{h}}$, and is expressed in terms of the real space unit vectors as $n\hat{a}_1 + m\hat{a}_2 \equiv (n, m)$, where n and m are positive integers, and $n \geq m$. The angle θ that $\vec{\mathrm{C}}_{\mathrm{h}}$ makes with $\hat{a}_1$ is called the chiral angle, and for symmetry reasons $0 \leq \theta \leq \pi/6$. The diameter of the SWNT, $d_t = |\vec{C}_h| = a\sqrt{n^2 + m^2 + nm}$. The vector $\vec{T}$ in Fig. 2.2 is called the translation vector, and is the 1D unit vector of the SWNT. It is oriented parallel to the SWNT axis, and perpendicular to $\vec{C}_h$. The translation vector is defined as $\vec{T} = t_1\hat{a}_1 + t_2\hat{a}_2 \equiv (t_1, t_2)$, where

$$t_1 = \frac{2m + n}{d_R} \qquad t_2 = -\frac{2n + m}{d_R}. \tag{2.3}$$

The value d_R in equation (2.3) is the greatest common divisor (gcd) of $(2m+n)$ and $(2n+m)$. By Euclid's law[1], it turns out that

$$d_R = \begin{cases} d & \text{if } n-m \text{ is not a multiple of 3d} \\ 3d & \text{if } n-m \text{ is a multiple of 3d} \end{cases}, \tag{2.4}$$

where $d = gcd(n,m)$. The vectors $\vec{C}_h$ and $\vec{T}$ define the rectangle $OAB'B$ in Fig. 2.3, which encloses the unit cell of the SWNT. The number of hexagons in the unit cell is N, where

$$N = \frac{|\vec{C}_h \times \vec{T}|}{|\hat{a}_1 \times \hat{a}_2|} = \frac{2(m^2+n^2+nm)}{d_R}. \tag{2.5}$$

One can imagine there are many possible (n,m) combinations, giving rise to many possible SWNT structures. These structures fall into three general categories, examples of which are shown in Fig. 2.4. SWNTs have been observed using high-resolution scanning tunneling microscopy (STM) [9, 10, 11]. In the STM image shown in 2.4 (far right) the nanotube structure is easily seen, giving direct confirmation of the chiral structure described above.

---

[1] If two integers p and q ($p > q$) have a common divisor s, then s is also the gcd of $(p-q)$ and q.

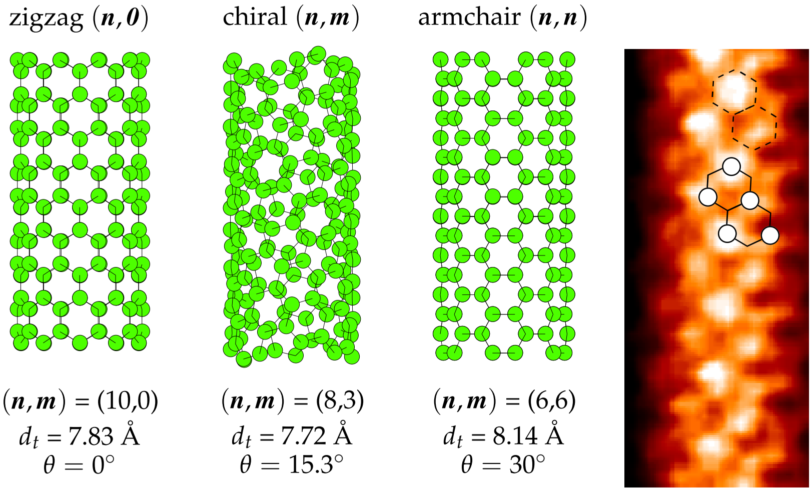

zigzag $(\boldsymbol{n},\boldsymbol{0})$ — $(\boldsymbol{n},\boldsymbol{m})$ = (10,0), d_t = 7.83 Å, $\theta = 0°$

chiral $(\boldsymbol{n},\boldsymbol{m})$ — $(\boldsymbol{n},\boldsymbol{m})$ = (8,3), d_t = 7.72 Å, $\theta = 15.3°$

armchair $(\boldsymbol{n},\boldsymbol{n})$ — $(\boldsymbol{n},\boldsymbol{m})$ = (6,6), d_t = 8.14 Å, $\theta = 30°$

Figure 2.4: Examples of the three different SWNT geometries, zigzag, chiral, and armchair. A high-resolution scanning tunneling microscope image (far right) confirming the SWNT's chiral structure (from [9]).

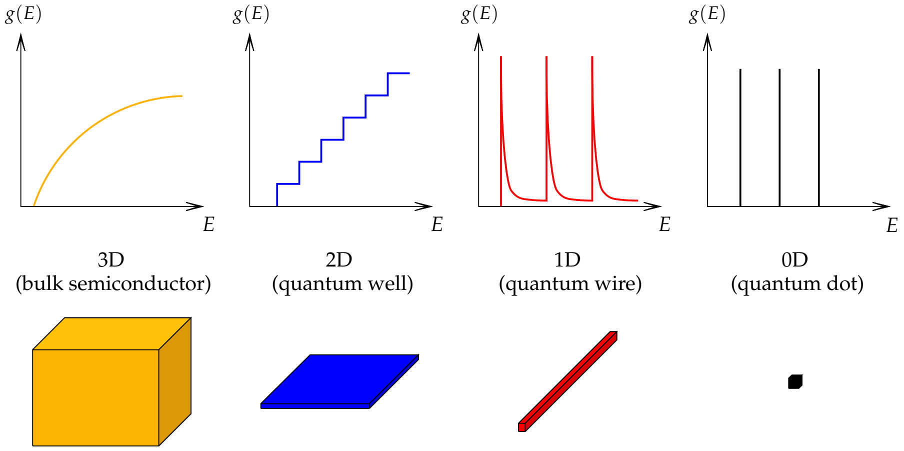

Figure 2.5: Typical density of states $g(E)$ for materials of different dimensionality. Quantum effects confine the allowed states as the dimensionality is reduced.

2.2 Electronic properties of single-walled carbon nanotubes

In bulk materials, the dimensions of the material are much larger than the constituent elements of the material. Hence, from the standpoint of the crystal lattice, the material is essentially unbound in all directions, which allows for a continuum of possible electronic states (Fig. 2.5). An example of such a system is bulk graphite. Reducing these dimensions to the scale of the lattice restricts the number of allowed states because of quantum confinement. When one of the dimensions of a material is decreased to the order of the constituent elements the dimensionality is reduced to 2 (e.g. a single atomic layer, in the case of graphene). This limits the possible electronic states, resulting in the plateaus in the density of states seen in Fig. 2.5. Further reduction to one or even zero dimensions further constrains the allowed states of a system, producing Van Hove singularities in 1D materials, and discrete energy levels in quantum dots. The 0D quantum dot is essentially the potential well model from modern physics.

The electronic properties of a material are determined by the electronic dispersion relations of the material. These can be calculated using various analytical methods, the most common of which is the tight binding approximation (Appendix A). Since many physical properties of SWNTs are very similar to those of other carbon systems, particularly graphite/graphene [7], it is often convenient to begin with the well-known properties of graphite, and then apply them to the 1D geometry of a SWNT. The energy dispersion

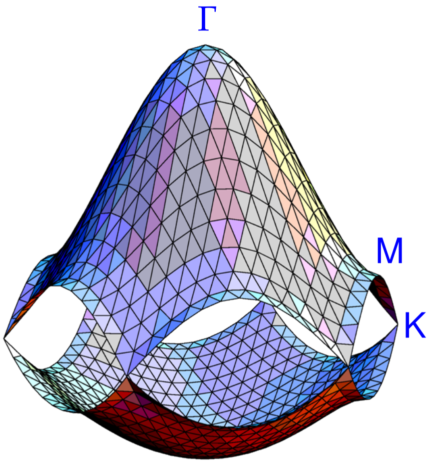

Figure 2.6: The electronic density of states (DOS) calculated over the entire Brillouin zone of graphene. The labels indicate high-symmetry points (Figure courtesy R. Saito, Tohoku University).

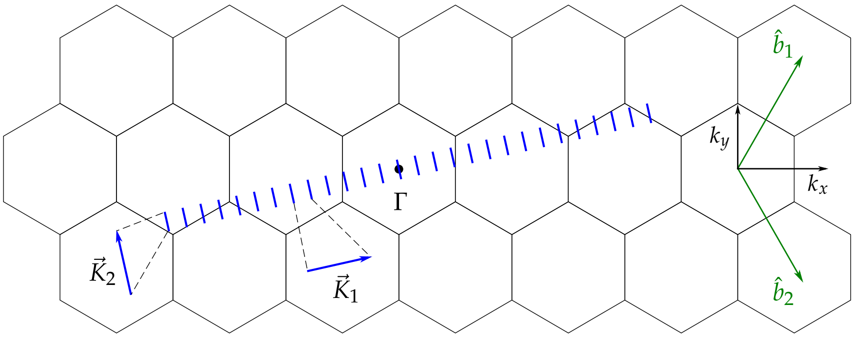

Figure 2.7: Cutting lines in the Brillouin zone for a (4,2) nanotube.

relations for graphene are shown in Fig. 2.6. These relations for graphene can be applied to the geometry of a SWNT by a technique called "zone folding" [6, 12]. Zone folding essentially maps the properties of a 2D system (e.g. the dispersion relations for graphene) to a 1D system (a SWNT). Zone-folding the electronic dispersion relations for graphene (Fig. 2.6) yields the dispersion relations for a SWNT (Fig. 2.7). The line segments in Fig. 2.7 along the reciprocal lattice vector $\vec{K}_2$ (separated by $\vec{K}_1$) are 1D Brillouin zone segments called *cutting lines*. The formation of discrete bands is a result of the periodic boundary condition around the SWNT circumference. Van Hove singularities are present in the resulting electronic DOS (Fig. 2.8), as expected for a 1D system (see Fig. 2.5).

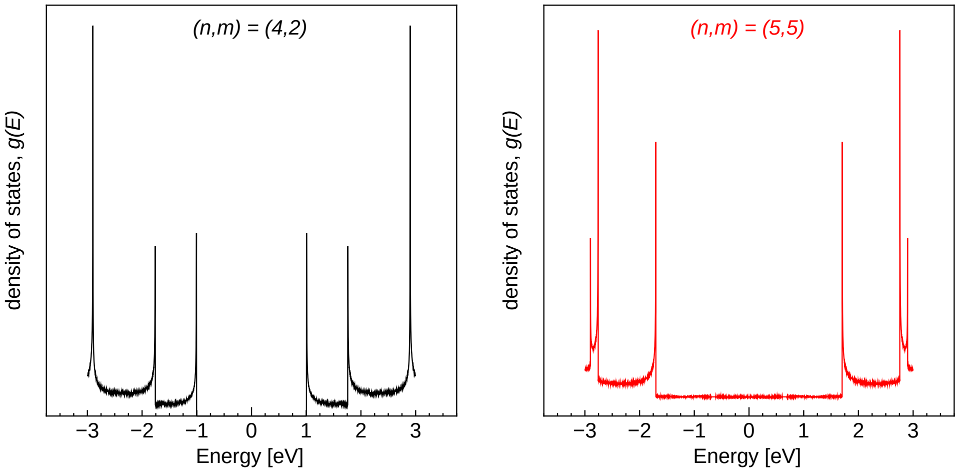

Figure 2.8: Plots of the density of states for a semiconducting (4,2) chiral SWNT, and a metallic (5,5) armchair SWNT

In Fig. 2.8, the density of states $g(E)$ at the Fermi energy is essentially zero for the (4,2) SWNT, but $g(E) > 0$ for a (5,5) SWNT. This means the (4,2) SWNT is an intrinsic semiconductor, while the (5,5) SWNT is inherently metallic. This difference is a result of the zone-folding process. In graphite, the valence and conduction bands are degenerate at the K point, where the density of states is nonzero at the Fermi level, making graphite a semi-metal (or a zero-gap semiconductor). Since the zone-folding process breaks the Brillouin zone into discrete segments, a SWNT will also be metallic if K point in contained in the DOS. This occurs when a cutting line (the 1D energy band of a SWNT) passes directly through the K point in the Brillouin zone, as is the case for the (5,5) SWNT. In the case of the (4,2) SWNT, however, the K point is not contained in the 1D dispersion relations, therefore an energy gap exists and the (4,2) SWNT is an intrinsic semiconductor. In general, all SWNTs for which $\mathrm{mod}(n-m,3) = 0$ are metallic, whereas SWNTs for which $\mathrm{mod}(n-m,3) \neq 0$ are semiconducting. This pattern is shown for various chiralities in Fig. 2.9. Other physical properties of carbon nanotubes (such as phonon dispersion relations [6, 7]) can be obtained using the same zone-folding approach.

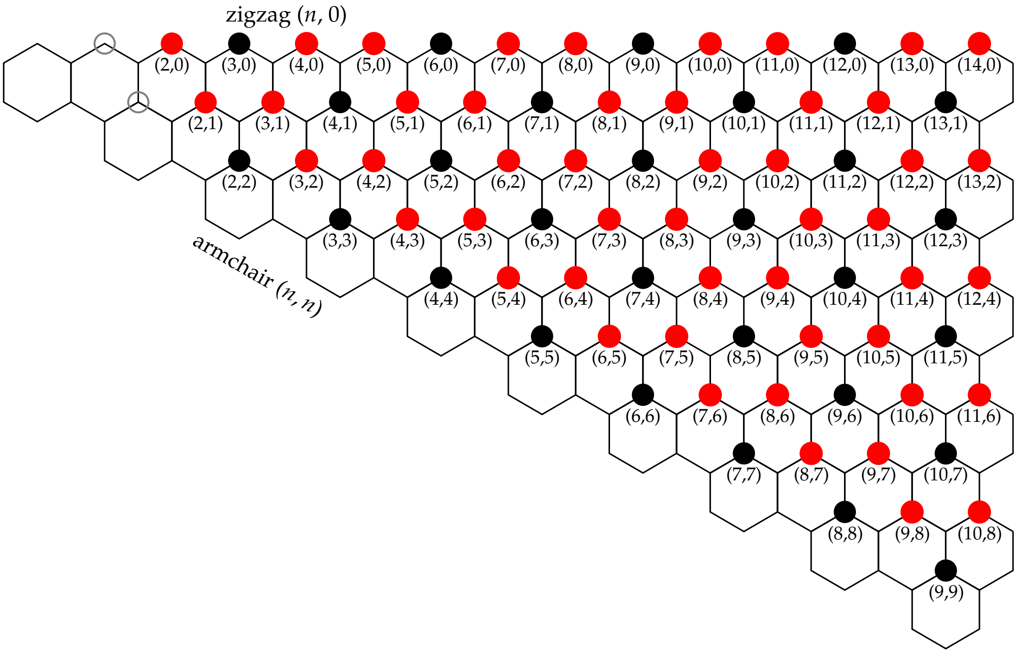

Figure 2.9: Representation of the symmetry-dependent electrical properties of SWNTs, where each dot corresponds to a specific chirality. The red dots represent semiconducting nanotubes, while the black dots are for metallic nanotubes.

Chapter 3

Characterization methods

In the previous chapter I discussed some of the physical aspects of SWNTs, and showed how the one-dimensionality of a SWNT gives rise to singularities in the electronic density of states. Since this electronic structure depends on the (n, m) of a given nanotube, experimental probes of the electronic structure can reveal much information about the diameter, chirality, and metallic or semiconducting nature of a nanotube sample. Furthermore, since optical techniques obtain information via photon interactions, they are usually very well suited for use as non-destructive characterization methods. In this chapter, I will introduce two optical spectroscopic methods commonly used to characterize SWNTs.

3.1 Optical absorption spectroscopy

3.1.1 The Beer-Lambert law

As light propagates through an absorbing medium, its intensity decreases exponentially according to the Beer-Lambert law,

$$I(L) = I_0 e^{-\alpha L c}, \tag{3.1}$$

where I_0 is the intensity of the incident light, α the absorption coefficient, L the optical path length, and c the concentration of absorbing species in the material. This is illustrated in Fig. 3.1. By measuring the transmitted intensity relative to the incident intensity, the absorbance (for a given wavelength λ) can be calculated from the following expression

$$A = -log_{10} \left(\frac{I}{I_0} \right). \tag{3.2}$$

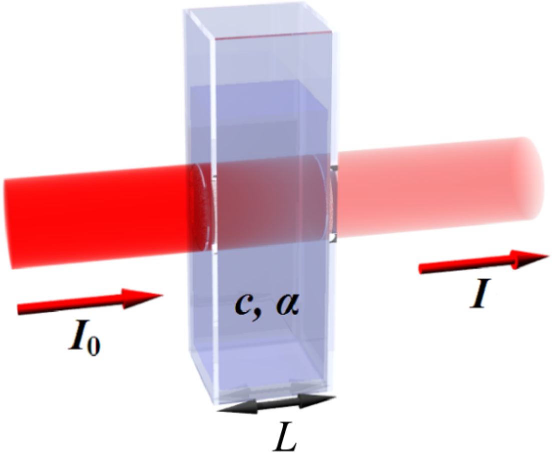

Figure 3.1: Illustration of optical absorption by a material with absorption coefficient α and concentration of absorbing species c. The optical path length is L (usually equal to the thickness or depth of the material), and I_0 and I are the incident and transmitted intensities, respectively. (Image used with permission under the GNU Free Documentation License.)

In optical absorption spectroscopy, the wavelength of the incident light is scanned through some spectral range – usually covering the ultraviolet, visible, and near infrared (UV-vis-NIR) spectral regions – throughout which the absorbance is determined using equation (3.2). Features in the resulting absorption spectrum can be mapped directly to features in the electronic states of the material, thus this technique is useful for SWNT characterization and analysis. In particular, if the incident photon energy matches the energy separation between Van Hove singularities in the SWNT density of states, the absorption probability increases dramatically, provided the transition is allowed. This will show up as a peak in the absorption spectrum. Since the DOS depends on the chirality of the SWNT, the diameter and metallic or semiconducting nature can also be determined from the peak energies, making absorption spectroscopy an important tool for SWNT characterization.

3.1.2 Interband transitions

The optical properties of a material are a direct consequence of the electronic nature of the material. As shown in the previous chapter, both metallic and semiconducting SWNTs exhibit Van Hove singularities in their electronic DOS. This results in valence and conduction band states, between which optically-induced electronic transitions can oc-

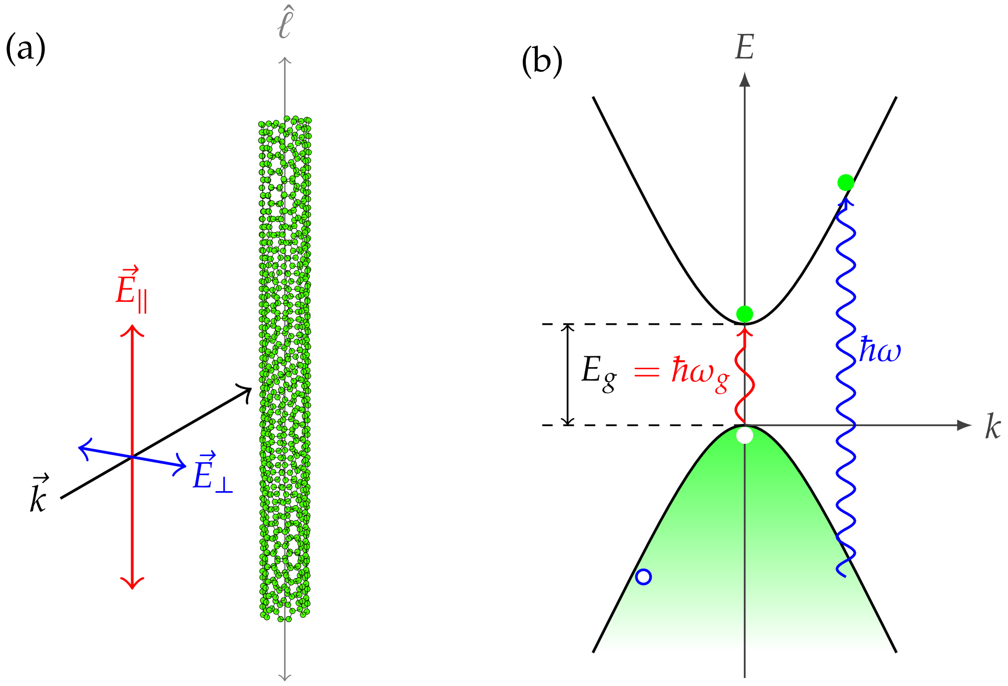

Figure 3.2: Optical absorption by a SWNT is highly anisotropic. For interband transitions, the strongest absorption occurs when the electric field vector $\vec{E}$ is polarized along the SWNT axis $\hat{\ell}$.

cur. However, the possible transitions are restricted due to symmetry considerations [13]. Due to the 1D nature of SWNTs, these optical selection rules are different depending on the polarization of the incident light with respect to the SWNT axis. The result is highly anisotropic absorption, which is strong for polarization parallel to the SWNT axis, and much weaker for perpendicular polarization (Fig. 3.2).

The allowed transitions for these two polarizations are fundamentally different processes. Given a band index μ, polarization along the SWNT axis can result in a transition from a band μ in the valence band to a corresponding band μ in the conduction band [13], such that $\Delta\mu = 0$. However, if the incident light is polarized perpendicular to the SWNT axis, the allowed transition is to a conduction band with index $\mu \pm 1$, so that $\Delta\mu = 1$. In the latter case, the transition probability is much lower than for $\Delta\mu$=0, largely due to induced depolarization effects [14]. All of these processes, however, occur for photons in the UV-vis-NIR range, which have energies of a few electron volts. These photons carry very little momentum k, thus there is essentially zero momentum transfer for these absorption processes. Transitions where $\Delta k = 0$ are called "vertical" processes because they are shown by vertical transitions in a band diagram (see Fig. 3.2b). An incident photon must have an energy greater than the band gap energy E_g to excite an electron into the conduction (upper) band. If transitions occur for energies $\hbar\omega > E_g$ (blue line), the transition is still vertical, but occurs away from the band edge (i.e. $k > 0$). In order to conserve momentum, the hole created in the valence band carries momentum of equal magnitude but opposite sign than the excited electron.

3.2 Resonant Raman spectroscopy

3.2.1 Raman scattering

Raman scattering is the *inelastic* scattering of a photon. Most scattering events are elastic (Rayleigh) processes, however, there is a small probability that a scattering event will be inelastic, exchanging energy by interacting with optical phonons. The quantum mechanical states and transitions involved in Raman scattering are shown in Fig. 3.3.

Depending on the direction of energy transfer, there are actually two possible process by which Raman scattering can occur. In both cases, the scattering process begins with an electron (and corresponding hole) in an initial state $|0\rangle$. An incident photon with energy $\hbar\omega$ excites this electron-hole pair (exciton) into a *virtual* state $|i\rangle$. Transition to this

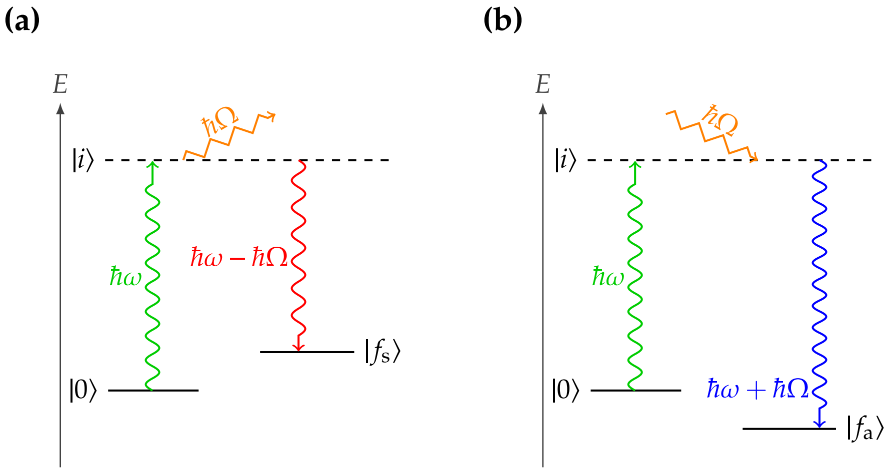

Figure 3.3: Representation of the quantum mechanical states involved in the (a) Stokes and (b) anti-Stokes Raman scattering processes (reproduction from [15]).

virtual state does not require energy be conserved. Before the electron and hole recombine and relax back to $|0\rangle$, the exciton can create or annihilate a phonon with energy $\hbar\Omega$ via the electron-phonon interaction [15]. If a phonon is created, the exciton relaxes to a final state $|f_\text{s}\rangle$, which is higher in energy than the initial state $|0\rangle$ by $\hbar\Omega$, the amount of energy carried by the phonon. This is known as the Stokes process (Fig. 3.3a). In the anti-Stokes process (Fig. 3.3b), a phonon with energy $\hbar\Omega$ that is already present in the crystal is absorbed by the exciton in the virtual state $|i\rangle$, which then recombines to a final state $|f_\text{a}\rangle$ that has a lower energy than the initial state $|0\rangle$.

In crystalline solids, wavevector must be conserved during the scattering process. This requires that $\vec{k}_i = \vec{k}_s \pm \vec{q}$, where $\vec{k}_i$ and $\vec{k}_s$ are the wavevectors of the incident and scattered light, respectively, and $\vec{q}$ is the wavevector of the phonon. This limits the scattering process to within the magnitude of $\vec{q}$, which is nearly zero for photons in the spectral range of interest (UV-vis-NIR). Therefore, only phonons for which $q \approx 0$ (i.e. Γ-point phonons) contribute to the scattering process [16], and the energy transfer is small.

As shown in the previous chapter (Fig. 2.8), SWNTs with different chiralities have a different electronic density of states. As a result, the energy differences E_{ii} between singularities i in the valence and conduction bands are unique for every (n, m) nanotube. This plays a very important role in Raman spectroscopy of SWNTs because a strong resonance occurs when the energy of the excitation light $\hbar\omega \sim E_{ii}$. This resonant Raman effect dramatically increases the scattering probability, which gives rise to a strong peak in Raman spectra. Because of this resonance, the Raman signals detected for different excitation energies can be used to identify SWNTs of different (n, m). This makes Raman spectroscopy one of the most important optical technique for characterization of SWNTs.

3.2.2 Raman spectra

As previously mentioned, there is a small probability that an incident photon will be inelastically scattered by a material. This occurs in roughly one of every 10^7 scattering events (the rest of which are scattered by the Rayleigh process). As a result, the intensity of Raman-scattered light is very weak, so in order to obtain a decent measurement of this signal it is necessary to increase the frequency of scattering events. One way to accomplish this is to use a laser as the light source, unlike in optical absorption spectroscopy, where a lamp is sufficient. To further enhance the Raman scattered signal, the laser is focused to a

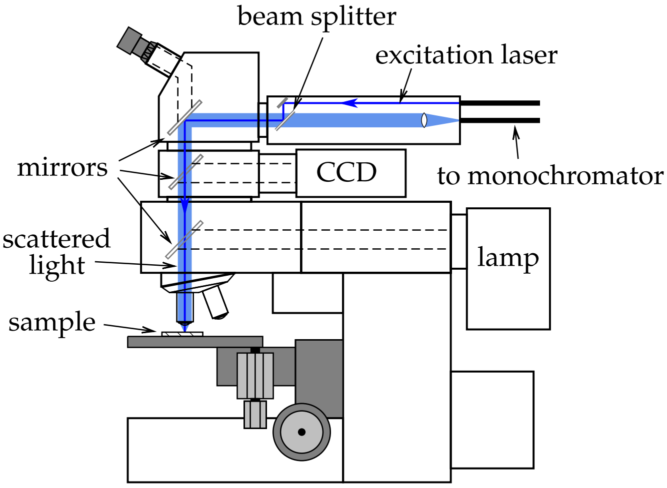

Figure 3.4: Diagram of the apparatus used for Raman scattering measurements. The scattered light is focused into an optical fiber, which sends it to a monochromator where the signal is recorded by a CCD (image modified from [17]).

small area on the sample from where the signal is measured. This is often done by passing the laser through the lenses of an optical microscope, as illustrated in Fig. 3.4. Fortunately, the microscope lens can also be used to collect the scattered light, which is sent into a monochromator and recorded by a CCD. Before entering the monochromator, the intense Rayleigh signal is filtered out by a combination of a dichroic mirror (beam splitter) and an adjustable notch filter. A typical Raman spectrum is shown in Fig. 3.5, where the Raman shift – the shift with respect to the excitation light – is plotted in inverse cm.

The dominant peak at around 1590 cm^{-1} in the Raman spectrum shown in Fig. 3.5 corresponds to a resonant excitation of in-plane optical phonons, reflecting the graphitic nature of the nanotube [18]. For this reason, this peak is called the G-band, where G stands for graphite. However, unlike graphite, the curvature of the SWNT causes the axial and transverse in-plane vibrational modes to have a slight difference in energy. These vibrations are indicated by the red and blue arrows in Fig. 3.6a. This energy difference causes the G-band peak to split into a lower energy G^- peak and a higher energy G^+ peak. Interestingly, it has been shown that the relative shift of the transverse and longitudinal modes is opposite for semiconducting and metallic SWNTs [19, 20]. The scattering process associated with the G-band excitation is a first-order process, meaning one scattering event occurs. Second-order scattering can occur when excited phonons are scattered by defects

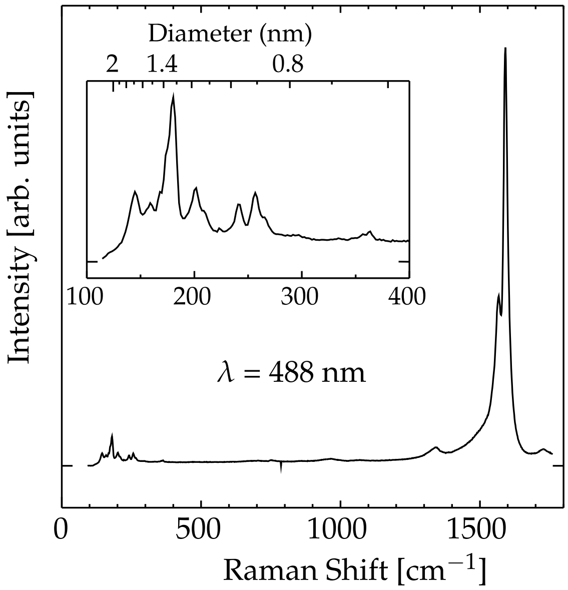

Figure 3.5: A typical Raman spectrum from vertically aligned SWNTs (488 nm excitation laser). The RBM peaks are shown in the insert. A dominant peak at 180 cm^{-1} is indicative of vertical alignment (see text).

or inconsistencies in the crystal lattice. This shows up in Raman spectra of SWNTs as a small hump near 1350 cm^{-1} called the disorder band, or D-band.

The last major feature visible in the spectrum in Fig. 3.5 is the series of peaks below 400 cm^{-1} (magnified in the insert). These peaks are from a phonon excitation that is unique to SWNTs, and contain much information about the nanotubes present in the sample. Recall that the G-band mode described above is caused by a resonant in-plane vibrational mode, which is characteristic of graphite. An out-of-plane modes also exists, where the vibration is perpendicular to the lattice plane [21]. If one imagines taking a graphene sheet supporting such an out-of-plane vibration, and rolling it into the cylindrical shape of a SWNT, the out-of-plane vibrations become oriented radially away from the SWNT axis, as shown in Fig. 3.6b. The result is a purely radial mode, where the diameter of the entire SWNT oscillates, appearing as though it were "breathing". For this reason, this mode is known as the radial breathing mode, or RBM. The RBM is also a resonant Raman mode, which is in resonance when the energy of the incident photons match an energy gap E_{ii} in the SWNT density of states. The fact that the RBM is unique to SWNTs makes Raman spectroscopy a quick and easy method to confirm the presence of SWNTs

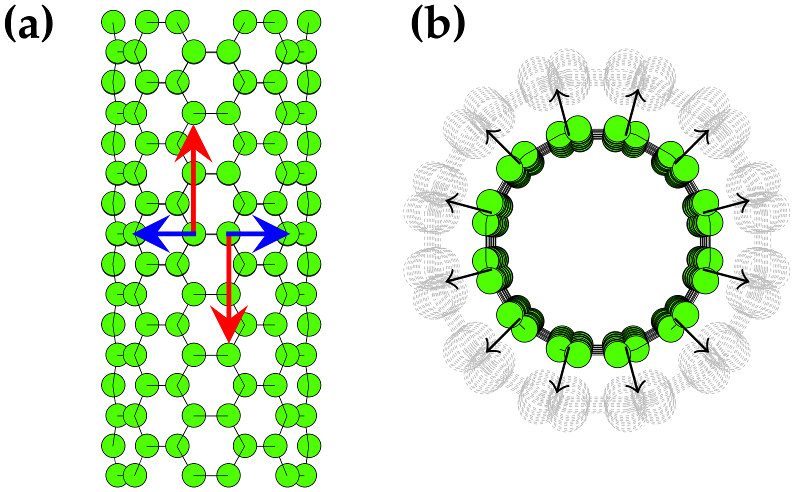

Figure 3.6: (a) the in-plane vibrational modes corresponding to the G-band Raman signal, and (b) the uniform out-of-plane vibration that gives rise to radial breathing mode (RBM) excitations.

in a sample, as well as to estimate the diameter distribution and overall sample quality. In general it is possible to detect the RBM from the inner and outer walls of a DWNT [22], but additional walls strongly dampen these radial modes.

As one might expect, the frequency of the RBM depends on the diameter of the SWNT, thus each peak in the spectrum corresponds to a SWNT of a certain diameter (note the diameter scale on the upper axis in the inset in Fig. 3.5). This diameter dependence has been thoroughly studied [23], and the experimental data shown in Fig. 3.7 show a very well-behaved relationship. Based on these data, the RBM frequency (ω_{RBM}) is related to the SWNT diameter (d_t) by the empirical equation

$$\omega_{RBM} \approx \frac{218}{d_t} + 16. \tag{3.3}$$

As seen in this equation, ω_{RBM} is roughly inversely proportional to the SWNT diameter, thus as the SWNT diameter increases, ω_{RBM} decreases. Since the region near 0 cm^{-1} is suppressed by the notch filter, it is difficult to detect RBM peaks from large-diameter SWNTs.

Using different excitation energies, RBMs of different frequencies – corresponding to different SWNTs – will be excited. This makes it possible to "map out" the diameter distribution of a sample by scanning the excitation laser through a wide energy range. Such a map is shown in Fig. 3.8.

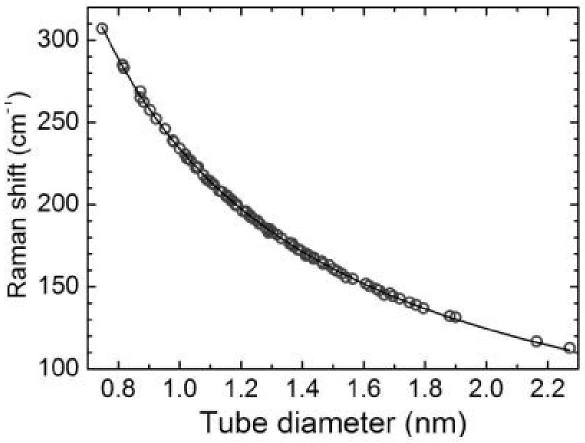

Figure 3.7: The correlation between the SWNT diameter and the RBM frequency (reproduced from [23]). This relationship is described by equation (3.3).

As with optical absorption, excitation of the RBM is also polarization dependent [24]. As a result, it has been shown by our group that polarization-dependent Raman spectroscopy can be used to obtain information about the morphology of the sample [25]. For the vertically aligned SWNTs investigated here, a strong RBM peak at 180 cm^{-1} in relation to neighboring peaks at 160 and 203 cm^{-1} is indicative of vertical alignment (for light incident normal to the substrate on which the SWNT film has been grown).

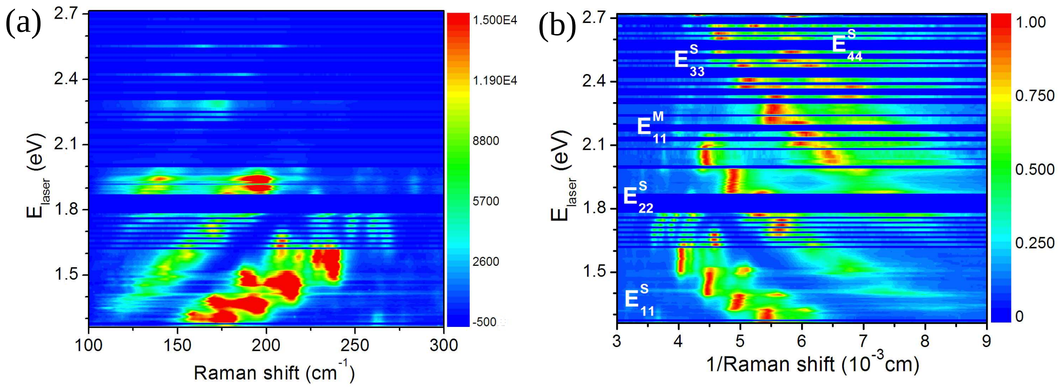

Figure 3.8: A "Raman map" showing normalized peak intensities for Raman spectra obtained using many excitation wavelengths. The (a) Raman shift and (b) inverse Raman shift are plotted vs. the excitation laser energy (reproduced from [23]).

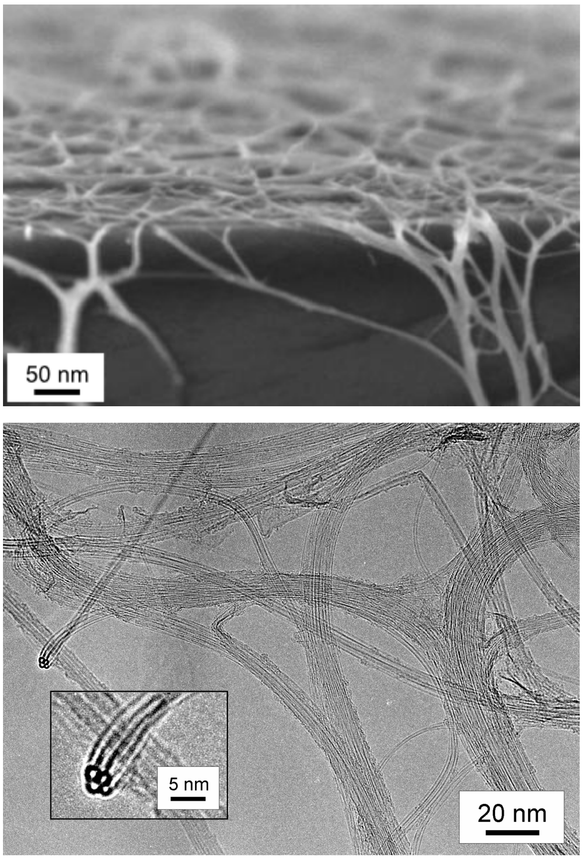

Figure 3.9: A high-resolution FE-SEM image of SWNT bundles lying on a substrate surface (left), and a TEM image of SWNT bundles (right). Individual SWNTs within a bundle can be seen in the insert.

3.3 Electron microscopy

Electron microscopy is an indispensable tool used in many areas of science. Just as the wavelike nature of light is used to produce an image in a light microscope, the wavelike nature of electrons to produce an image in an electron microscope, thereby obtaining much higher resolution (magnification exceeding 100,000X). Images are produced by scanning an electron beam over a sample in a raster pattern, and then detecting the scattered electrons. A microscope designed for this purpose is called a scanning electron microscope, or SEM. A field emission (FE-)SEM uses a field emitter to obtain an intense electron beam, which further improves the resolution. Figure 3.9(a) shows an electron micrograph of carbon nanotube bundles obtained using an FE-SEM.

In addition to the SEM there is another kind of electron microscope that is capable of even higher magnification (over 1,000,000X). This is achieved not by detecting electrons scattered by a material, but rather by detecting electrons that have passed *through* the sample. This is accomplished by accelerating the electrons to high energies (typically > 100 keV) and specially preparing the sample so that it is thin enough for the incident electrons to pass through. A microscope operating on this principle is called a transmission electron microscope, or TEM. A good TEM is capable of atomic resolution, thus gives an extremely accurate picture of the crystal structure of a material. A TEM image of SWNTs produced from alcohol [26] is shown in Fig. 3.9b. The single-layered tube walls can be made out in the image. A bundle of four SWNTs is shown in the inset. Synthesis of SWNTs from alcohol and the realization of vertically aligned growth is the subject of the following chapter.

Chapter 4

Vertically aligned SWNTs from alcohol

4.1 SWNT synthesis

In the first few years following their discovery [2, 3], highly crystalline, few-defect SWNTs could be produced by only a few methods, such as the arc discharge [27] and laser over [28] methods, but the pace of research was inhibited because SWNTs could not be produced on the scale required for most experiments. SWNT synthesis became much simpler when Hongjie Dai and coworkers at Rick Smalley's group at Rice University (the same Rick Smalley who was awarded the Nobel prize for the discovery of C_{60}) developed a method [29] by which SWNTs could be produced by chemical vapor deposition (CVD), in which the carbon source used for CVD growth was a carbon containing gas, such as CO, reacted with metal catalyst particles inside a heated reactor. This quickly became the most common SWNT production method, but the quality of the SWNTs produced varied from laboratory to laboratory.

In the late 1990s, again at Rick Smalley's group, a SWNT synthesis process called HiPco [30] was developed, by which SWNTs were synthesized by a high-pressure disproportional reaction of CO. This was the first time gram-scale quantities of SWNTs could be synthesized in a reproducible fashion. Requests for samples poured in from laboratories around the world. Many of these requests were filled, and HiPco nanotubes subsequently became the *de facto* SWNT standard, allowing direct comparison of experimental results

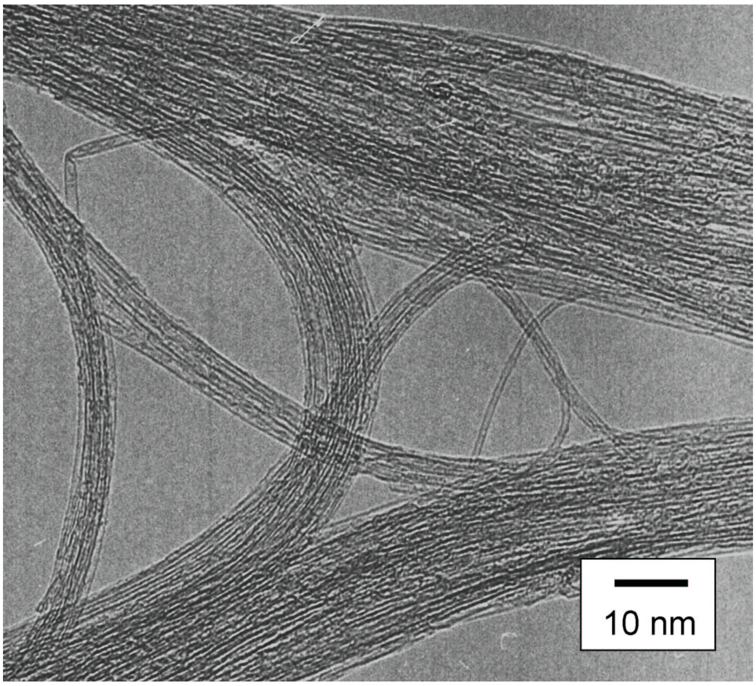

Figure 4.1: A TEM image showing bundles of high-purity SWNTs synthesized from alcohol (from [26]).

from various experiments carried out at laboratories around the world. This significantly accelerated the pace of SWNT research, and many significant advancements in the field soon followed. However, nanotechnology was still in its infancy.

One major challenge in nanotechnology is controlling the morphology of SWNTs during synthesis. Morphologically-controlled growth is critical for the realization of many proposed nanotube-based applications. A major advance in this area came in 2003, with the synthesis of vertically-aligned SWNTs [31] using an alcohol-based CVD growth process [26].

4.2 The ACCVD method

There are many SWNT production methods, each with its own advantages and disadvantages. However, one problem common to all of them is the presence of impurities, usually in the form of catalyst particles or amorphous carbon formed during SWNT synthesis. In 2002, it was reported [26] that high-purity SWNTs could be grown using alcohol

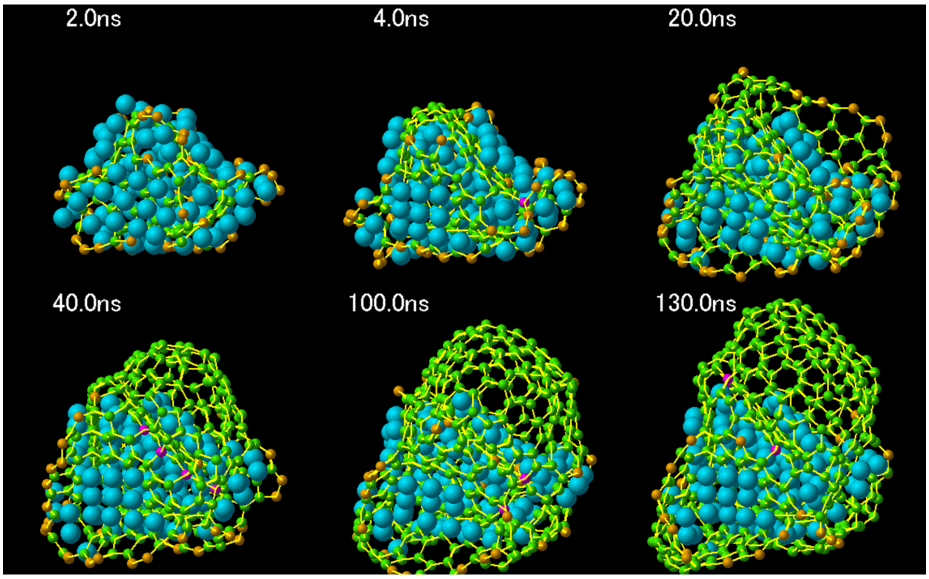

Figure 4.2: A molecular dynamics simulation showing the formation of a SWNT cap structure on a metal catalyst particle during CVD (from [33])

as the carbon feedstock gas. A TEM image of SWNTs synthesized from alcohol is shown in Fig. 4.1. This alcohol catalytic chemical vapor deposition (ACCVD) method has since become one of the most popular methods used for low-cost, high-purity SWNT synthesis. This lack of amorphous carbon was attributed to the OH radical present in alcohols, which preferentially reacts with carbon molecules that have dangling bonds. This effectively etches away those carbon atoms that are most likely to produce amorphous carbon [26, 32]. The details of the growth mechanism, however, are not yet well understood. It is known, however, that SWNT growth is a catalytic process, by which a carbon-containing molecule reacts with a metal catalyst particle and precipitates a nanotube. The general CVD process is still being investigated by many different methods, including molecular dynamics simulations such as that shown in Fig. 4.2 [33].

4.3 Achieving vertical alignment

Another significant advance in SWNT research was the synthesis of vertically aligned SWNTs [31]. This had previously been achieved using multi-walled carbon nanotubes, but SWNTs are known to form bundles, bound together by Van der Waals forces.

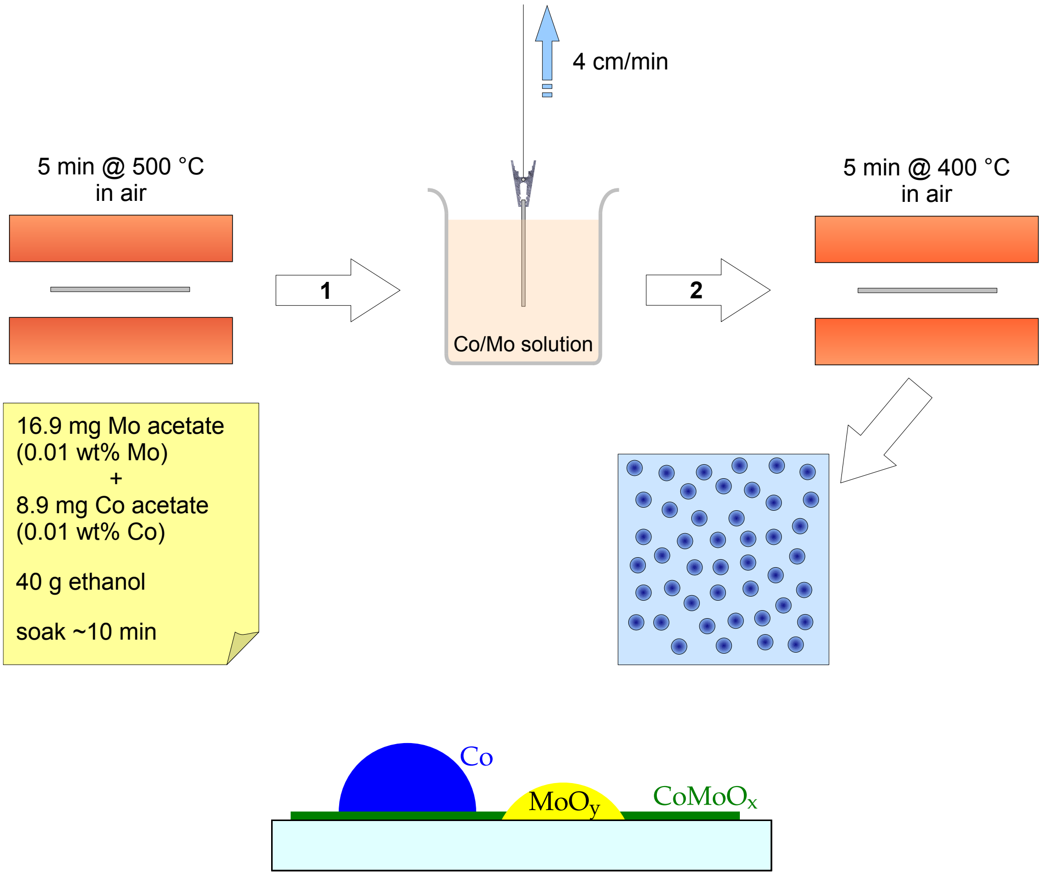

Figure 4.3: (top) A diagram of the dip-coat catalyst loading process [34] and resulting monodispersed catalyst particles, and (bottom) the chemical state of the growth surface after reduction [35].

This typically results in a tangled mess of random SWNTs, often likened to spaghetti. However, due to their one-dimensionality, many SWNT properties are anisotropic, thus control over the orientation is highly desirable for exploiting these anisotropic properties. For SWNTs, this was achieved by combining the aforementioned ACCVD method with a liquid-based catalyst loading method [34], described in the following section.

4.3.1 Catalyst loading by the dip-coat method

Catalyst loading was performed by submerging an optically polished quartz substrate into a solution containing cobalt acetate ($(CH_3CO_2)_2Co–4H_2O$) and Mo acetate ($(CH_3CO_2)_2Mo–4H_2O$) dissolved in ethanol. The amount of each metal species in the

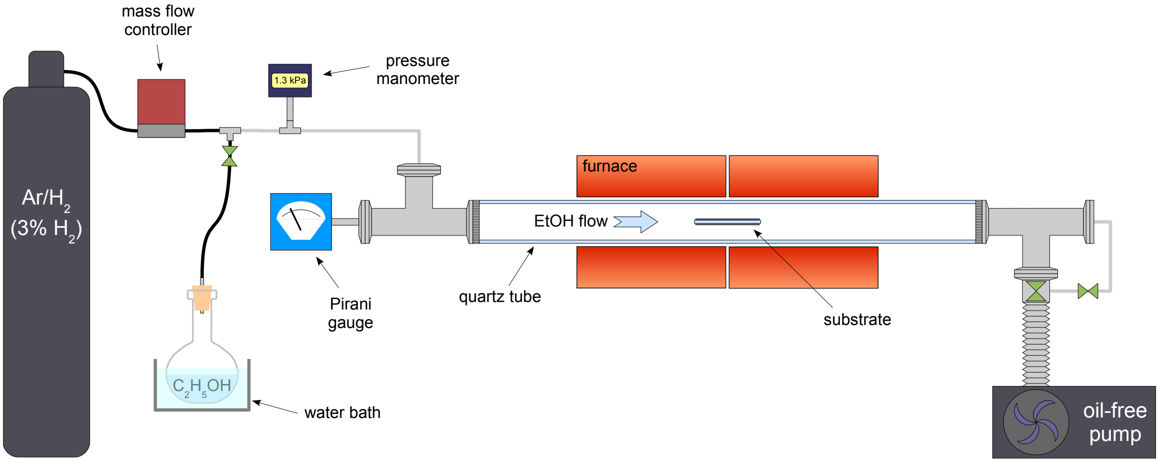

Figure 4.4: Diagram of the CVD system used to synthesize vertically aligned SWNTs.

solution was 0.01 wt.%. The substrate was immersed in the Co/Mo solution for approximately 10 minutes, then slowly withdrawn from the solution at 4 cm min^{-1} (see Fig. 4.3). The thin liquid film on the substrate surface after withdrawing from the solution contains a nearly homogeneous mixture of the dissolved metals. The dip-coated substrate is then baked in air at 400°C for 5 min to remove the acetate and oxidize the metals. Formation of this oxide fixes the catalyst in place on the substrate surface, thereby resisting agglomeration at high temperatures (e.g. 800°C). The result is densely deposited, mono-dispersed catalyst particles ($\approx 10^5$ particles per μm^2) with diameters of approximately 1.5 nm [35]. It is believed that this high catalyst density leads to vertically aligned growth. Due to the high catalyst density, the presence of SWNTs in close proximity to one another limits their lateral freedom during growth, thus they orient themselves perpendicular to the substrate and grow in an aligned fashion.

Since oxidized metals are generally catalytically inactive [36], the oxidized catalyst particles were reduced prior to SWNT growth. This was done by supplying an Ar/H_2 mixture (3% H_2, Ar balance) at a flow rate of 300 sccm and pressure of 40 kPa during heating of the CVD reaction chamber. The state of the catalyst after this reduction is shown at the bottom of Fig. 4.3. After reaching the growth temperature (650-850 °C), the Ar/H_2 mixture was stopped and ethanol vapor (99.5% dehydrated ethanol) was introduced to initiate SWNT growth. For our system, shown in Fig. 4.4, the alcohol pressures at the inlet and inside the growth chamber during SWNT synthesis were 1.3 and 0.6 kPa, respectively. The

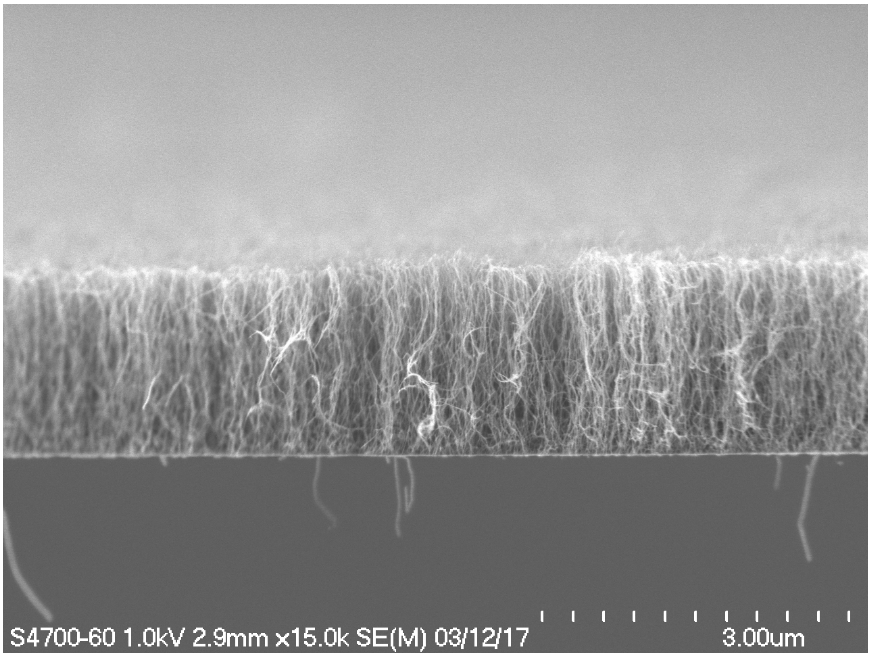

Figure 4.5: FE-SEM image showing vertically aligned SWNTs produced by the alcohol CVD method. The film thickness is approximately 2 μm.

produced SWNTs have an average diameter [37] of 1.9-2.0 nm and are several micrometers in length. An FE-SEM image of VA-SWNTs produced by the ACCVD method is shown in Fig. 4.5. The following chapters will explain the various studies undertaken to improve the synthesis of vertically aligned SWNT films, and to better understand their structure and properties.

Chapter 5

Elucidating the growth process

As discussed in the previous chapter, vertically aligned SWNT films were grown on quartz substrates from catalyst particles deposited by a liquid-based dip-coat process. Unless otherwise noted, the same dip-coat solution (0.01 wt% Co, 0.01 wt% Mo, dissolved in ethanol) was used in the following investigations.

5.1 Growth on silicon

Vertically aligned growth of single-walled carbon nanotubes had been achieved on quartz surfaces, but had not been successfully grown on a silicon wafer. Since the silicon wafer is coated with a native oxide layer that is chemically equivalent to quartz glass (SiO_2), growth on a Si wafer should be a reasonable extension of the quartz-based synthesis process. However, synthesis of vertically aligned SWNTs on Si wafers proved much more difficult. In most cases, vertically aligned growth was not achieved. The SWNT density was usually much lower than on quartz, resulting in sparse, tangled SWNTs (Fig. 5.1). In some cases, vertically aligned growth on a silicon wafer, such as that shown in Fig. 5.2a, was possible, but the yield was very low and the SWNT films were far from uniform, as indicated by the Raman spectra in Fig. 5.2b.

Despite being chemically equivalent (i.e. both being SiO_2), the surface of a silicon wafer is much smoother than that of polished quartz glass, having only minor variations on the order of an atomic layer or two. This difference in surface roughness may be critical in determining how much catalyst is deposited during the dip-coat process. Due to the smoothness of the Si wafer surface, it is possible that dip-coating does not result in a

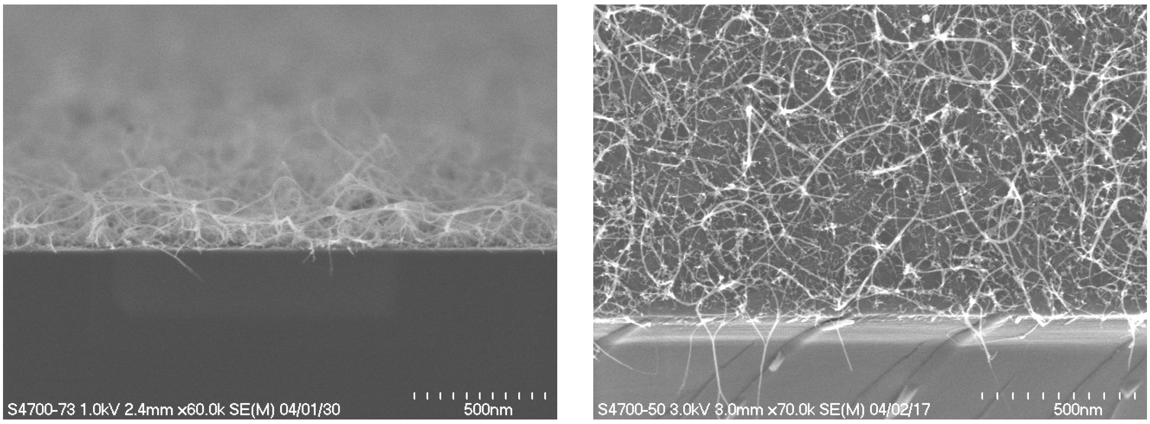

Figure 5.1: FE-SEM images of SWNTs synthesized on a silicon wafer. It is believed vertically aligned growth does not occur because of the low SWNT density.

sufficiently dense distribution of catalyst particles to result in vertically aligned growth. If so, using a higher concentration of solution or a more viscous solvent liquid (i.e. isopropyl alcohol, rather than ethanol) may increase the catalyst density on the substrate surface, resulting in vertically aligned growth. Another possible explanation for the low yield and lack of vertical alignment may depend on the thickness of the SiO_2 layer which exists natively on the surface of the silicon wafer. It has been reported [36, 38] that catalyst particles can lose their catalytic properties (known as catalyst poisoning) by reacting with pure Si at the high temperatures at which CVD growth of SWNTs occurs. If the native oxide layer on top of the Si surface is too thin there may be some interaction between the Si atoms in the wafer and the catalyst particles on the surface at the 800 °C growth temperature. This could cause some degree of catalyst poisoning by the formation of silicide, resulting in sparse, low-yield growth. Since the quartz glass is entirely SiO_2, silicide formation cannot occur, therefore the catalyst particles may be more active at the onset of SWNT growth.

Based on these results, it seems the next obvious step would be to investigate the two hypotheses presented here, in order to determine the cause of the poor yield of SWNTs grown on silicon wafers. However, if the conditions on which such a study were based were far from ideal, it is very likely that no clear conclusion could be reached. Therefore, we decided to go back to studying VA-SWNT growth on quartz and investigate the growth process in more detail in order to determine the optimal growth conditions for VA-SWNT synthesis.

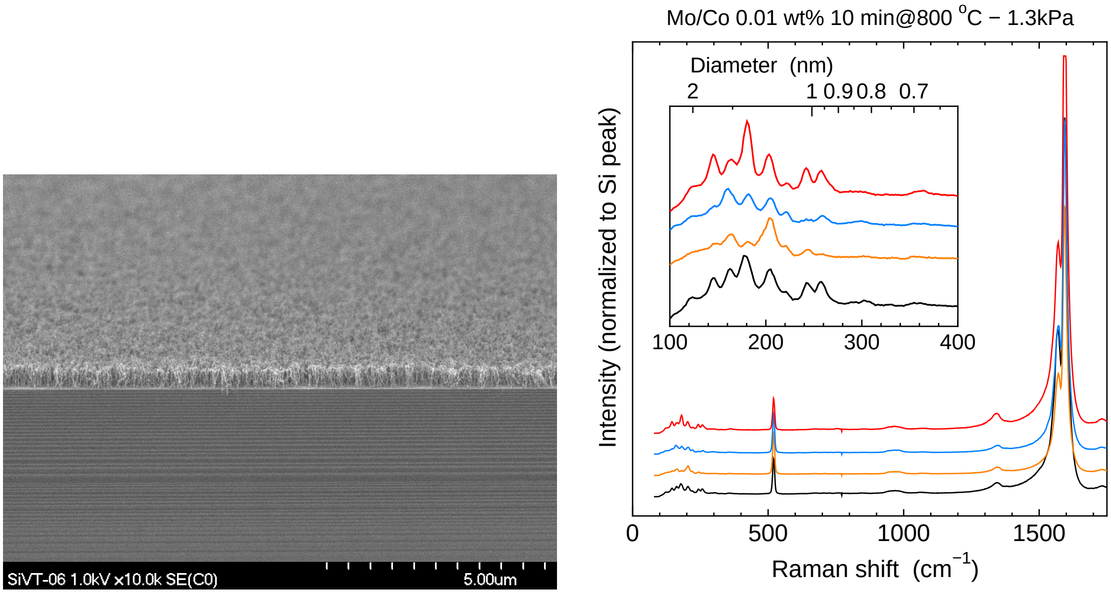

Figure 5.2: An FE-SEM image (left) and Raman spectra (right) of VA-SWNTs produced on a silicon wafer. The overall film morphology was not uniform, as is indicated by the very different RBM spectra obtained from the same sample.

5.2 The VA-SWNT growth mechanism

When studying the behavior of a transient process, it is very important to obtain "snapshots" of various stages of the process. Regarding growth of VA-SWNT films, this was achieved by stopping the CVD reaction after different CVD times, thereby allowing the growth to progress to different stages. By doing so, we expected to observe one of two likely trends, (i) a fast initial growth rate, which slows as the growth reaction continues, or (ii) a slow, linear growth rate that is relatively constant as long as the CVD conditions remain unchanged. The results were both as expected, yet somewhat surprising.

A time-series of SEM observations of VA-SWNTs grown for different CVD times is presented in Fig. 5.3. Up until 10 minutes, the film thickness increases with reaction time, with an apparent decrease in the growth rate with increasing CVD time. However, after 30 minutes of CVD there is an apparent *decrease* in the film thickness, which continues for longer CVD times (100 minutes). Since the environmental conditions were unchanged during CVD growth, two hypotheses can be presented to explain this decrease. The first is that, due to some variations in the dip-coating and catalyst preparation process, the initial

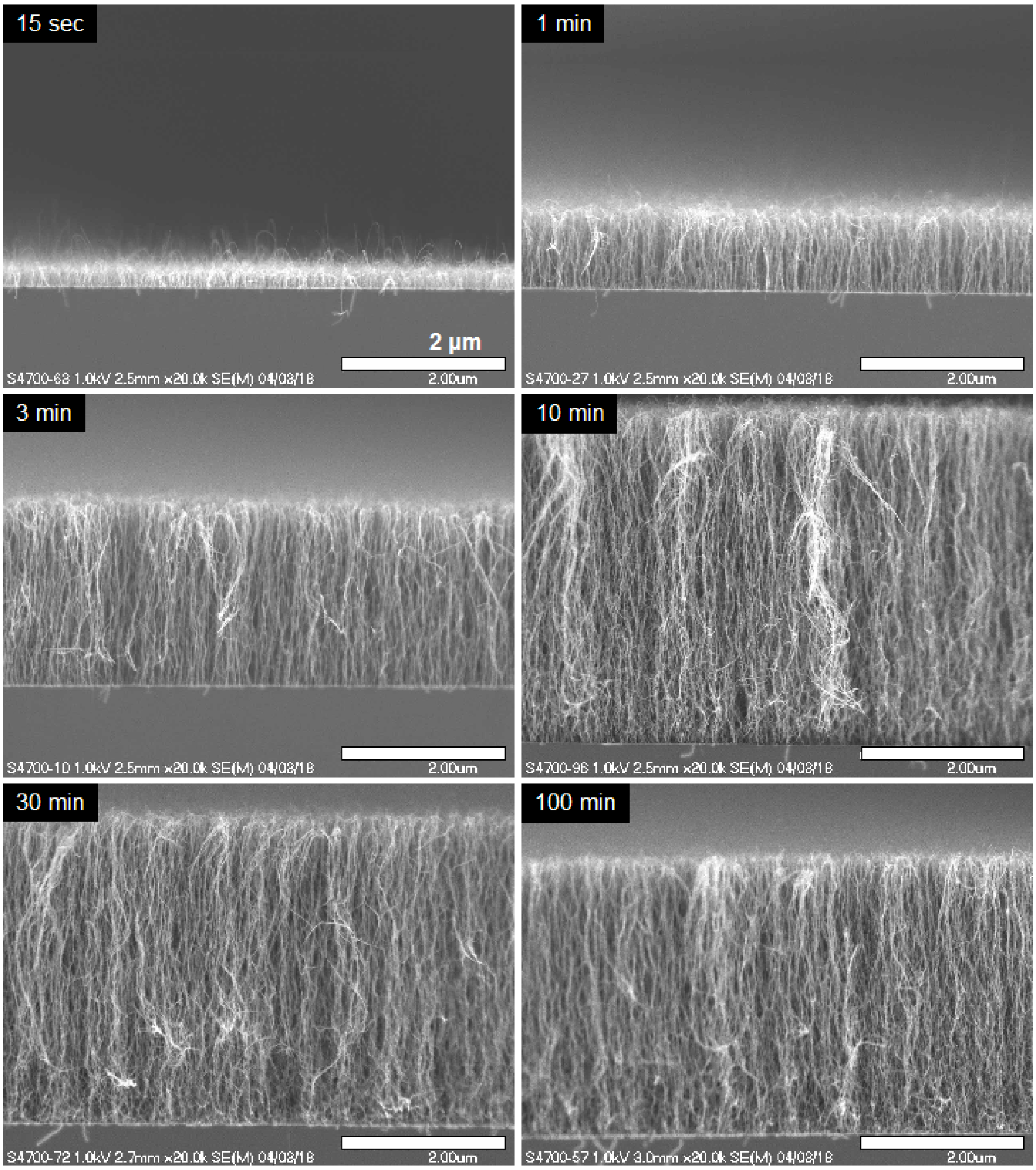

Figure 5.3: SEM images of VA-SWNT films produced after different CVD times [39]. The thickness increases as expected, but the growth rate seems to decrease with increasing CVD time. An apparent decrease in film thickness is seen after 30 min, and a larger decrease after 100 min of CVD. The scale is the same in all images.

state of the catalyst particles varies among samples. If the VA-SWNT growth proceeds in the same fashion for all cases, and the decrease in catalyst activity is the same (Fig. 5.4a), then the final thickness will be different (Fig. 5.4b). Thus, it is possible the initial catalyst

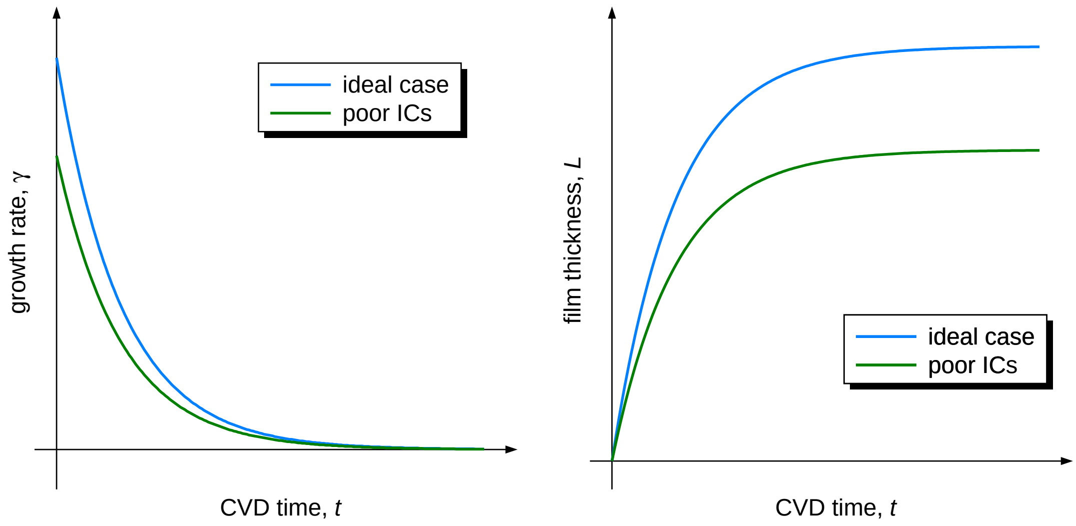

Figure 5.4: Hypothesis I: the initial growth rate and catalyst lifetime depend on the initial growth conditions, but growth proceeds in the same fashion, resulting in no decrease, just a lower final (maximum) film thickness

activity for the 10 min. case shown in Fig. 5.3 was slightly higher than for the 30 min. case, and both were initially more catalytically active than the 100 min. case. Those samples grown for less than 10 min. were probably unable to reach their maximum (final) height before the CVD reaction was stopped, thus it is unknown how long the growth could have progressed. The second hypothesis proposed to explain the apparent decrease is based on the harsh growth conditions. In the ACCVD method used to synthesize VA-SWNTs in these experiments, the growth temperature is maintained at 800 °C. This temperature is much higher than the burning temperature of SWNTs in air (between 500 and 600 °C for SWNTs prepared by the ACCVD method [32]), thus it is reasonable that minor burning of the SWNTs could occur if some air were present during growth (due to some slow leak in the vacuum chamber). If this were true, then two identical substrates, loaded with catalyst particles in the same initial state, would produce VA-SWNT films of different thicknesses depending on the length of CVD time (Fig. 5.5). If the rate of burning is slow, then this decrease will not be significant unless the high-temperature conditions are maintained after the film growth rate diminishes to zero. This could explain the small decrease observed at 30 min., and the further decrease observed after 100 minutes of CVD. This decrease is effectively a negative growth rate, which is seen in Fig. 5.5a.

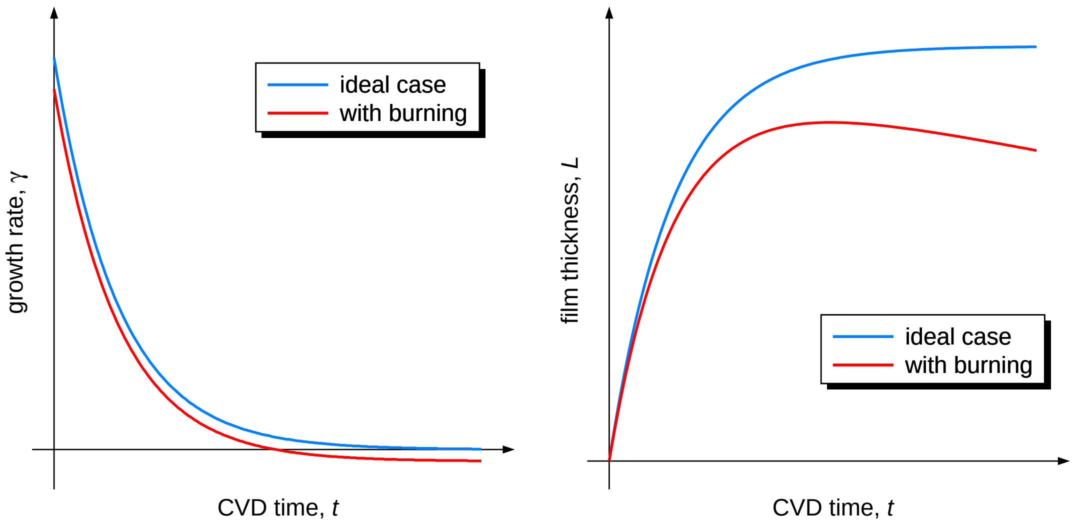

Figure 5.5: Hypothesis II: initial growth conditions are the same, but some environmental effect leads to burning of the SWNTs. This eventually leads to a decreasing film thickness.

5.2.1 Determination of VA-SWNT film thickness during CVD

Optical absorbance measurements of the VA-SWNT films shown in Fig. 5.3 are plotted in Fig. 5.6. According to the Beer-Lambert law, it is not surprising that the absorbance increases with increasing film thickness, as a thicker film simply means an increased optical path length. Plotting the absorbance at two common laser wavelengths (488 and 633 nm), we see in Fig. 5.7a that the absorbance and film thickness (determined from SEM) follow similar trends with increasing CVD time. The apparent decrease in VA-SWNT film thickness also appears in the absorbance data. This correlation between the absorbance and film thickness becomes clear in Fig. 5.7b, where the absorbance at 488 nm is plotted as a function of film thickness. The slope of this line is the absorption coefficient α, which has the value $\alpha = 6.78\ \mu\text{m}^{-1}$ for light with a wavelength of 488 nm.

Using this correlation between the thickness of a VA-SWNT film and its absorbance, we developed a technique by which the film growth can be indirectly measured during CVD by an *in situ* optical absorption measurement (Fig. 5.8). Very simply, the substrate is positioned such that a laser (λ = 488 nm) is incident normal to the substrate through a small opening in the bottom of the CVD furnace. The transmitted light passes through another small opening in the top of the furnace, and is then incident on a detector where the intensity is measured. The Beer-Lambert law was then used to calculate the absorbance.

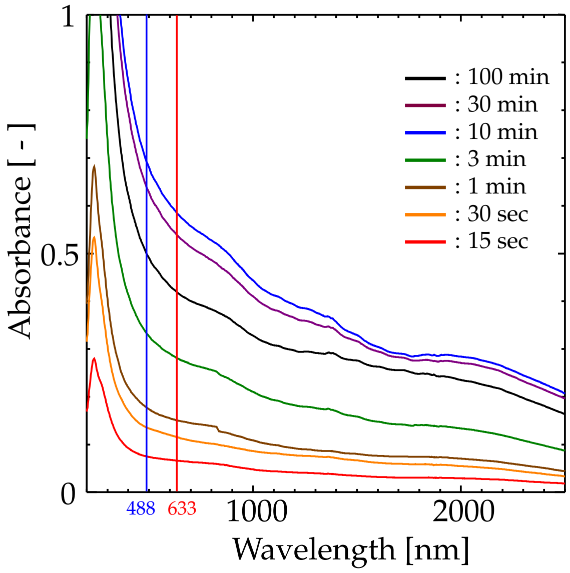

Figure 5.6: Absorption spectra of VA-SWNT films grown for different CVD times (same as in Fig. 5.3).

5.3 Analytical description of VA-SWNT growth

The *in situ* optical absorbance measurements of the VA-SWNT film growth described here have been reported in Refs. [39] and [40]. Some data obtained by this method are shown in Fig. 5.8. As hypothesized in the previous section, these data indicate an exponentially decreasing growth rate. However, the initial growth rate for the sample indicated by black squares is significantly higher than the other two cases. Even when the initial growth rate is similar (red circles and blue triangles), the growth rate decreases slightly faster for the blue-triangle case. These findings indicate there is some variation in both the initial catalyst condition and the catalytic reaction during SWNT growth.

5.3.1 Formulation of an analytical growth model

It is believed that the VA-SWNTs discussed in this report form by a root-growth mechanism [37, 41], where alcohol is dissociated by reacting with metal catalyst particles on the substrate surface. The amount of carbon contained in the feedstock gas supplied to the catalyst particles is the flux J [mol μm^{-2} s^{-1}] at the substrate surface. By some catalytic process, some number of moles of this available carbon are converted into SWNTs. This

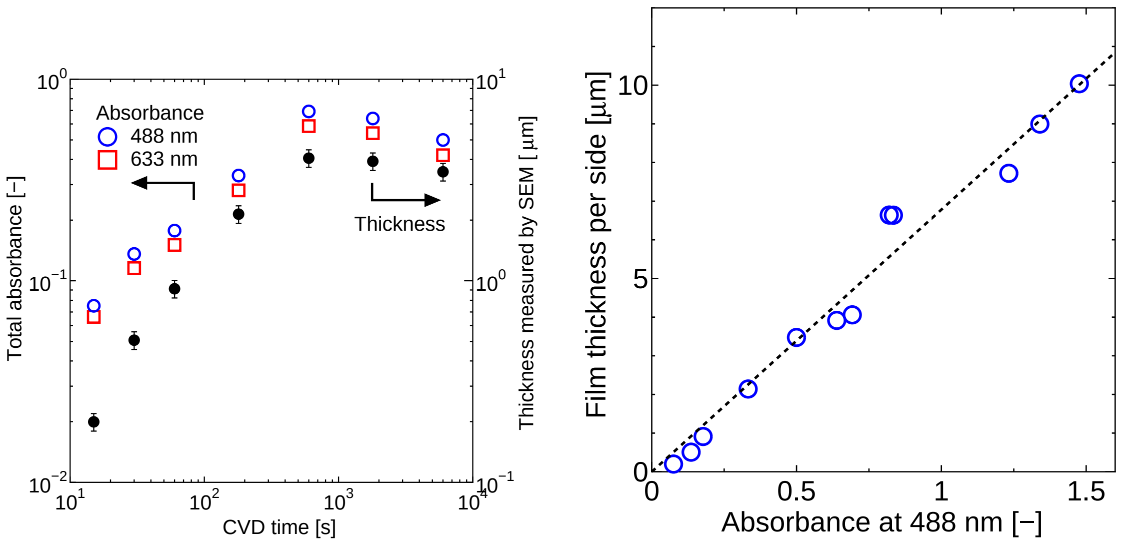

Figure 5.7: (left) The optical absorbance and VA-SWNT film thickness obtained from SEM for different CVD times. (right) The relationship between absorbance and VA-SWNT film thickness for 488 nm light [39].

conversion rate per substrate area is M [mol μm^{-2} s^{-1}], which can be thought of as the molar growth rate of SWNTs per substrate area. Also, M has the same units as J, thus M is essentially an outflux of carbon from the surface in the form of SWNTs. The ratio of available carbon (J) converted into SWNTs (M) is the catalyst *efficiency*, $\eta = M/J$. The growth rate γ [μm s^{-1}] can be expressed by dividing M by the density of the VA-SWNT film, ρ [mol μm^{-3}].

The optical absorption A can be defined as $A = \varepsilon\rho L$, where ε [μm^2 mol^{-1}] is the molar absorption cross section, ρ is the molar density, and L [μm] is the optical path length through the absorbing material (i.e. the VA-SWNT film thickness). In the *in situ* absorbance method described above, it is assumed that the concentration of the VA-SWNT film is uniform over the area of the laser spot, because the catalyst particles are uniformly distributed on the substrate surface [31, 35]. Since the absorbance is directly related to the VA-SWNT film thickness (see Fig. 5.7b), the growth rate $\gamma = \frac{dL}{dt}$ is proportional to $\frac{dA}{dt}$. This decrease in catalyst activity may be due to byproducts from alcohol decomposition reacting with the catalyst particles before diffusing away from the substrate surface, or due to the formation of amorphous carbon around the catalyst particles, preventing further influx of carbon from the alcohol. Since both of these processes are driven by the catalytic

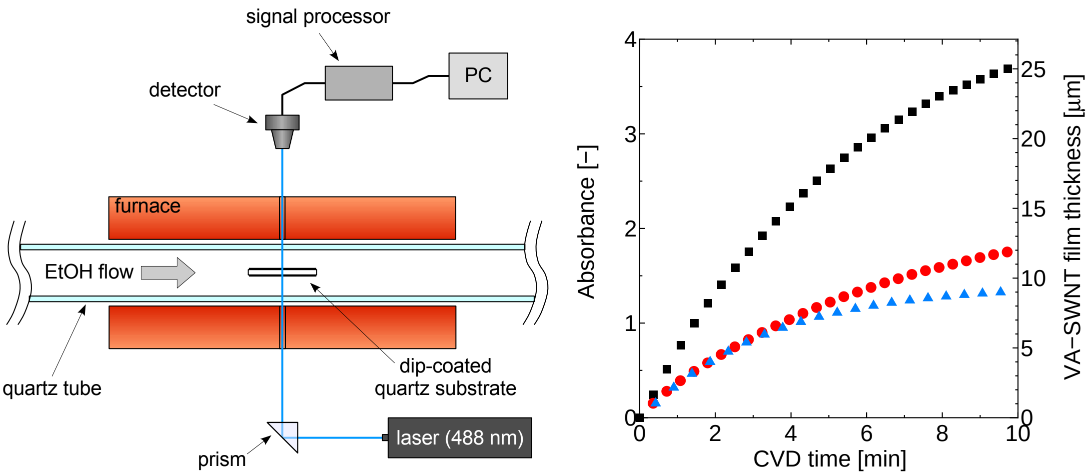

Figure 5.8: (left) Diagram of the *in situ* optical absorbance measurement. (right) Data obtained by the *in situ* measurement for different VA-SWNT films. The film thickness (right ordinate) was determined from the absorbance.

growth reaction it is postulated that the catalyst activity, and therefore the growth rate, diminishes in proportion to the SWNT growth rate by a proportionality constant κ [s^{-1}]. This is expressed by

$$\frac{\partial \gamma}{\partial t} = -\kappa \gamma. \tag{5.1}$$

Solving (5.1) yields the time-dependent expression for the growth rate,

$$\gamma(t) = \gamma_0 e^{-\frac{t}{\tau}}, \tag{5.2}$$

where γ_0 is the initial growth rate of the VA-SWNT film, and τ [s] (defined as $\tau \equiv \kappa^{-1}$) is the effective catalyst lifetime. From equation (5.2), the film thickness $L(t) = \int \gamma(t)dt$, and from the initial condition $L(t = 0) = 0$, the overall film thickness is described by the equation

$$L(t) = \gamma_0 \tau \left(1 - e^{-\frac{t}{\tau}}\right). \tag{5.3}$$

Due to the correlation between the VA-SWNT film thickness and the optical absorbance (Fig. 5.7b), the film thickness obtained from *in situ* optical absorbance measurements can be fit using equation (5.3). Data obtained by *in situ* absorbance measurements show the progression of VA-SWNT film growth with CVD reaction time. The growth rate (γ) is clearly fastest at the onset of growth, and decreases in an exponential fashion as the CVD reaction progresses (Fig. 5.9a). This behavior is independent of the film

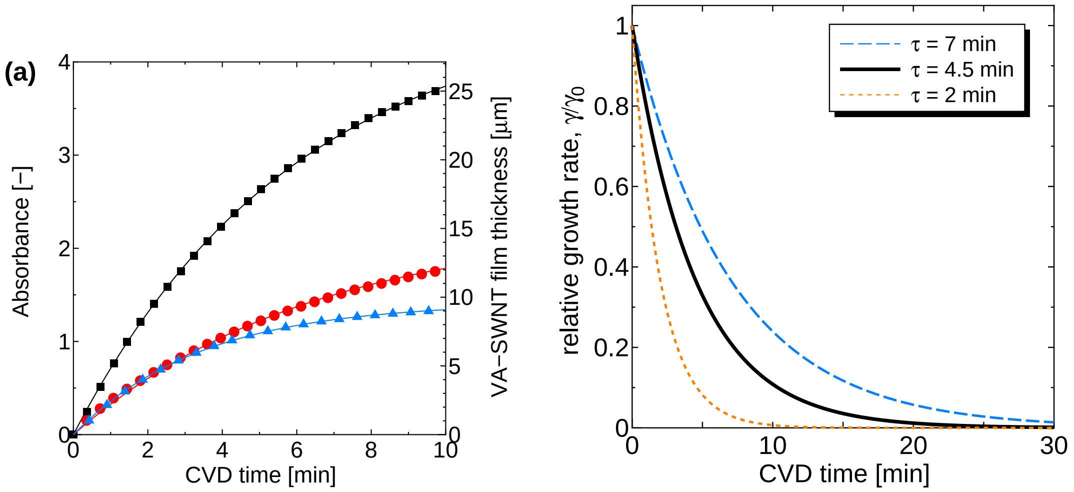

Figure 5.9: (a) *In situ* optical absorbance data showing the growth of different VA-SWNT films. The fitted curves were calculated for the data plotted in Fig. 5.8 using equation (5.3). (b) Exponential decay of the growth rate vs. CVD time. The thick line was calculated for the average value of τ determined from several fittings, and the dashed/dotted lines represent the upper/lower bounds.

thickness, indicating the slowing growth rate is due to diminishing catalyst activity rather than a diffusion-limited mechanism [40, 42]. Fitting for three different cases are shown in Fig. 5.9a, where the solid curves were fit to measured absorbance data (indicated by the markers). The initial growth rate γ_0 and catalyst lifetime τ were determined simultaneously by iterative fitting. Based on many fittings, the initial growth rate varied widely for different samples, but τ ranged from two to seven minutes, with an average value of 4.5 minutes. Using these values, the decay of the growth rate, or equivalently, the catalyst efficiency, is shown in Fig. 5.9b. The thick solid line was calculated from equation (5.2), and the dashed lines (calculated for $\tau = 2$ and 7 min) show the bounds. According to this plot, $\gamma(t)$ typically diminishes to less than 5% of γ_0 in approximately 15 min, indicating no appreciable growth will occur for longer CVD times. The excellent fit of the curves in Fig. 5.9a (R^2 values ≥ 0.995) show that the above model accurately describes VA-SWNT film growth. It is interesting to note that despite the different approach and very different experimental conditions, equation (5.3) has the same form as that reported by Futaba *et al.* [43] to describe the water-assisted growth from SWNTs from ethylene. The effective catalyst lifetime is also nearly the same (~4.5 min), which indicates the growth process is common to CVD synthesis in general. However, since the catalyst lifetimes were also found to be quite similar, the authors' conclusion that the addition of water prolongs the catalyst lifetime may be incorrect, or at least far less significant than its effect on the initial growth rate.

5.4 Burning and the growth environment

It was shown above that long CVD times ($t \gtrsim 30$ min) may lead to a decrease in VA-SWNT film thickness. It was hypothesized that this decrease was due to burning of the VA-SWNT film, caused by air leaking into the CVD chamber. In order to test this hypothesis, experiments were performed under different vacuum conditions, where the rate of pressure increase in the CVD chamber (the leak rate) was checked immediately prior to heating the CVD furnace for SWNT growth. After reaching the growth temperature of 800 °C, ethanol was introduced as in the standard ACCVD process. After the growth rate had diminished to essentially zero – determined by *in situ* monitoring of the absorbance – the ethanol flow was stopped and the CVD chamber maintained at 800 °C. The measured data are shown in Fig. 5.10a. The upper series in Fig. 5.10a (open circles) corresponds to a leak rate of $1.3\text{x}10^{-3}$ sccm. No decrease in film thickness was apparent after stopping the ethanol flow (indicated by the arrow in Fig. 5.10a). The lower series (represented by triangles) corresponds to a case where the leak rate was considerably faster ($4.2\text{x}10^{-3}$ sccm). After cutting off the ethanol supply (at t = 15 min, indicated by the arrow), a decrease in the absorbance, thus the film thickness, was clearly observed. This decrease is shown in detail in Fig. 5.10b. It is interesting to note that the time constant τ (determined from fitting) is similar in both cases, but the initial growth rate γ_0 is nearly one order of magnitude larger for the slow-leak case (open circles). This suggests a connection between the leak rate and the initial catalyst activity, possibly due to the extent of catalyst reduction during the heating stage immediately prior to SWNT growth, but this has not yet been clarified.

We found that a slow leak rate could be further slowed by flushing the system with Ar/H_2 for one hour or more, but faster leak rates (e.g. the case in Fig. 5.10b) were unaffected by flushing the system. This indicates that in the majority of cases, slow leak rates may be due to outgassing of the CVD chamber, rather than an actual leak in the vacuum system, and faster leak rates are actual leaks, which can lead to burning of the SWNTs. This burning can be accounted for in the growth model by introducing a burning term β

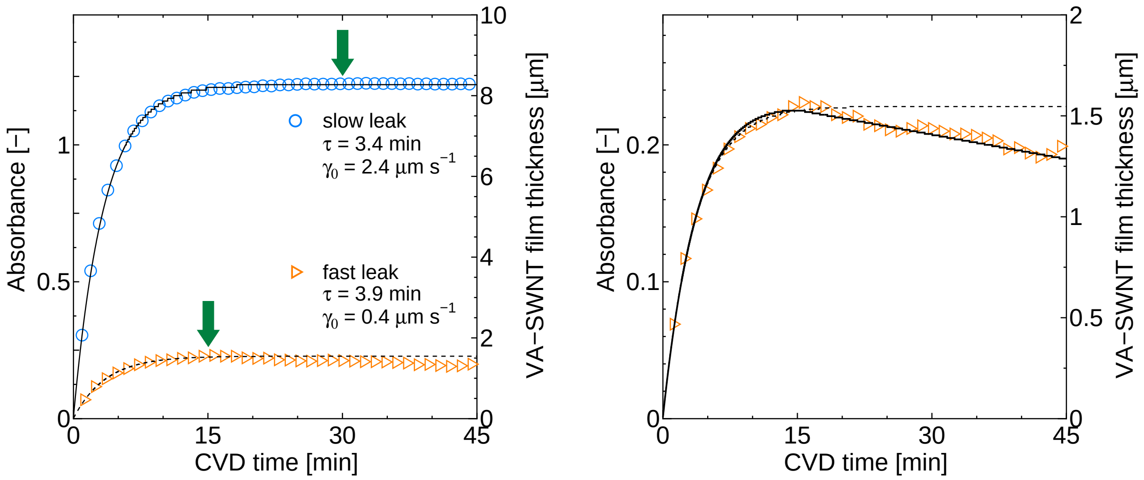

Figure 5.10: (a) Two cases where the leak rate of air into the CVD chamber was slow (upper series, circles) and fast (lower series, triangles). In both cases, the alcohol supply was cut-off after growth had effectively stopped (indicated by the arrows) and the CVD chamber was maintained at the growth temperature of 800°C. A decrease in the film thickness detected for the fast leak case (triangles) is shown in detail in (b), where the dashed curve was fitted using equation (5.3), and the solid curve (which accounts for burning) was fitted using equation (5.4).

[μm s^{-1}], which effectively opposes the film growth rate $\gamma(t)$. Based on the trend shown in Fig. 5.10b, and since the environmental conditions inside the CVD chamber are unchanged during SWNT growth, we make the assumption that burning occurs at a constant rate. By subtracting β from the growth term in equation (5.2), the resulting expression for the film thickness including burning effects is

$$L(t) = \gamma_0 \tau \left(1 - e^{-\frac{t}{\tau}}\right) - \beta t. \tag{5.4}$$

Since burning cannot occur when no SWNTs are present, the conditions imposed on β are

$$\beta \begin{cases} = 0 & \text{when} L(t) = 0 \\ \geq 0 & \text{when} L(t) > 0. \end{cases} \tag{5.5}$$

The data in Fig. 5.10a were fit using equation (5.3), in which burning effects are ignored (β = 0), and using equation (5.4), which accounts for burning ($\beta > 0$). For the slower leak rate (open circles), both fitting methods yielded the same result, with $\beta \approxeq 0$ in equation (5.4), showing that burning is negligible. Fittings for the faster leak case are shown in detail in

Fig. 5.10b. The fitting which ignores burning (dotted line) is clearly incorrect, however when burning effects are included (solid line), the data are fit quite accurately. The value of β obtained from this fitting is approximately 2% of γ_0 ($\beta \approx 0.008$ μm min^{-1}). This value is quite small, meaning burning effects are negligible for short CVD times, but can become significant for longer CVD times.

The form of equation (5.4) shows the VA-SWNT film thickness increases as long as the growth rate exceeds the rate of burning, but as the catalyst efficiency diminishes, the growth rate will slow to a point where burning eventually dominates (if $\beta \neq 0$) and the net growth rate will become negative. This transition occurs when $\gamma(t) = 0$, or

$$\beta = \gamma_0 \left(1 - e^{-\frac{t}{\tau}}\right). \tag{5.6}$$

This condition is satisfied at some time t_c, where

$$t_\mathrm{c} = -\tau ln \left(\frac{\beta}{\gamma_0}\right). \tag{5.7}$$

Various fittings using equation (5.4) yielded values of t_c between 50 and 100 min, with an average of 70 minutes (Fig. 5.11). Since this is considerably longer than the CVD growth time, which need not exceed 15 or 20 minutes (determined from Fig. 5.9b), burning is insignificant in most cases. However, when the leak rate is appreciable, t_c becomes comparable to the growth time, and burning of the VA-SWNT film can become significant. For the two cases shown in Fig. 5.10a, the values of t_c for the upper and lower cases are 102 and 15 min, respectively. In the upper case (circles), $t_\mathrm{c} \gg t$, meaning burning of the film is negligible, thus the data are fit accurately when $\beta = 0$ in equation (5.4). However, for the lower case (fast leak rate), t_c is on the order of t, thus burning is significant, as shown in Fig. 5.10b. It should be noted that accurate determination of t_c is difficult because in most cases $\beta \ll \gamma_0$, thus $t_\mathrm{c} \rightarrow \infty$ as $\beta \rightarrow 0$.

Due to the exponential decay of the catalyst efficiency and possible burning effects, the effective CVD time and the maximum growth time before burning becomes dominant (t_c) were determined. Knowledge of these two values could be important for maximizing SWNT production, indicating the *in situ* method could be used not only for controlling growth of VA-SWNT thin films, but also for assessing the conditions inside a CVD system. Further studies on the role of the CVD environment on SWNT growth, such as the effect of pressure and temperature on the initial catalyst activity and catalyst lifetime, would be beneficial in optimizing the production of morphology-controlled SWNTs.

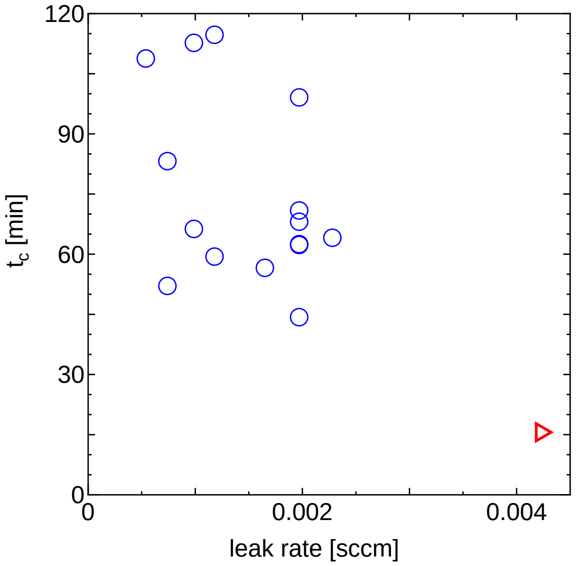

Figure 5.11: The red triangle corresponds to the fast leak case in Fig. 5.10a, for which burning was observed, and t_c is on the order of the CVD reaction time.

5.4.1 Optical measurement of burning temperature

The *in situ* optical absorbance technique presented in this chapter allows accurate, nondestructive determination of the film thickness during CVD growth. As shown above, this method was used to elucidate the growth process, as well as confirm burning of the VA-SWNT film. When synthesizing SWNTs, one of course wants to suppress burning to maximize the yield. However, as shown here, the ability to precisely measure this burning can be used to determine the burning temperature of SWNTs when only a small amount of material is available.

The standard way to determine the burning temperature of a material is by thermogravimetric analysis (TGA), where one measures the change in mass of a material as it is heated in a well-controlled manner. The problem with applying TGA to SWNTs is that it is often difficult to obtain enough mass for an accurate measurement. Using the *in situ* method described in the previous section it is possible to measure the burning of the film by measuring the change in absorption. Such an experiment was performed on a VA-SWNT film, and the result is quite similar to previous TGA measurements (see Fig. 5.12). The experiment was performed under dry air at 1 atm, with a heating rate of 2 °C per minute. The burning temperature appears to be slightly higher than for VA-SWNTs

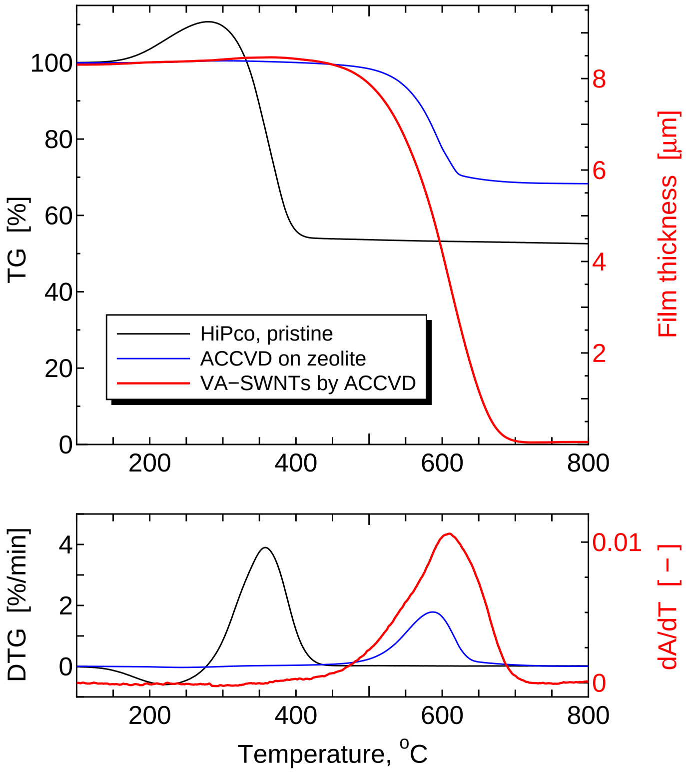

Figure 5.12: Thermal decomposition of VA-SWNTs measured by *in situ* optical absorption (red) vs. TGA measurements of SWNTs produced by the ACCVD and HiPco methods. In the lower graph, the burning temperature is determined by the peak in the differential spectrum.

measured by TGA (blue line in Fig. 5.12). This may be because the average diameter of VA-SWNTs is slightly larger than that of SWNTs synthesized from alcohol on zeolite, making them energetically more stable [40]. One drawback to the optical method, however, is the final absorbance (thickness) value reads zero after all SWNTs are burned. In the TGA method, one can estimate the purity of the SWNTs by comparing the level of the baseline (the fraction of metal particles, etc. contained in the original sample) to the initial weight. This optical method will not likely challenge TGA as the standard technique, but can offer an advantage when dealing with small amounts of material, as with the VA-SWNT films discussed here.

Chapter 6

Optical and X-ray spectroscopy

In the previous chapter I showed how the optical absorbance of a VA-SWNT film can be used to determine the film thickness, thus obtain information on the growth process of the film. There are, in fact, many optical methods that can be used to obtain various kinds of information, some of which will be presented in this chapter. In particular, I will focus on optical measurements using polarized light, which, due to the anisotropic absorption of SWNTs [25, 44], one can obtain information on the internal structure of the aligned SWNT film. An example of one practical application which takes advantage of this nonlinear absorbance is also presented. Lastly, I will present results from X-ray absorption spectroscopy using synchrotron radiation as the light source.

6.1 Polarization dependent optical absorbance

As discussed in Chapter 2, the wavevector $\vec{k}$ of an optical photon is very small, thus absorption of photons in the optical range induces vertical transitions, in which $\Delta k = 0$. The probability of such a transition occurring depends on the orientation of the electric field vector $\vec{E}$ of an incoming photon with respect to the appropriate absorption dipoles in a SWNT. For low energies, corresponding to light in the UV-vis-NIR range, the strongest absorbing dipoles are oriented along the SWNT axis [45, 46], denoted by the unit vector $\hat{\ell}$. Absorption by perpendicularly oriented dipoles is much weaker, and is the cause of the highly anisotropic absorption by SWNTs. Therefore, angle-resolved absorption spectroscopy using polarized light can be used to determine the orientation of aligned SWNTs. This experiment was performed using an absorption spectrometer, where the incident light

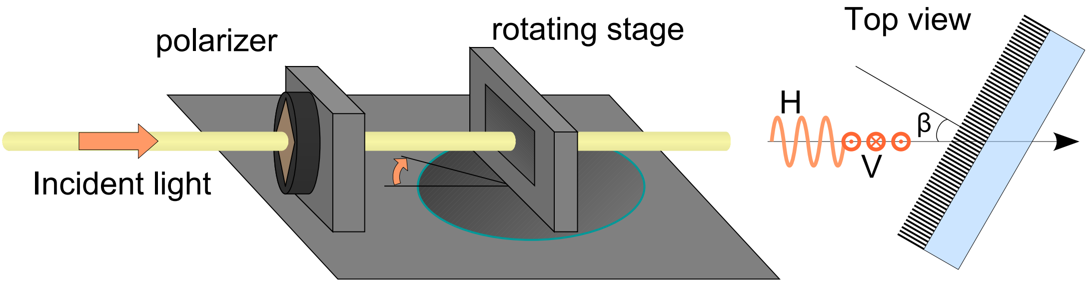

Figure 6.1: Experimental setup for polarization-dependent optical absorption measurements. A top view shows the perspective along the rotation axis.

was polarized either vertically or horizontally (with respect to the lab), and the angle of incidence on the VA-SWNT film was changed by rotating the substrate holder. The setup is shown in Fig. 6.1. For two polarization orientations, V and H, the SWNT film was rotated through an angle β with respect to the propagation direction of the incident light. The results of each case will be discussed separately, in order to minimize confusion from going back and forth between the two. I will begin with the V case.

6.1.1 Polarization along rotation axis

For optical absorption in the range of this experiment, it is known that SWNTs exhibit strong absorption for light polarized along the SWNT axis, $\hat{\ell}$, and very weak absorption when perpendicularly polarized with respect to $\hat{\ell}$. Let us assume the vertically aligned SWNTs are straight, such that $\hat{\ell}$ lies along the substrate normal, denoted by $\hat{z}$. Since the polarization with respect to $\hat{\ell}$ determines the absorption, we describe the polarization of the incident light relative to the substrate normal $\hat{z}$, rather than relative to the substrate surface. For the orientation marked "V", the spectra measured for values of $\beta = 0°$, 15°, 30°, and 45° are plotted in Fig. 6.2a. The absorption spectra are essentially the same for all angles. The reason for this is as follows. Initially (for $\beta = 0$), $\vec{E} \perp \hat{z}$, and $\vec{E}$ is parallel to the axis of rotation. Therefore, the orientation of $\vec{E}$ with respect to the SWNTs (which are oriented along $\hat{z}$) does not change with $beta$, so there should be no β-dependence on the absorption. In other words, changing β does not change the relative orientation between $\vec{E}$ and the absorption dipoles in the aligned SWNTs, thus does not affect the absorption.

In the second case ("H" in Fig. 6.2), the polarization of the incident light has been rotated by 90°, so $\vec{E}$ is now in the plane of sample rotation. Therefore, the absorption

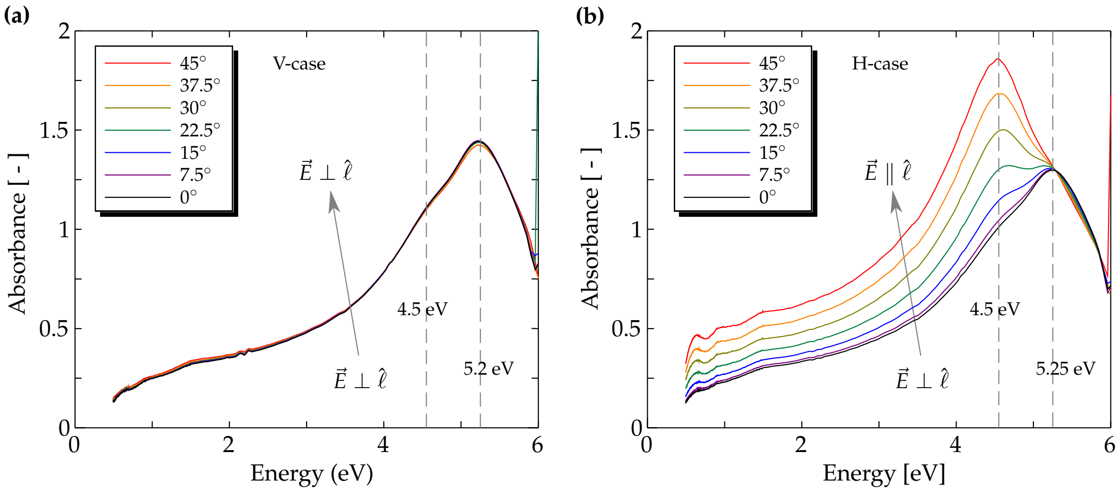

Figure 6.2: Angle-dependent polarized absorption spectra for the two cases "V" (a) and "H" (b), as shown in Fig. 6.1 (from [44]).

dipoles are coplanar, and should strongly depend on β. The angle-resolved spectra are shown in Fig. 6.2b. For this orientation, the incident light is initially polarized perpendicular to the substrate normal $\hat{z}$ (at $\beta = 0$), thus the absorption is the same as in the "V" case (Fig. 6.2a). However, as the sample is rotated the SWNT axes became more in line with $\vec{E}$. Therefore, the absorbance, which depends on the inner product $\vec{E} \cdot \hat{\ell}$, increases (remember we are assuming the SWNT axis $\hat{\ell}$ is collinear with the substrate normal $\hat{z}$).

6.1.2 Determining the degree of alignment

In Fig. 6.2a, the spectrum for $\vec{E} \perp \hat{\ell}$ has a broad peak at 5.25 eV, but is otherwise featureless. Absorption peaks due to interband transitions, which should be found below ~ 2 eV, are suppressed because the absorption for this polarization is much weaker than for parallel polarization [46]. The peak at 5.25 eV is attributed to a plasmon resonance of the π electrons, which is common for carbon systems [47, 48, 49, 50, 51]. As β is changed and $\vec{E}$ becomes increasingly polarized along the SWNT axis (for the "H" case in Fig. 6.2b), we see two major changes in the absorption spectra. First of all, the low-energy peaks ($E < 2$ eV) corresponding to interband excitations increase, as expected. Also, the position of the π plasmon peak changes from 5.25 to 4.5 eV. This change is puzzling because the π plasmon peak energy does not disperse from 5.25 to 4.5 eV, but rather the dominant peak

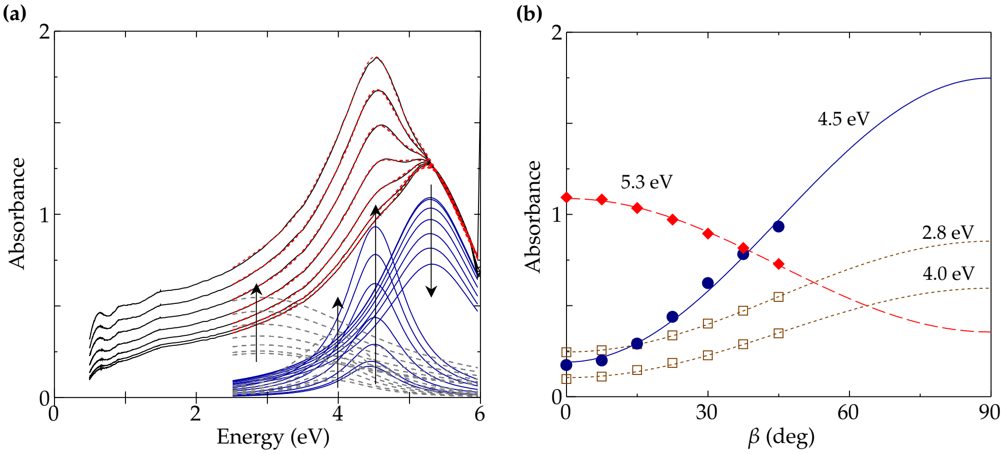

Figure 6.3: (a) Lorentzian fitting of the spectra shown in Fig. 6.2 (“H” case) for angles $0 \leq \beta \leq 45°$. The arrows show the change with increasing β. (b) Dependence of each Lorentzian amplitude on the incidence angle β (from [44]).

changes to a second peak with energy of 4.5 eV. In the following analysis I will show how this angular dependence can be used to estimate the degree of alignment of the SWNTs in the aligned film.

Figure 6.3a shows the fitting of the spectra in Fig. 6.2b by four Lorentzian curves. The arrows indicate the direction of the change as β increases from 0° to 45°. The β-dependence is plotted in Fig. 6.3b. This analysis shows the presence of distinct peaks at 4.5 and 5.25 eV. Since the dependence on β is essentially the same for both peaks, either can be used as the basis for determining the orientation dependence. However, since the peak at 5.25 eV is located near the edge of the measured range, the baseline cannot be determined accurately, thus we choose the 4.5 eV peak for our analysis. In order to analyze these results we need to formulate a model that describes the interaction between the incident light and the SWNT absorption dipoles, which provides an expression for the optical absorbance anisotropy. It is noted that the following analysis takes a somewhat different but equivalent approach than used in the original publication of these findings (Ref. [37]).

6.1.2.1 Interaction geometry

Consider a right-handed Cartesian coordinate system described by the axes x, y, and z, defined by the orthonormal unit vectors $\hat{x}$, $\hat{y}$, and $\hat{z}$, respectively. Let the xy-plane

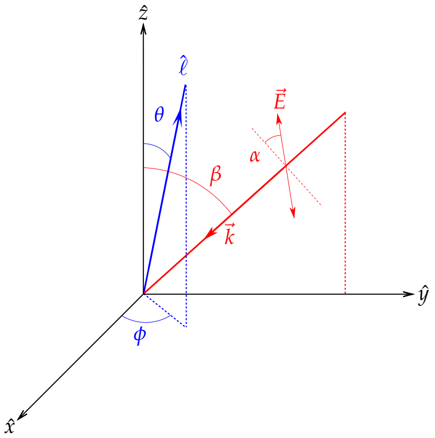

Figure 6.4: the orientation of an SWNT and an incoming electromagnetic wave along the propagation vector $\vec{k}$

be parallel to the plane of the substrate, such that the substrate normal is oriented in the direction of $\hat{z}$. Now let the orientation of the axis of a SWNT with respect to the origin of the coordinate system be described by the directional vector $\hat{\ell}$. In describing $\hat{\ell}$, it is convenient to use spherical polar coordinates, which are related to the Cartesian components by

$$\begin{aligned} x &= \sin\theta\cos\phi \\ y &= \sin\theta\sin\phi \\ z &= \cos\theta \end{aligned}$$

The angle θ is measured from the positive z-axis, and ϕ is measured from the positive x-axis. Due to the symmetry of this system, we can make the following restrictions

$$0 \leq \theta \leq \frac{\pi}{2}$$
$$0 \leq \phi \leq \pi$$

Therefore, the SWNT axis can be represented by the vector

$$\hat{\ell} = \begin{bmatrix} \sin\theta\cos\phi \\ \sin\theta\sin\phi \\ \cos\theta \end{bmatrix} \tag{6.1}$$

as shown in Fig. 6.4.

Now that we have a description of the orientation of a SWNT, let us consider an incident electromagnetic wave, propagating along the wavevector $\vec{k}$, where $\vec{k}$ is confined to the yz-plane. If $\vec{k}$ makes an angle β with the positive z-axis, then the orientation of $\vec{k}$ is described by

$$\hat{k} = \begin{bmatrix} 0 \\ -\sin\beta \\ -\cos\beta \end{bmatrix} \tag{6.2}$$

The polarization of the incident light is defined by the orientation of the electric field $\vec{E}$, which, according to Maxwell's equations, is perpendicular to the propagation direction $\vec{k}$. We can therefore describe the orientation of $\vec{E}$ by the angle α ($0 \leq \alpha \leq \pi$), where α is measured from the yz-plane (i.e. the plane in which $\vec{k}$ propagates). Thus, the expression for the orientation of the electric field, which describes the polarization, is

$$\vec{E} = E \begin{bmatrix} \cos\alpha \\ \cos\beta\sin\alpha \\ \sin\beta\sin\alpha \end{bmatrix} \tag{6.3}$$

In this description, the incident electromagnetic wave is p-polarized with respect to the substrate when $\alpha = 0$ ("H" case), and is s-polarized when $\alpha = \frac{\pi}{2}$ ("V" case). The orientation of the SWNTs in the sample can be estimated by calculating the anisotropy, r, which is defined as

$$r = \frac{\Lambda_{\parallel} - \Lambda_{\perp}}{\Lambda_{\parallel} + 2\Lambda_{\perp}}, \tag{6.4}$$

where $\Lambda_{\parallel}$ and $\Lambda_{\perp}$ are the total absorption by parallel and perpendicular absorption dipoles, respectively [52]. The absorption of an incident photon by a SWNT depends on the orientation of the absorption dipole $\vec{\mu}$ with respect to the electric field $\vec{E}$ of the incident photon. The probability of absorption is given by $|\vec{E} \cdot \vec{\mu}|^2$. For interband transitions, the absorption dipole $\vec{\mu}$ is oriented along the SWNT axis, i.e. collinear with $\hat{\ell}$. Thus, absorption is strongest for light polarized along the SWNT axis (parallel to $\hat{\ell}$), but from equation (6.4) we see that we must also take into account absorption by perpendicular dipoles in order to correctly describe the overall interaction. For clarity, the expressions for parallel and perpendicular absorption dipoles will be treated separately in the following discussion.

We begin by defining the parallel absorption dipole, $\vec{\mu}_{\parallel} = \mu\hat{\ell}$. The absorption by $\vec{\mu}_{\parallel}$ is given by the equation

$$\begin{aligned}\Lambda_{\parallel} &= \left|\vec{\mu}_{\parallel} \cdot \vec{E}\right|^2 \\ &= \mu_{\parallel}^2 E^2 \left[\sin\theta\cos\phi\cos\alpha + \sin\theta\sin\phi\cos\beta\sin\alpha + \cos\theta\sin\beta\sin\alpha\right]^2 \\ &= \mu_{\parallel}^2 E^2 \left[\cos\alpha(\sin\theta\cos\phi) + \sin\alpha(\cos\beta\sin\theta\sin\phi + \sin\beta\cos\theta)\right]^2 .\end{aligned} \tag{6.5}$$

For the α = 0 ("H") case, the above expression becomes

$$\Lambda_{\parallel}(\alpha = 0) = \frac{1}{2}\mu_{\parallel}^2 E^2 \langle \sin^2\theta \rangle \tag{6.6}$$

and for the $\alpha = \frac{\pi}{2}$ ("V") case, we obtain

$$\Lambda_{\parallel}\left(\alpha = \frac{\pi}{2}\right) = \frac{1}{2}\mu_{\parallel}^2 E^2 \Big[\cos^2\beta\langle\sin^2\theta\rangle + 2\sin^2\beta\langle\cos^2\theta\rangle\Big]. \tag{6.7}$$

We now address the case of perpendicular dipoles. The relevant dipole vector, $\vec{\mu}_{\perp}$ is perpendicular to the SWNT axis, but its magnitude is unchanged for all circumferential angles. Hence, if a photon is incident along the SWNT axis (i.e. if $\hat{k} \parallel \hat{\ell}$), absorption by perpendicular dipoles will be independent of the polarization direction. Therefore, we use the definition $\vec{\mu}_{\perp} = \mu\hat{k}$, and define the absorption as $\Lambda_{\perp} = E^2|\vec{\mu}_{\perp} \cdot \hat{\ell}|^2$. This approach yields

$$\begin{aligned}\Lambda_{\perp} &= \mu_{\perp}^2 E^2 \left[\sin^2\beta\langle\sin^2\theta\rangle\langle\sin^2\phi\rangle + \cos^2\beta\langle\cos^2\theta\rangle\right] \\ &= \frac{1}{4}\mu_{\perp}^2 E^2 \left[\cos^2\beta\langle\cos^2\theta\rangle + \frac{1}{2}\sin^2\beta\langle\sin^2\beta\rangle\right]\end{aligned} \tag{6.8}$$

These expression are the components of the anisotropy defined in equation (6.4).

At this point we take into account the fact that the SWNTs are not perfectly aligned, but distributed around the z-axis. This distribution is described by some function $f(\theta)$, where θ is the angle between the SWNT axis and the substrate normal (see Fig. 6.4). This distribution is described by a number called the *nematic order parameter*, S, which is defined as [37, 53]

$$S = \int_{-1}^{1} f(\theta)\left(\frac{3\cos^2\theta - 1}{2}\right) d(\cos\theta) = \frac{3\langle\cos^2\theta\rangle - 1}{2}. \tag{6.9}$$

This parameter can be included in equation (6.4) to describe the imperfect distribution

$$r = \frac{\Lambda_{\parallel} - \Lambda_{\perp}}{\Lambda_{\parallel} + 2\Lambda_{\perp}} S \tag{6.10}$$

Fitting the polarization-dependent absorption data by this method [37], one obtains the value $S \approx 0.75$, corresponding to an average deviation from the substrate normal of $\langle\theta\rangle \approx 24°$ [44]. An example of applying the nonlinear absorption properties of VA-SWNTs to an optical application is presented in the following section.

6.2 Nonlinear optics application

Over the past few decades, passively mode-locked lasers have been receiving much attention due to their advantages over active mode-locking schemes because they can realize ultrashort pulse formation from a simple and robust laser structure [54]. The discovery of the high nonlinearity and saturable absorption properties of SWNTs has further accelerated research in recent years. Other notable attractions include wide operating bandwidth (ranging from 1 to 2 μm), ultra-short recovery time ($\sim$500 fs), high optical damage threshold, and excellent compatibility with fibers and nano-devices due to their extremely small footprint [55]. The state of polarization in a SWNT mode-locked laser is managed by controlling the morphology of the SWNTs.

6.2.1 Passive mode-locking by VA-SWNTs

Past studies on nanotube-based devices have focused on the diversification of the mode-locked lasers in terms of operating wavelength, repetition rate, novel mode-locking scheme, and matrix material for nanotube dispersion. Recently, a novel all-fiber mode-locking scheme was demonstrated in which the evanescent field of the light propagating in the fiber interacts with the SWNTs to induce loss modulation in the laser cavity [56]. In previous studies, alcohol-grown SWNTs [26] were sprayed onto either a D-shaped fiber or tapered fiber, so the SWNTs can interact with the propagating mode inside the optical fiber. However, the preparation of such fibers and application of SWNTs is difficult. Furthermore, randomized SWNTs have a reduced interaction because only the SWNTs that are aligned with the electric field of the propagating light ensure the saturable absorption effect.

We have developed a new scheme for nanotube-based mode-locking incorporating VA-SWNT films [57]. A VA-SWNT film is attached onto a D-shaped fiber (Fig. 6.5) to maximize the interaction between the evanescent field of the propagating light and the

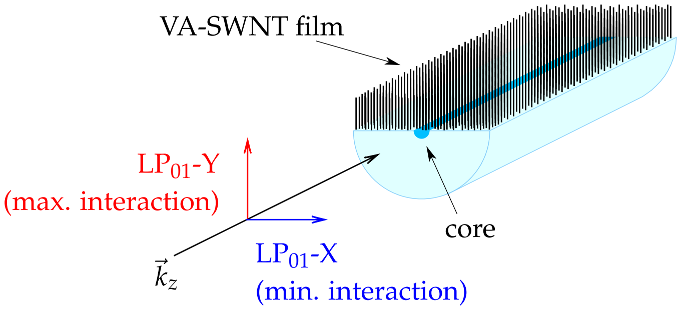

Figure 6.5: A VA-SWNT film transferred onto a D-shaped optical fiber. Alignment of the SWNTs maximizes interaction with the LP_{01}-Y mode propagating through the laser cavity.

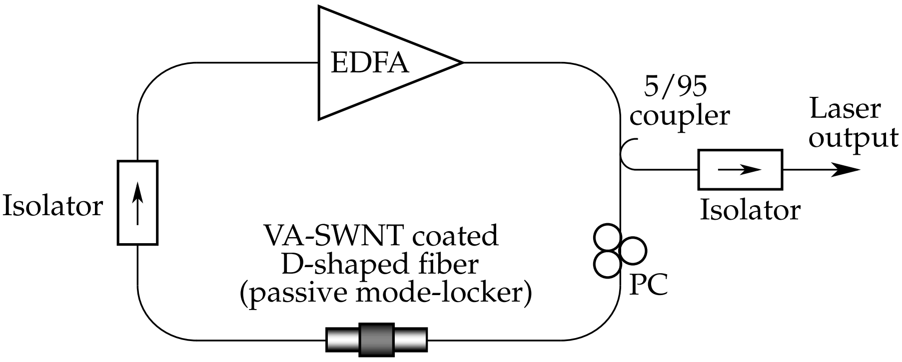

Figure 6.6: The ring cavity setup used to demonstrate the passive mode-locking by the VA-SWNT-coated fiber.

aligned SWNTs over a reasonably long distance. The SWNT-fiber is then inserted into the all-fiber ring cavity, as shown in Fig. 6.6.

The ring laser demonstrated here uses an Erbium-doped fiber amplifier (EDFA) as a gain medium (16-dBm average power). In order to minimize the deleterious reflection to the SWNT mode-locker, isolators are inserted both after the mode-locker and at the output port. A polarization controller (PC) optimizes the round-trip polarization in the laser cavity; 5% of the intracavity lasing light is tapped for the laser output, while the other 95% of the power is fed back into the ring cavity. Using this all-fiber configuration, we successfully demonstrated the operation of a passive mode-locked laser using a VA-SWNT-based saturable absorber. The output spectrum of the laser is shown in Fig. 6.7. The output pulse train (left), showing a repetition rate of 5.7 MHz, verifies pulse formation

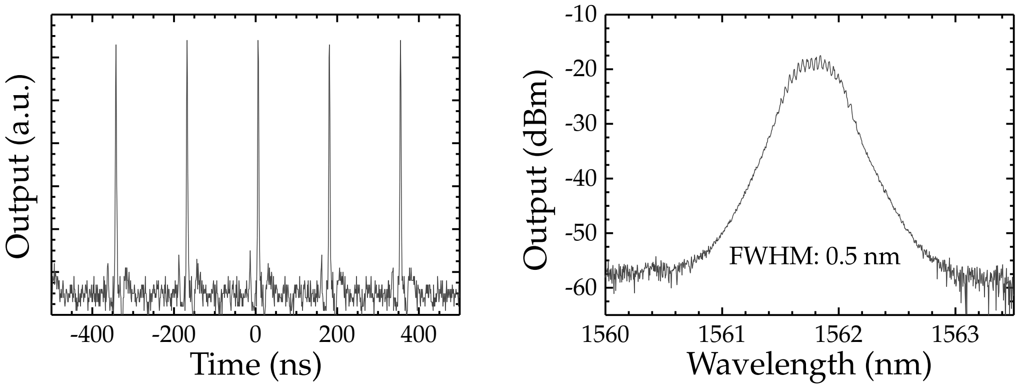

Figure 6.7: Laser output showing the pulse train at 5.7 MHz (left) and the output spectrum (right), with a 3dB FWHM of 0.5 nm.

by our VA-SWNT mode-locker. The center wavelength (right) is 1561.8 nm with a 3 dB spectral FWHM of 0.5 nm, indicating a temporal pulse of 5.12 ps.

This new scheme highlights some remarkable advantages including (i) simple and safe SWNT application process, (ii) maximized SWNT interaction with the evanescent field of propagating light due to the SWNT alignment, (iii) high success rate (near 100%) for device manufacturing, and (iv) low SWNT density threshold to achieve mode-locking. We expect that further optimization of the laser cavity, including the mode-locker design, will result in a significant improvement of the output pulse quality.

6.3 Studies using synchrotron radiation

High-energy optical studies on VA-SWNTs were performed using synchrotron radiation, the electromagnetic waves emitted by charged particles (typically electrons) circulating at high speeds in particle accelerators. In the early years of particle accelerators, this phenomena was viewed by high-energy physicists as an inescapable problem because it resulted in a significant loss of the energy necessary for particle physics experiments. However, once it was realized that this radiation could be used as a source of super-intense, tunable, highly-polarized light covering a very broad spectrum, its usefulness for investigating many aspects of a wide range of materials quickly became evident. At each of these facilities, called light sources (Fig. 6.8), there is a large "storage ring", around which packets of electrons (steered by magnetic fields) race at nearly the speed of light. This storage

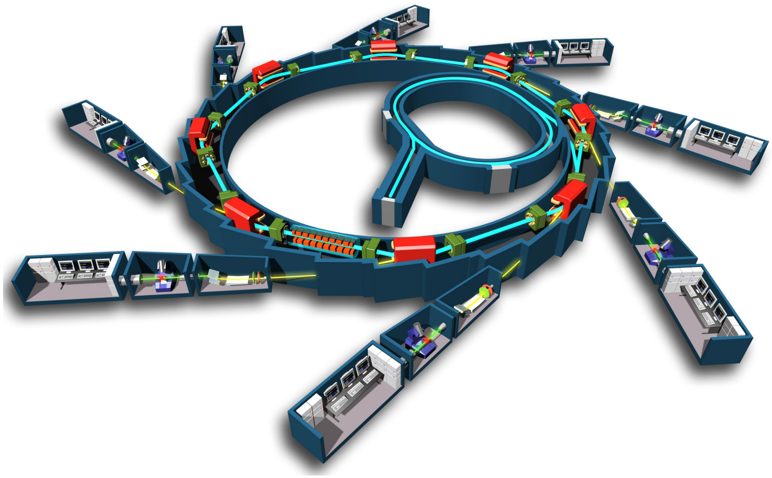

Figure 6.8: A synchrotron facility consisting of a main storage ring surrounding an injector system, and from which many beamlines protrude tangentially. Experiments are conducted at the ends of each of the beamlines (image courtesy of Synchrotron Soleil).

ring is quite large, having a circumference of hundreds of meters. Electrons are periodically supplied to the storage ring from an injector located inside the storage ring. Since the emitted radiation propagates out in straight lines, straight sections called beamlines radiate out tangential to the storage ring. Synchrotron radiation generated by electrons circulating in the storage ring is sent down each of these beamlines, at the end of which an experimental setup is waiting.

Synchrotrons have been particularly important in modern materials science because they provided the first tunable source of ultra-bright X-rays. X-rays are extremely useful in many areas of science because their wavelength corresponds to the scale of inter-atomic distances, making them ideal probes for studying the crystal structure of materials. The usefulness of synchrotron light sources quickly became evident to the research community, and there are now dozens of facilities designed specifically to generate synchrotron radiation. The experiments described in this section were conducted at the 3rd generation[1] synchrotron light source known as BESSY (Berliner Elektronenspeicherring-Gesellschaft für Synchrotrontrahlung), located in Berlin, Germany. Before discussing this study, I will give a quick overview of synchrotron radiation as a research tool.

---

[1] As with many technologies requiring a large initial investment, advancements occur in stages, often called "generations". 3rd generation light sources were designed to act as ultrabright X-ray sources, and employ advanced techniques which set them apart from older light sources.

Figure 6.9: The synchrotron light source BESSY, where these experiments were conducted (photo from http://www.bessy.de).

6.3.1 Generation of synchrotron radiation

In very general terms, an electromagnetic wave is a disturbance in an electromagnetic field, which (in vacuum) travels away from the disturbance at the speed of light. These waves are created/emitted by the acceleration of charged particles. The intensity of the electromagnetic wave is proportional to the acceleration, and if this acceleration is oscillatory – such as charges in an antenna driven by an alternating current, or electrons racing around the storage ring of a synchrotron – the frequency of the emitted radiation depends on the frequency of the oscillation. However, since the electrons in the synchrotron move at relativistic speeds, it is necessary to introduce the parameter γ, which comes into play in almost every equation describing relativistic physical phenomena. This parameter is defined by

$$\gamma = \left[1 - \frac{u^2}{c^2}\right]^{\frac{1}{2}}, \tag{6.11}$$

where u is the speed of an object (in this case an electron) measured in the laboratory frame, and c is the speed of light, which has the same value in every inertial frame[2].

---

[2] This is one of Einstein's postulates of special relativity.

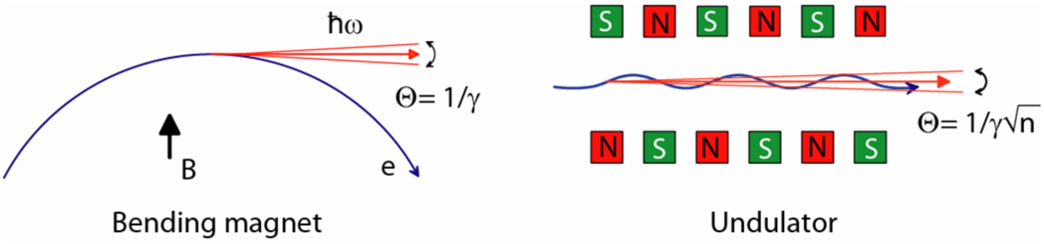

Figure 6.10: Types of magnets used to produce synchrotron radiation.

Synchrotron radiation is highly polarized in the plane of the circulating electrons, which are guided around the storage ring by powerful magnets. These storage "rings", however, are not actually round. In order to produce different kinds of radiation, different arrays of magnets are used in different sections along which the high-energy electrons travel. Bending magnets (see Fig.6.10) are located, not surprisingly, in the curved sections of the storage "ring", where the electron beam is bent (via the Lorentz force) around its path. As stated above, the frequency of the emitted radiation depends on the frequency of the oscillation of the charged particle. For an electron moving along a circular trajectory in a uniform magnetic field B, with effective (relativistic) mass $m = \gamma m_0$ (m_0 is the rest mass of the electron) the angular speed ω_e in the frame of the electron is

$$\omega_e = \frac{\gamma e B}{m_0} \tag{6.12}$$

and the emitted wavelength is

$$\lambda_e = \frac{2\pi m_0 c}{\gamma e B}. \tag{6.13}$$

After taking into account the Doppler shift[3], the frequency measured in the laboratory frame is

$$\lambda_L = \left(\frac{\lambda_e}{2\gamma}\right)\frac{2\pi m_0 c}{2\gamma^2 e B}. \tag{6.14}$$

This wavelength, however, is just the center of a very wide emission band, which can extend over many domains (from X-rays to infrared). At a synchrotron facility, the desired wavelength can be selected, providing a very broad range of photon energies that can be used in a wide variety of experiments.

Another method for producing synchrotron radiation is the use of an "undulator", which is used to produce very high brightness X-rays. An undulator is an array of

---

[3] the Doppler shifted frequency $f' = \gamma(1 - v/c)f$

magnets (Fig. 6.10) located along the straight sections of a storage ring. The magnet array causes the electrons to oscillate back and forth transverse to their direction of travel, emitting radiation along this path. The frequency of the emitted light depends on the period of the magnet array, thus the wavelength is on the order of the period of the array. In order to produce X-rays, which have wavelengths on the order of 1 Å, one might expect the period of the magnet array must also be on this scale, which is obviously impossible. However, recalling the relativistic speeds at which the electrons are traveling, the period of the magnet array is Lorentz contracted in the frame of the electron, thus shortening the period significantly. Furthermore, the radiation emitted in the frame of the electrons becomes Doppler-shifted toward higher frequency when observed in the lab frame. Therefore, not only is X-ray generation possible in a synchrotron, but the energy of the generated X-rays is tunable by the speed of the electrons and the strength of the magnetic field.

A third device used for producing synchrotron radiation is called a “wiggler”. A wiggler is essentially an undulator with a much stronger magnetic field. They are given different names, however, because they are used to produce different kinds of radiation. In an undulator, the magnetic field is relatively weak, creating a pulse that is long in time, but has a very narrow frequency band. Increasing the magnetic field (as in a wiggler) creates a series of very short pulses that are broad in frequency, rather than a long pulse centered around one fundamental wavelength. A wiggler is essentially equivalent to a series of bending magnets.

Synchrotron light is clearly a powerful, versatile source of radiation that can be tailored for use in a variety of experiments, such as X-ray absorption, circular dichroism spectroscopy, photoemission spectroscopy, etc. Due to the large number of beamlines at each synchrotron facility (there are 46 beamlines at BESSY) many types of experiments probing many different properties can be performed simultaneously at one facility. Two measurements using synchrotron radiation will be discussed here.

6.3.2 X-ray absorption spectroscopy

The absorption of X-rays is essentially the same as other absorption processes, but involve much higher-energy transitions. These transitions are typically from the inner “core” states (1s, 2s, 2p, etc.) to the continuum states (e.g. the conduction band), which exist above the Fermi energy, E_F. Such a transition can occur if the energy of the incident photon

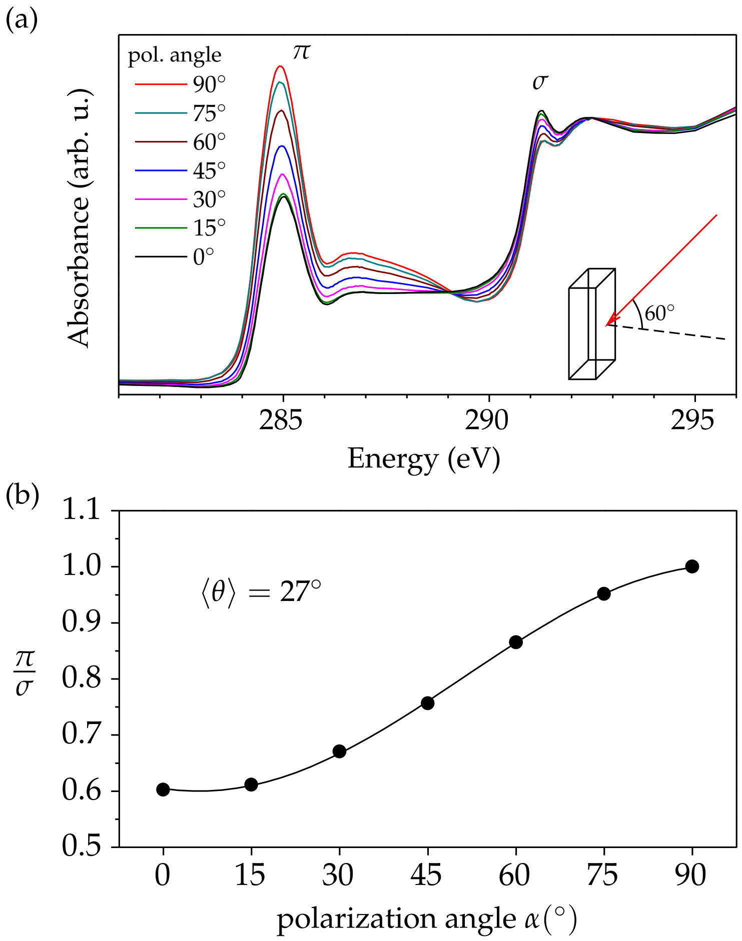

Figure 6.11: (a) X-ray absorption spectra near the core-edge for light incident at an angle of 60° and changing polarization angle. (b) Ratio of π to σ peak intensities as a function of polarization angle.

is larger than this energy difference. For carbon atoms, the 1s level is 284 eV below E_F, thus excitation of a 1s core electron to the continuum requires a photon for which $\hbar\omega > 284$ eV. This corresponds to a photon with a wavelength on the order of 1 Å, corresponding to an X-ray. By comparison, interband transitions in molecules are excited by the absorption of photons in the visible or UV range, which have energies of only a few electron volts.

X-ray absorption spectroscopy (XAS) is a technique to obtain chemical and structural information about a material. The strength of the absorption depends on the number of electrons that can contribute to the absorption process (i.e. the number of electrons occupying core levels), and the number of available (unoccupied) final states. Chemical bonding changes both of these parameters, and is reflected in the X-ray spectrum. The most dominant feature in the spectrum is the core-edge absorption peak, which marks the minimum energy at which a core-level electron can be excited into the continuum. XAS spectra obtained from our VA-SWNT samples is shown in Fig. 6.11a, where the X-rays were incident on the sample at an angle of 60° from normal, and the X-ray polarization was changed from 0 to 90° in 15° steps. The core edge, corresponding to a $1s \rightarrow \pi^*$ transition, is clearly visible at ~285 eV, and is strongly dependent on the polarization angle. The $1s \rightarrow \sigma^*$ transition can be seen at ~291 eV, and shows very little polarization dependence.

The $1s \rightarrow \pi^*$ and $1s \rightarrow \sigma^*$ transitions can be modeled by representing the distribution of SWNT axes by a Gaussian curve on a hemisphere (similar to the branch of an atomic *p*-orbital). The electric field vector $\vec{E}$ is then composed into parallel (E_P) and radial (E_R) components. The $1s \rightarrow \pi^*$ transition has no angular dependence, thus depends entirely on the radial part E_R. The $1s \rightarrow \sigma^*$ transition does have angular dependence, thus has contributions from both the radial and parallel components. Separating out these components [58] and integrating over all orientations yields the $1s \rightarrow \sigma^*$ contribution, $E_P + \frac{4E_R}{\pi^2}$. For a completely random distribution, these components are equal at 54.7°. The experimental data in Fig. 6.11 are fit when $\theta = 27°$, which means the SWNTs in the aligned film are distributed such that their average deviation from the substrate normal is approximately 27°. This value is in fairly good agreement with the value obtained by polarized optical absorption spectroscopy (24°). However, this method is likely to have more error because of the difficulty in orienting the sample so that it is exactly perpendicular to an invisible beam of synchrotron radiation.

6.3.3 Photoemission spectroscopy

X-rays can also excite core electrons into the continuum, producing photoelectrons. These transitions are generally direct, meaning wavevector $\vec{k}$ is conserved. However, X-rays have sufficient momentum that nonvertical excitations are also possible. Analysis of the momentum and energy distributions of the photoelectrons allows the electronic dispersion relations $E(\vec{k})$ to be determined, from which one can determine the binding energies of the original electronic states. This makes photoemission spectroscopy (PES) an important analytical tool for obtaining information on the electronic states of materials. The theory describing PES can be found in in-depth reviews of the subject [59, 60].

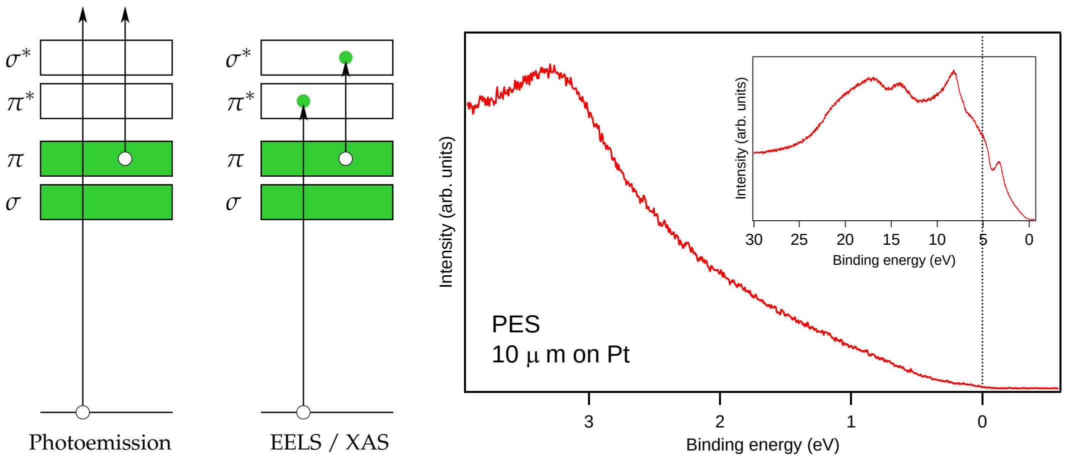

Figure 6.12: (left) Electronic excitations measured by Photoemission, X-ray Absorbance, and EELS spectroscopies (reproduced from [65]). (right) A photoemission spectrum from vertically aligned SWNTs, which shows no clear Fermi edge. The complete valence band spectrum is shown in the inset.

The photoemission spectrum shown in Fig. 6.12 is from a film of vertically aligned SWNTs. The excitation energy was 125 eV. The lack of a clear step at the Fermi edge, indicated in Fig. 6.12 by the dotted line, may indicate the SWNTs exhibit Luttinger liquid behavior [61]. A Luttinger liquid is the state resulting from the breakdown of Fermi liquid theory at low dimensions. This causes the quasi-particles, which interact in a Fermi liquid, to split into into separate charge and spin modes, which have a bosonic nature [62]. The result is a momentum distribution which exhibits a smooth power law, rather than having a "step" as in a Fermi liquid. This step shows up at the Fermi energy in photoemission spectra, thus the absence of any noticeable step in the spectrum for our VA-SWNTs indicates Luttinger liquid behavior. This phenomenon has been previously reported for SWNTs [61, 63, 64], and the spectrum shown in Fig. 6.12 bears many similarities to that in Reference [63]. However, this has not been confirmed for our VA-SWNTs.

Chapter 7

Electron energy-loss spectroscopy

In the previous chapter I discussed spectroscopic techniques based on the interaction of electromagnetic radiation with matter. In this chapter I focus on a technique called electron energy-loss spectroscopy (EELS), which uses accelerated electrons to probe the electronic system of a solid. In EELS, high-energy electrons are either reflected from or transmitted through a material, transferring energy to the solid in the process. More recent methods (including that employed in this study) primarily use transmitted electrons, whose incident energy is between 100 and 200 keV. The incident electrons transfer energy to the system via the Coulomb potential, thus the possible excitations which occur (i.e. excitation of quasi-particles, which couple to the moving electron[1]) are similar to optical absorption or scattering processes. One major difference, however, is that the incident electrons have a much larger momentum than photons with the same energy, thus in EELS *both energy and momentum* can be measured (a 10 eV electron has a wavevector of about 10^8 cm^{-1}, whereas a 10 eV photon has a wavevector 1000 times smaller). This means the dispersion relations can be measured over the entire Brillouin zone.

7.1 EELS theory

Since EELS is based on an inelastic scattering process, both energy and momentum conservation apply. The scattering geometry is shown in Fig. 7.1, where electrons with energy E_0, and momentum k_0 are incident on an electon-transparent sample. Since the en-

---

[1] Formally, this process is similar to Raman scattering, except that in EELS the probing electron interacts with the quasi-particles of the solid directly, rather than via an intermediate exciton state [15].

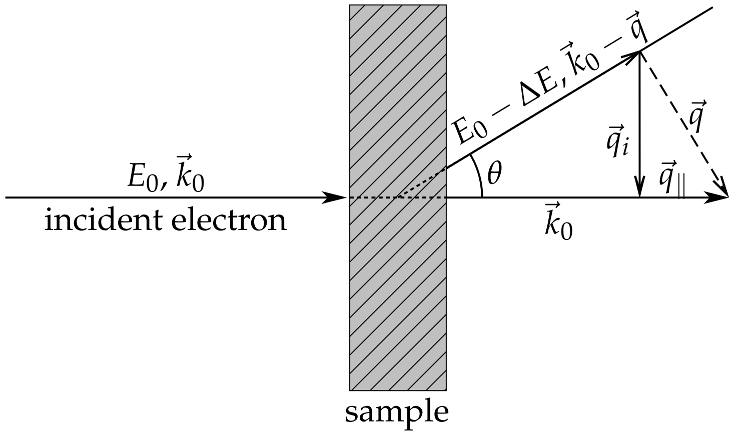

Figure 7.1: Scattering geometry in electron energy loss spectroscopy (reproduced from [66])

ergy loss $\Delta E \ll E_0$, the scattering angle θ is small, therefore the energy and momentum relations can be approximated by

$$q_{\perp} = (k_0 - q)\sin\theta \approx k_0 - q \tag{7.1}$$

$$q_{\parallel} \approx k_0 - (k_0 - q) \approx k_0 \frac{\Delta E}{2E_0} \ll q_{\perp} \tag{7.2}$$

where $q_{\parallel}$ and $q_{\perp}$ refer to directions parallel and perpendicular to the electron beam.

Now consider the dynamic form factor (or power spectrum), $S(q,\omega)$, which describes the energy spectrum [15]. For the electronic system,

$$S(q,\omega) = \frac{q^2 \epsilon_0 \mathcal{V}}{e^2} \mathrm{Im}\{-\frac{1}{\epsilon(q,\omega)}\}. \tag{7.3}$$

The factor in front is the scattering volume $\mathcal{V}$ and the inverse of the Fourier transform of the Coulomb interaction. The imaginary part, $\mathrm{Im}\{-\frac{1}{\epsilon(q,\omega)}\}$, is known as the *energy loss function*, where $\epsilon(q,\omega)$ is the complex dielectric function. The loss function is related to the scattering cross-section by

$$\frac{d^2\sigma}{d\Omega d\hbar\omega} \frac{4\epsilon_0 \mathcal{V}}{e^2 r_B^2 q^2} = \mathrm{Im}\{-\frac{1}{\epsilon(q,\omega)}\}. \tag{7.4}$$

This relationship allows us to determine the loss function *directly from the scattering experiment*. A Kramers-Kronig analysis (see Appendix C) is then performed to obtain the dielectric function $\epsilon(q,\omega)$.

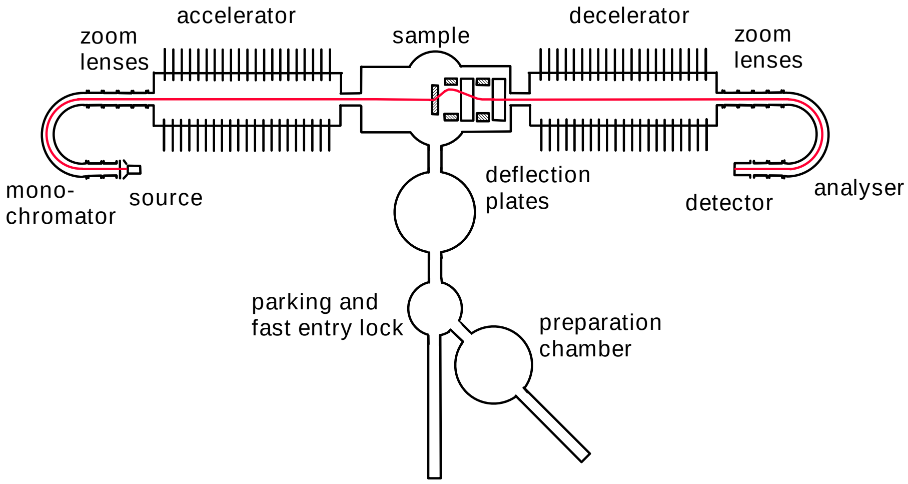

Figure 7.2: The EELS spectrometer, having good momentum and energy resolution, used to analyze the energy loss ([66]).

7.2 Experimental results

The spectrometer used in these EELS measurements, shown in Fig. 7.2, is a purpose-built system having good energy *and* momentum resolution [66]. The operating pressure of the spectrometer is 10^{-5} to 10^{-6} Pa. Before arriving at the sample, electrons from the source pass through a monochromator, and are then accelerated to 170 keV. The angular distribution of the transmitted (scattered) electrons can be selected by changing the voltage applied to the deflection plates, allowing one to analyze interactions with a specific momentum transfer. The momentum-selected electrons are decelerated before arriving at the detector. Good energy resolution (down to 0.05 eV) is obtained by precisely matching the acceleration and deceleration voltages.

7.2.1 Transfer of VA-SWNT films

A promising new method was developed by Murakami and Maruyama [67] that shows great potential to allow various measurements and applications of VA-SWNTs that were previously impossible. Their method is the removal of VA-SWNT films from the substrate on which they were grown (typically quartz glass) and transfer of these films (the same VA-SWNTs as used in this research) onto arbitrary substrates simply by submersion into hot water. The VA-SWNT films essentially peel away from the substrate when the

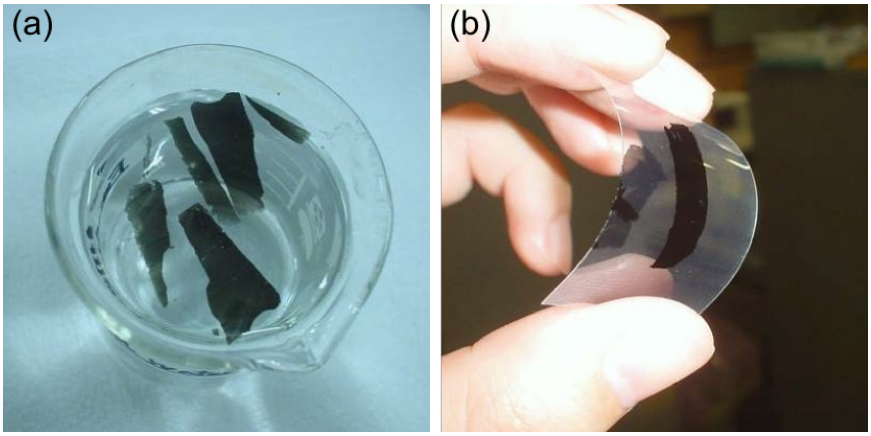

Figure 7.3: (a) Floating VA-SWNT films after removal by the hot-water assisted method, and (b) a VA-SWNT film after transferred onto a flexible plastic substrate (from [67]).

substrate is submerged into hot water, and remain floating on the surface of the water bath (see Fig. 7.3a). The films can then be transferred onto any arbitrary surface (such as plastic, in Fig. 7.3b) simply by submerging the new substrate into the water, positioning it under the floating VA-SWNT film, and drawing it out in a way that the film contacts the substrate. Observation by SEM [67] have shown that the SWNTs remain vertically aligned after undergoing this hot-water assisted removal and transfer process, with no observable change in morphology. It should be noted, however, that this is not the case for all vertically aligned SWNTs. The VA-SWNTs produced by the "supergrowth" method have been reported to absorb water [68], condensing into a solid-like mass.

7.2.2 EELS in the low-energy region

The large momentum of electrons used in EELS can be used to probe excitations across the entire Brillouin zone. At the limit of zero momentum transfer ($q \rightarrow 0$), EELS can be considered a direct analog to optical absorbance, because only vertical transitions ($\Delta k \approx 0$) are possible. Therefore, as an extension of the optical measurements described in Chapter 6, this study focuses on small-k excitations.

Below ~25 eV, carbon systems primarily support two types of excitations: interband transitions and plasma oscillations. The interband transitions are single-particle excitations, just as in optical absorbance, and appear in EELS spectra as relatively sharp, localized peaks. In anisotropic materials, longitudinal plasmon modes dominate, which

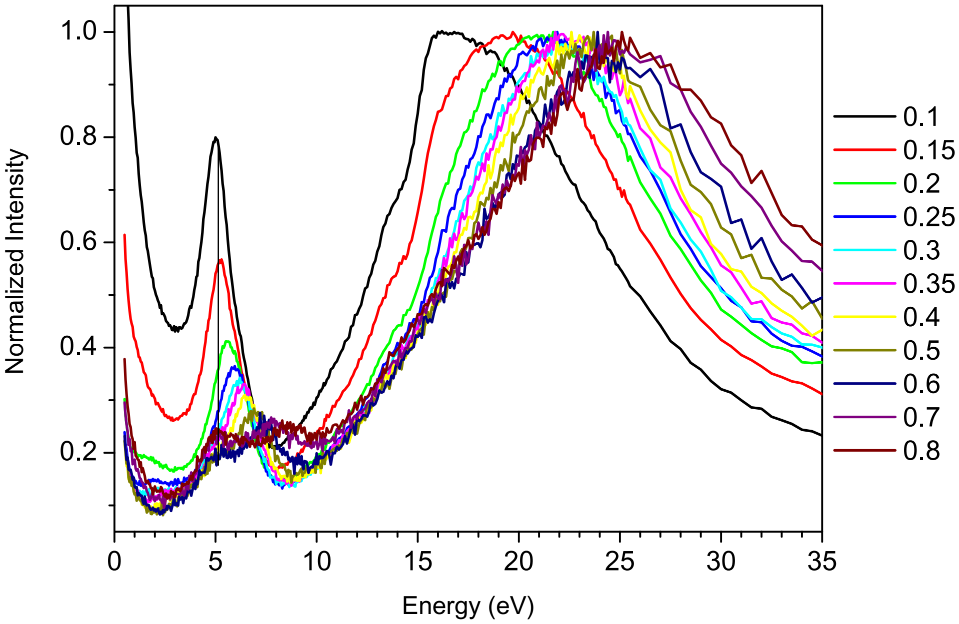

Figure 7.4: EELS spectra showing the π and σ plasmon peaks for values of momentum transfer between 0.1 and 0.8 Å $^{-1}$.

can be excited by traveling electrons [65]. Photons, on the other hand, excite transverse modes, thus a strong plasmon signal is suppressed in optical interactions, but are very strongly excited by an electron beam. These oscillations are caused by coupling of the valence electrons to the passing electrons, and have angular frequency

$$\omega_p = \sqrt{\frac{ne^2}{\epsilon_0 m}}. \tag{7.5}$$

ω_p is the plasma frequency, and e and m are the effective charge and reduced mass of the oscillator, respectively. This collective excitation is equivalent to the excitation of quasi-particles called *plasmons*, where a plasmon is a quantum of plasma oscillation (much as a phonon is a quantum of lattice oscillation). A collective plasma oscillation appears in EELS spectra as a broad, dispersive peak centered at ω_p. Experimentally obtained EELS spectra for different degrees of momentum transfer are plotted in Fig. 7.4. The two peaks correspond to plasmon excitations in the VA-SWNTs. The narrow peak just above 5 eV corresponds to an oscillation of the π electrons, while the broad peak, which disperses from

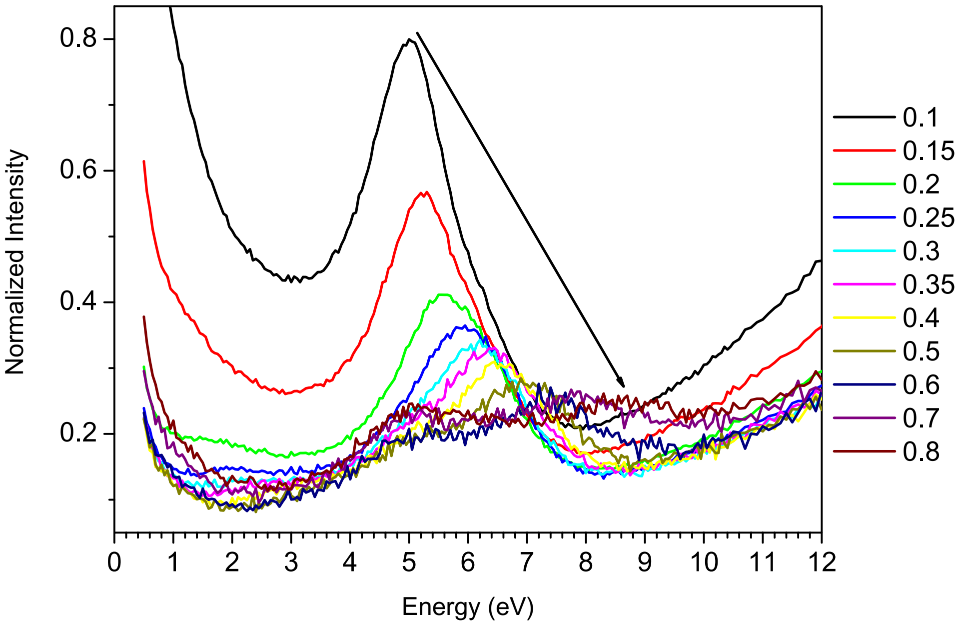

Figure 7.5: EELS spectra showing large dispersion of the π plasmon energy with changing momentum transfer

15 to 25 eV, arises from a plasma oscillation in the electrons occupying the σ bonds. To compare with our optical spectroscopy results, we take a closer look at the energy region below 10 eV.

The spectra shown in Fig. 7.5 are the first EELS spectra obtained from this type of geometry (i.e. SWNTs vertically aligned on a substrate). In order to ensure electron transparency, typical EELS samples are usually $\leq$ 100 nm thick. However, due to the very low density of these VA-SWNT films, samples several μm thick are still electron transparent. Unfortunately, the 2 μm-thick VA-SWNT film used in these measurements was not thick enough to obtain a strong signal from the interband transitions, which are washed out by the tails of the strong peak at 0 eV arising from elastically scattered electrons. The π plasmon peak, however, is clearly observed, and the π plasmon energy for small q (~5 eV) corresponds well to the optical absorbance data (Chap. 6). One very interesting result of this experiment is the dispersion of this peak with momentum transfer. The peak energy in this sample of VA-SWNTs exhibits momentum-dependent dispersion of the π

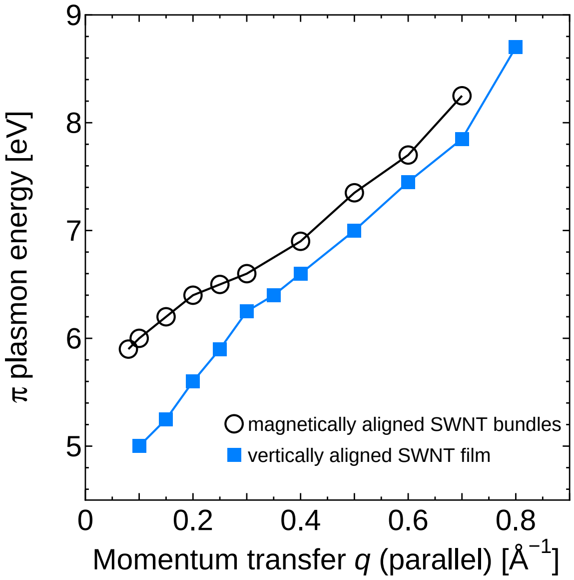

Figure 7.6: Dependence of the π plasmon energy on momentum transfer for magnetically aligned SWNTs (open circles) and a VA-SWNT film (closed squares). The data for the magnetically aligned sample is from [69].

plasmon that is considerably larger than for aligned SWNT bundles [69]. The plasmon energy vs. momentum transfer is plotted in Fig. 7.6. The dispersion to lower energy for small q is due to suppressed tube-tube interactions. Since one does not expect the packing density of SWNTs in the bundles to change (as this is due to Van der Waals interactions), this result indicates the bundles themselves are very small, or there is an unusually large number of isolated SWNTs dispersed throughout the bundle.

7.2.3 Electron diffraction

By setting the energy loss to zero, it is possible to carry out electron diffraction measurements inside the EELS spectrometer. As mentioned above, this spectrometer has both energy and momentum resolution, but does not have spatial resolution (as in a TEM). Thus it is impossible to obtain typical electron diffraction patterns. One can, however, obtain the intensity profile for various degrees of momentum transfer q. Two such profiles are shown in Fig. 7.7, measured parallel and perpendicular to the SWNT alignment direction. There are two peak structures in this spectrum. The (110) Bragg peak from graphite is found at 3 Å^{-1}, and the (100) Bragg peak at 5.4 Å^{-1}. The degree to which the sample is

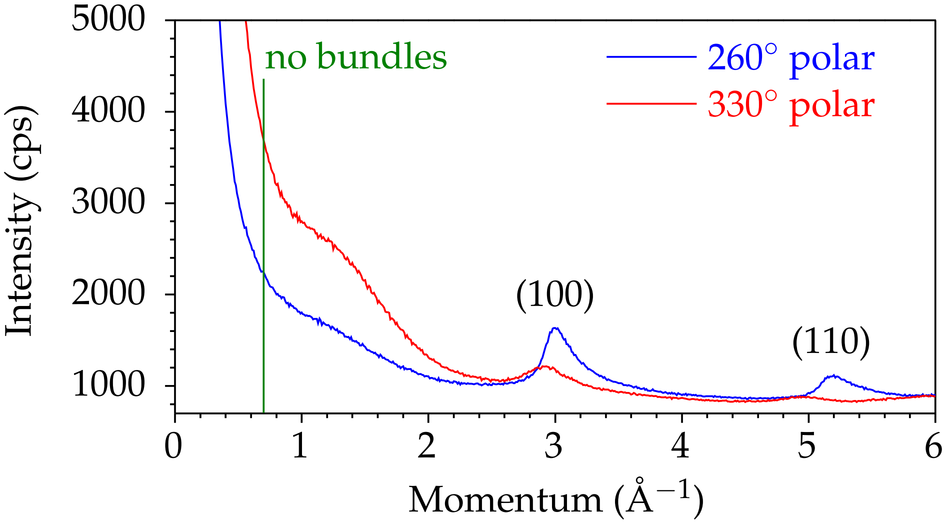

Figure 7.7: Electron diffraction intensity profiles for near-normal (blue) and low-angle (red) orientations. The armchair and zigzag peaks are clearly visible, but no bundle peaks appear in the low-q region.

ordered can be estimated from the *mosaic spread*, which is obtained by plotting the intensity of one of the peaks in the diffraction spectrum for all polar angles. This is shown in Fig. 7.8 (black line). The mosaic spread was obtained using the (100) peak at 3 Å^{-1}. Fitting the data yields a full-width at half maximum (FWHM) of approximately 65°. The red curve in Fig. 7.8 was obtained by calculating the mosaic spread using the 27° obtained from XAS measurements, and is in good agreement. However, both peaks in the calculated spectrum have equal height, whereas the peak heights in the measured spectrum are different. This seems to indicate the SWNTs have a preferred leaning direction, but may also be due to imperfect alignment of the substrate normal with the direction of incident electron beam.

The diffraction spectra in Fig. 7.7 are very similar to those obtained from magnetically aligned SWNT films [69], There is, however, one major exception, and that is no peaks are found in the low-q region (below 2 Å^{-1}). It has been well established that low-q diffraction peaks indicate bundling of SWNTs [27, 28, 70, 71]. The spectrum for this VA-SWNT film, however, shows a weak, broad hump near 1.2 Å $^{-1}$, which may be related to the large diameter distribution of the SWNTs [37], but the most prominent bundle peak (which should be found at 0.4 – 0.5 Å^{-1}) is absent. The absence of the bundle peak at low q does not mean there are no bundles in this sample, as surely there must be, but the

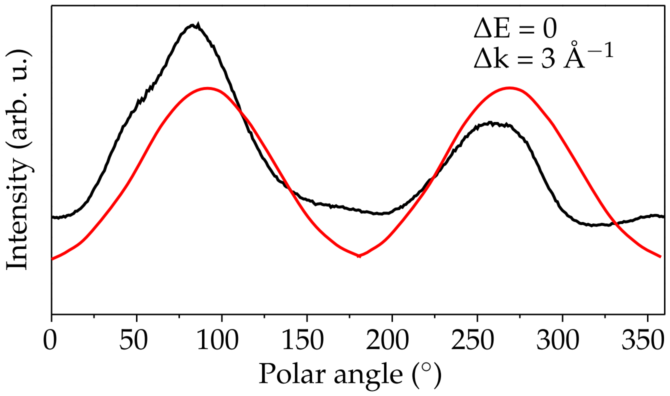

Figure 7.8: The angular spread of the zigzag peak located at ∼3 Å^{-1} in the electron diffraction spectra, and a calculated spread (red line) corresponding to an average deviation of 27°.

degree of bundling may be less than SWNTs prepared by other methods. Insignificant bundling would support the EELS results presented above, but direct observation by TEM is necessary to accurately characterize the internal structure, and is the final topic of this thesis.

Chapter 8

Transmission Electron Microscopy

The research presented in this thesis began shortly after realizing the synthesis of vertically aligned SWNT films [31] by the alcohol CVD method [26]. As a result, the initial characterization by electron microscopy [31] predate this work, but some new methods and results have since become available. In particular, the ability to prepare freestanding, vertically aligned SWNT films for transmission electron microscope (TEM) observation provided a new perspective on the internal structure of these VA-SWNT films. Findings based on these observations are presented in this chapter.

8.1 Observation by TEM

Typical preparation of SWNTs for TEM observation usually involves dispersion of SWNTs in a solution such as acetone, which is then dropped onto a TEM grid. The solution evaporates, leaving only the dispersed SWNTs behind. This is a simple method that allows for good imaging of the dispersed SWNTs and ensured electron transparency, but this method clearly leaves the sample in a state very much disturbed from its as-grown state. In this study, we used the hot-water-assisted VA-SWNT film transfer method [67] described in Section 7.2 to mount a VA-SWNT onto a TEM grid (Fig. 8.1), allowing a unique view along the alignment direction of the vertically aligned films. Figure 8.2 shows an SEM image of a VA-SWNT film after being transferred onto a TEM grid. It is clear in this image that vertical alignment is conserved during transfer onto the TEM grid. Using this sample preparation procedure made possible the first observations along the alignment direction of undisturbed, vertically aligned SWNTs.

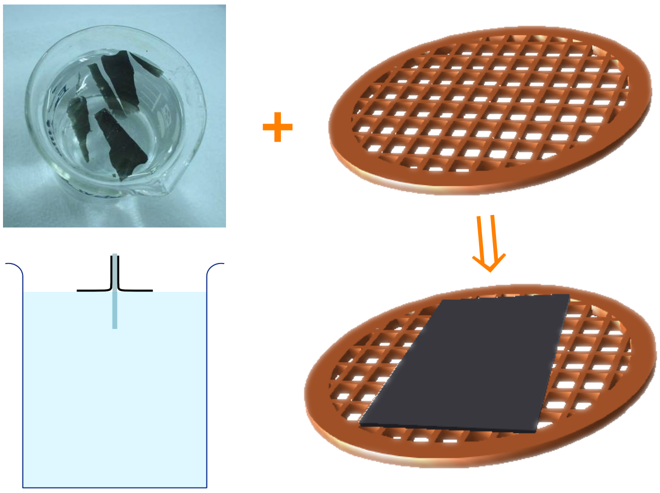

Figure 8.1: Using the hot-water method [67] to transfer a VA-SWNT film onto a TEM grid

A 2-μm-thick VA-SWNT film that had been transferred onto a TEM grid by the aforementioned hot-water assisted technique (Fig. 8.1) was observed by TEM, looking along the alignment direction. The images obtained are shown in Fig. 8.3. In the lower magnification images (a-b) the film appears quite uniform, except for the damaged portion near the top of the image. In (b), many dark spots can be seen dotting the image. One might expect these spots to be metal catalyst particles, or amorphous carbon deposits, but further magnification (c) shows these are, in fact, cross-sections of small SWNT bundles. Since the perspective in these images is along the alignment direction, many such cross-sections can be seen. These bundles, however, are much smaller than expected, and contain only a few (usually between 3 and 10) SWNTs. A higher magnification image of a few bundle cross-sections is shown in (d).

8.1.1 Unexpectedly small bundles

It is well-known that most synthesis methods tend to produce large bundles of SWNTs, such as those shown in Fig. 4.1. This bundling is attributed to Van der Waals interactions between the tubes [72, 73]. As discussed in Chapter 2, most of the unique properties of SWNTs arise from their one-dimensional nature. Inter-tube interactions with surrounding SWNTs in a bundle alter this one-dimensional nature, thus bundled SWNTs

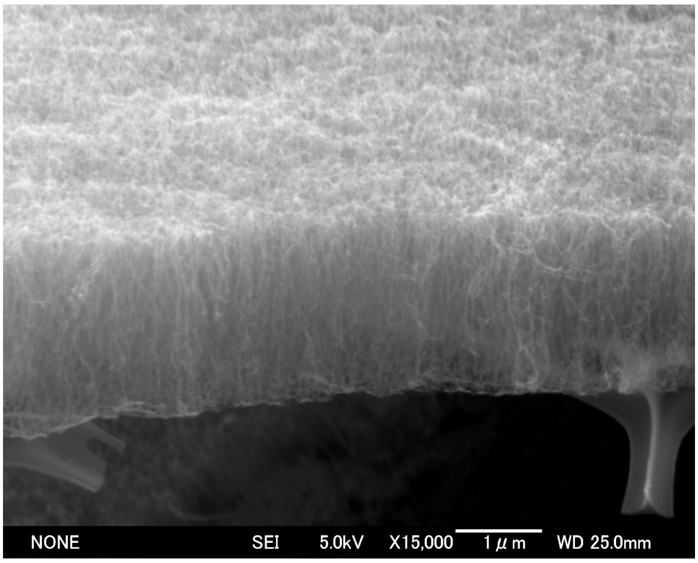

Figure 8.2: A VA-SWNT film after being transferred onto a TEM grid. The SWNTs remain vertically aligned after the transfer process.

more closely resemble bulk material than isolated SWNTs. This bundle effect is, of course, undesirable for many measurements of fundamental properties of SWNTs, as well as applications that rely on the unique 1D properties of SWNTs. Post-synthesis separation of bundles (by sonication, etc.) is almost certain to damage the SWNTs, thus is not a viable solution. The EELS presented in the previous chapter, however, indicate that it may be sufficient to obtain SWNT bundles that are sufficiently small that the inter-tube bundling effects are negligible, rather than the more challenging task of obtaining *individual* SWNTs.

Although TEM samples are usually ≤ 150 μm in thickness, in order to ensure electron transparency, the VA-SWNT film shown in Fig. 8.3, however, was 2 μm thick. Due to the low density of the film it is not unrealistic that this sample is electron transparent, but no structures are visible before or behind the region in focus. The explanation for this is the images shown in Fig. 8.3 were taken at 300 keV, while in most cases SWNTs are imaged at 120 or 200 keV to prevent damage by the electron beam. Most of the images were taken at a moderate magnification ($\sim$ 250,000X), thus minimal damage is expected from the electron beam. However, in order to confirm the small bundle size is not unique to this sample, a different film (7 μm thick) was observed at both 120 and 200 keV. The images are shown in Fig. 8.4. In this film, small bundles, as well as some dispersed SWNTs, are visible. This

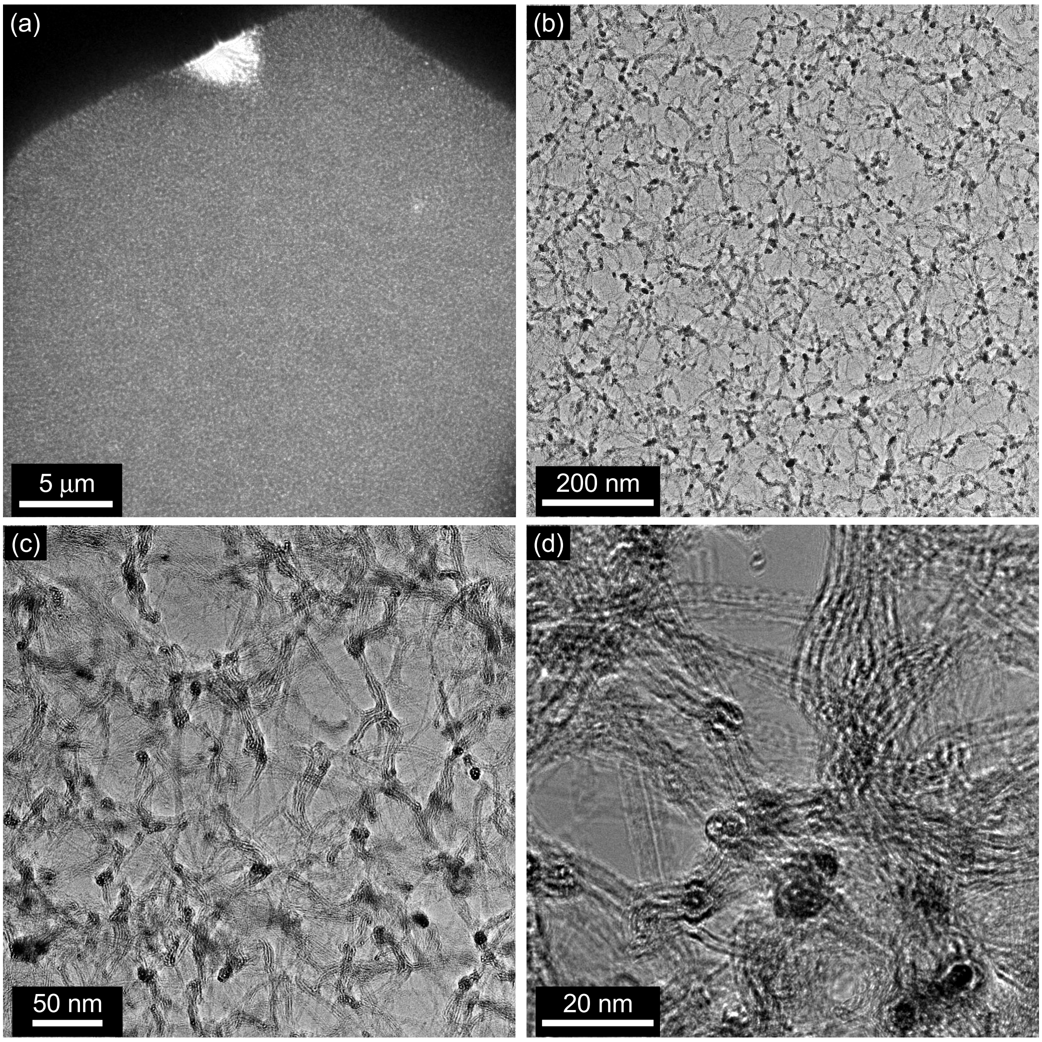

Figure 8.3: TEM images of a 2 μm-thick VA-SWNT film, looking along the alignment direction. As the magnification increases, many bundle cross-sections become visible (b), and are found to contain only a few SWNTs per bundle (c)-(d). All images taken at 300 keV

is in agreement with the results from the 2 μm sample, indicating the small bundle size is common to VA-SWNTs produced by the ACCVD method. Furthermore, out-of-focus background and foreground structures that were absent in the 300 keV images become visible when the acceleration voltage is lowered. The 7 μm film imaged in Fig. 8.4 may be a bit too thick, which is why the images taken at 200 keV turned out better than those as 120 keV (better transmission of the electron beam), but the observed structure is essentially the same.

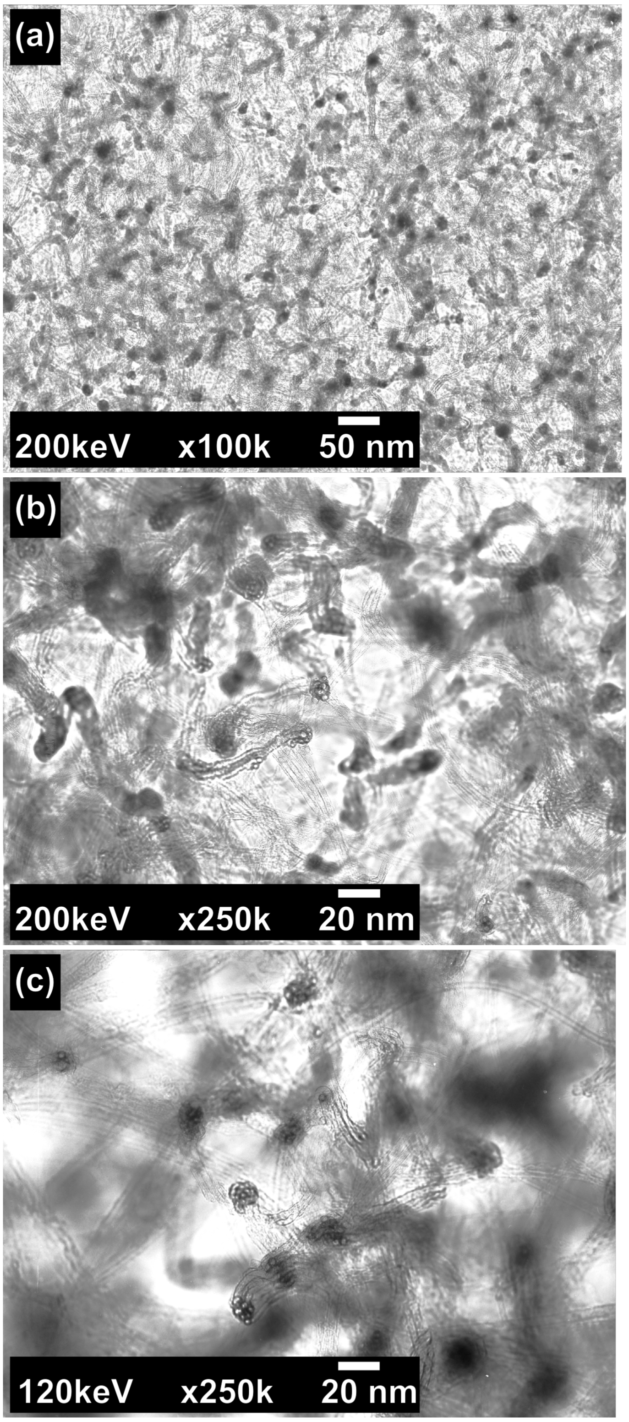

Figure 8.4: TEM images of a 7 μm-thick VA-SWNT film taken at (a)-(b) 200 keV, and (c) 120 keV. Small bundles are also found in this film, but the lower energy reveals more foreground/background structures.

As mentioned above, bundling makes SWNTs more closely resemble bulk carbon than one-dimensional materials. The lack of significant bundling observed in these vertically aligned films helps to explain the electronic and optical properties of the VA-SWNT films discussed in the preceding chapters. This new perspective on the internal structure of VA-SWNTs is expected to aid in developing new applications and in performing new measurements on the fundamental properties of SWNTs.

Chapter 9

Summary

This research conducted during the course of this PhD led to various improvements to the synthesis of vertically aligned single-walled carbon nanotubes (VA-SWNTs) from alcohol. In addition to increasing the overall yield of VA-SWNTs, a new optical absorption measurement method was developed that allowed the growth process to be studied during CVD synthesis. Using this *in situ* method, an analytical description of the growth process was developed, which describes VA-SWNT film growth based on the initial growth rate and the catalyst lifetime. This model also accounts for burning of the VA-SWNTs, which can occur if air is present in the growth chamber during CVD. However, burning of the SWNTs became negligible when the leak was suppressed. This *in situ* method is a promising method to better understand how the growth environment affects the catalyst activity, which should lead to a better understanding of the catalytic reaction and improved overall growth.

The structure and optical properties of VA-SWNTs were also investigated during this study. It was shown that the absorption properties of vertically aligned SWNT films exhibit significant polarization-dependent anisotropy, due to the alignment of the SWNTs. This was investigated by polarized optical and X-ray absorption spectroscopy. Based on these measurements, the degree of alignment of the films was determined to be approximately 25-27° from the substrate normal. Further measurements using electron diffraction are also in agreement with this value.

Electron diffraction spectra did, however, yield an unexpected result. Despite the tendency of SWNTs to form into bundles, no bundle peak was observed in the scattering spectra, indicating minimal bundling of the SWNTs in the vertically aligned film.

Momentum- and energy-resolved electron energy-loss spectroscopy (EELS) revealed an unusually large dispersion of the plasmon energy in the π electron system of VA-SWNTs. This large dispersion is similar to that expected for isolated SWNTs, adding support to the evidence for insignificant bundling. Subsequent observation of the VA-SWNTs by transmission electron microscopy confirmed the films are composed primarily of small bundles. The VA-SWNTs were observed along the alignment direction, revealing many bundle cross sections. These bundles were generally $\leq$ 10 nm in diameter, typically containing 3-10 SWNTs. Whether or not these bundles are indeed small enough to behave electronically as individual SWNTs requires further investigation, but many interesting new studies and applications are expected to follow from this research.

Appendix A

The tight-binding approximation

Two Bloch orbitals, constructed from the atomic orbitals for the two inequivalent atoms A and B in the grahene unit cell (Fig. 2.2a), provide the basis for a graphene sheet

$$\psi_j = \frac{1}{\sqrt{N}} \sum_{R_\alpha} e^{ikR_\alpha} \phi_j(r - R_\alpha), \quad (\alpha = A, B). \tag{A.1}$$

The summation is taken over the atomic site coordinate R_α for both atoms A and B.

To determine the energy eigenvalues and wavefunction, we need to solve the general equation

$$\mathcal{H}\psi = ES\psi, \tag{A.2}$$

where $\mathcal{H}$ is the tight-binding Hamiltonian and $\mathcal{S}$ is the overlap integral matrix. In order to obtain a solution, it is required that the determinant $|\mathcal{H} - E\mathcal{S}| = 0$.

When $\alpha = \beta = A$, we obtain the diagonal matrix element

$$\mathcal{H}_{AA}(r) = \frac{1}{N} \sum_{R,R'} e^{ik(R-R')} \langle \phi_A(r - R') | \, \mathcal{H} \, | \phi_A(r - R) \rangle \, . \tag{A.3}$$

This equation can be split into two parts, with the main component coming from $R' = R$, and giving the $2p$ energy level, E_{2p}. The second term describes nearest-neighbor contributions where $r \geq R' = 2a$. The nearest-neighbor Hamiltonian is (to a first approximation)

$$\begin{aligned} \mathcal{H}_{AB}(r) &= \frac{1}{N} \sum_{R} \Big\{ e^{-ika/2} \langle \phi_A(r - R) | \, \mathcal{H} \, | \phi_B(r - R - a/2) \rangle \\ &\quad + e^{ika/2} \langle \phi_A(r - R) | \, \mathcal{H} \, | \phi_B(r - R + a/2) \rangle \Big\} \\ &= 2\gamma_0 \cos(\frac{ka}{2}), \end{aligned} \tag{A.4}$$

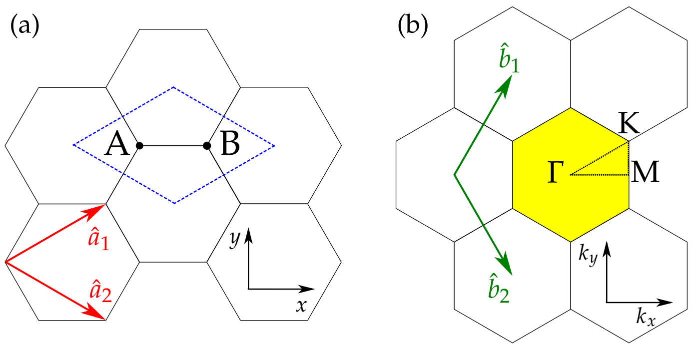

Figure A.1: (a) The unit cell enclosed by the dashed rhombus contains two atoms A and B. (b) The Brillouin zone of graphene (yellow region), and high symmetry points M, K, and Γ. $\hat{a}_i$ and $\hat{b}_i$ (i = 1,2) are the corresponding unit vectors.

where γ_0 is the neighbor transfer integral

$$\gamma_0 = \langle \phi_A(r-R) | \, \mathcal{H} \, | \phi_B(r - R \pm a/2) \rangle \, . \tag{A.5}$$

If the three nearest B atoms to an A atom are located at $\vec{R}_i$, i = (1,2,3), we can write

$$\mathcal{H}_{AB} = \gamma_0 \left(e^{i\vec{k}\cdot\vec{R}_1} + e^{i\vec{k}\cdot\vec{R}_2} + e^{i\vec{k}\cdot\vec{R}_3} \right) = \gamma_0 f(k) \tag{A.6}$$

where $f(k)$ is the function

$$f(k) = e^{ik_x a/\sqrt{3}} + 2e^{-ik_x 1/2\sqrt{3}} \cos\left(\frac{k_y a}{2}\right) . \tag{A.7}$$

Since $f(k)$ is complex, and the Hamiltonian operator is Hermitian, we know $\mathcal{H}_{BA} = \mathcal{H}^*_{AB}$ (where * denotes the complex conjugate). Furthermore, the overlap integral $\mathcal{S}$ can be given by $\mathcal{S}_{AA} = \mathcal{S}_{BB} = 1$,and $\mathcal{S}_{AB} = \mathcal{S}^*_{BA} = sf(k)$. Using these forms we can now write $\mathcal{H}$ and $\mathcal{S}$ as:

$$\mathcal{H} = \begin{pmatrix} E_{2p} & \gamma_0 f(k) \\ \gamma_0 f(k)^* & E_{2p} \end{pmatrix} ; \quad \mathcal{S} = \begin{pmatrix} 1 & sf(k) \\ sf(k)^* & 1 \end{pmatrix} . \tag{A.8}$$

By solving the secular equation det($\mathcal{H} - E\mathcal{S}$) = 0 and using the above forms for $\mathcal{H}$ and $\mathcal{S}$, we can obtain the eigenvalues of the energy dispersion relations as a function of k_x, k_y, and $\omega(\vec{K})$:

$$E_{g2D}(\vec{k}) = \frac{E_{2p} \pm \gamma_0 \omega(\vec{k})}{1 \pm s\omega(\vec{k})} , \tag{A.9}$$

where the ± indicates bonding/antibonding π/π^* bands, respectively.

Appendix B

Absorbance fitting program

The following program is written in the `MATLAB`™ programming language, and was used to fit *in situ* optical absorbance data.

```
close
clear all
clc
%+++get data file
cd 'e:/research/Data and Analysis/in situ optical/data'\ % main directory
[srcfile,srcpath] = uigetfile('*.txt','Select data file to process');
% break down filename into bits
[junk, filename, ext] = fileparts(srcfile);
% output directory
cd 'E:/research/Data and Analysis/in situ optical/analysis/burning'\
%+++begin recording program output
diary_pref = ['burn_info-'];
diary_ext = ['.txt'];
diaryname = horzcat(diary_pref,filename,diary_ext);
diary(diaryname);
%+++load data from file (col 1 is data point, col 2 is transmitted intensity)
% skip header
[data_pt intensity] = textread([srcpath, srcfile], '%f %f', 'headerlines', 23);
fprintf('Fitting of VASWNT growth data (including burning effects) based on
```

```
in situ optical absorbance measurement.\n’)
fprintf(’Performed on %s\n’,date)
fprintf(’Author: Erik Einarsson\n’)
fprintf(’\nData file processed: \n%s%s\n’,srcpath,srcfile)
%+++compute the time from the data points (and convert into minutes)
time_step = textread([srcpath, srcfile], ’%*s %d %*s’, 1, ’headerlines’,
6)/1000; % get time step from input file header
time = data_pt*time_step/60;
%++calculate absorbance and sparse array for output plot
%get max intensity from input file header (and convert from mW into W)
Imax = textread([srcpath, srcfile], ’%*s %f %*s’, 1, ’headerlines’,
14)/1000;
absorb = -log10(intensity/Imax);
abs_time = [time,absorb];
file_length = length(time);
step = round(file_length*0.02);
p_time = time(3:step:file_length);
p_absorb = absorb(3:step:file_length);
p_abs_time = [p_time,p_absorb];
%+++define fitting model and perform fitting (a = gamma_0/abs_to_thick)
fitmodel = fittype(’a*tau*(1-exp(-x/tau))’);
opts = fitoptions(fitmodel);
opts.Startpoint = [0.5 3];
opts.Lower = [0 0];
% opts.Robust = ’on’;
[fitresult,gof1] = fit(time,absorb,fitmodel,opts);
%+++define fitting model (with burning) and perform fitting
%+++(a = gamma_0/abs_to_thick, beta is beta/abs_to_thick)
burnmodel = fittype(’a*tau*(1-exp(-x/tau))-beta*x’);
opts = fitoptions(burnmodel);
opts.Startpoint = [0.5 3 0.000001];
opts.Lower = [0 0 0];
% opts.Robust = ’on’;
```

```
[burnresult,gof2] = fit(time,absorb,burnmodel,opts);
%+++write output file
prefix = ['burnfit-'];
data_ext = ['.dat'];
outputfile = horzcat(prefix,filename,data_ext);
save(outputfile, 'abs_time', '-ascii', '-tabs')
fprintf('\nAbsorbance vs. time data output to: \n E:/research/
Data and Analysis/in situ optical/analysis/burning/%s\n',outputfile);

%+++display results (to be recorded to diary file)
% define absorbance to thickness conversion parameter (per side, in um)
abs_to_thick = 6.7811;
a_max = max(absorb);
a_final = absorb(file_length);
h_max = a_max*abs_to_thick;
h_final = a_final*abs_to_thick;
delta_h = h_final-h_max;
gamma_0 = burnresult.a*abs_to_thick;
beta = burnresult.beta*abs_to_thick;
ratio = beta/gamma_0*100;
t_c = -burnresult.tau*log(beta/gamma_0);

fprintf('\n\nFit results (including beta):\n')
fprintf('\nMaximum absorbance:\t%2.3f\n',a_max)
fprintf('Final absorbance: \t%2.3f\n',a_final)
fprintf('\nMaximum film thickness (per side):\t%2.2f um\n',h_max)
fprintf('Final film thickness (per side): \t%2.2f um\n',h_final)
fprintf('\t change = %2.2f um\n',delta_h)
fprintf('\nFitting parameters:\n')
fprintf('\t gamma_o = %2.4G um/min   (%2.4G um/s)\n',gamma_0,gamma_0/60)
fprintf('\t tau = %2.3G min   (%2.4G s)\n',burnresult.tau,burnresult.tau*60)
fprintf('\t beta = %2.4G um/min   (%2.4G um/s)\n',beta,beta/60)
fprintf('\t\t\t this is %2.2f%% of gamma_o\n',ratio)
```

```
fprintf('\t t_c = %2.3G min\n',t_c)
fprintf('\nGoodness of fit results:\n')
fprintf('\t R-squared = %2.4f\n',gof2.rsquare)
fprintf('\t standard (RMS) error = %2.4f\n\n',gof2.rmse)
diary off; % stop recording and write diary file

%+++plot fitting result
b = plot(burnresult);
set(b,'LineWidth',1.5)
y_max=a_max*1.1;
YLim([0 y_max]);
box off;                    % turn off tick marks all around graph
hold on
p = plot(fitresult);        % attach handle 'p' to plot
set(p,'LineWidth',1,'LineStyle',':','Color','k');
y_max=a_max*1.1;
YLim([0 y_max]);
box off;                    % turn off tick marks all around graph
legend('\beta = 0','\beta \neq 0',0);
%+++plot raw data for comparison;
L1=line(p_time,p_absorb,'Marker','o','MarkerSize',9,'Color','k',
'LineStyle','none');
xlabel('CVD time [min]', 'FontSize',12);
ylabel('Absorbance @ 488 nm [ - ]','FontSize',12);
ax1 = gca;
set(ax1,'FontSize',12);
ydim = get(ax1,'Ylim');
% adjust thickness axis to correspond to abs. axis
y_upper = ydim(2)*abs_to_thick;
ax2 = axes('Position',get(ax1,'Position'),'XAxisLocation','top','XTick',[],
'YAxisLocation','right','Color','none','XColor','k','YColor','b');
set(ax2,'FontSize',12,'Ylim', [0 y_upper]);
ylabel('VASWNT film thickness [\mum]','FontSize',12);
```

```
%+++output figures
eps_ext = ['.eps']; %eps output with tiff preview for LaTeX
tiff_ext = ['.tif']; %tiff output for images
pdf_ext = ['.pdf']; %pdf output for LaTeX --> pdf
plotname_eps = horzcat(prefix,filename,eps_ext);
print('-f1', '-depsc', '-tiff', plotname_eps);
plotname_tiff = horzcat(prefix,filename,tiff_ext);
print('-f1', '-dtiff', '-r600', plotname_tiff);
plotname_pdf = horzcat(prefix,filename,pdf_ext);
print('-f1', '-dpdf', plotname_pdf);
%end
```

Appendix C

Kramers-Kronig relations

A general response function Φ_{AB} is defined by the *response* of a system to some perturbation $B = h(t)$, where the response is observed by the variable A. If the perturbation is small, the response is linear, and has the form

$$\overline{A(t)} = \langle A \rangle + \int_{-\infty}^{t} \Phi_{AB}(t-t')h(t')dt' = \langle A \rangle + \int_{0}^{\infty} \Phi_{AB}(\tau)h(t-\tau)d\tau. \tag{C.1}$$

The average $\langle A \rangle$ is taken in space, and $\overline{A(t)} = \langle A \rangle$ is the change in A induced by the perturbation $h(t)$. The response at time t is determined by the perturbation acting over the full time interval from $-\infty$ to t. We now consider the Fourier transform of C.1. Since the Fourier transform for a convolution of two functions is the product of the transformed functions, we have

$$\langle A(\omega) \rangle = \Phi_{AB}(\omega)h(\omega) = \chi_{AB}(\omega)h(\omega), \tag{C.2}$$

with

$$\chi_{AB}(\omega) = \frac{\langle A(\omega) \rangle}{h(\omega)} = \int_{0}^{\infty} \Phi_{AB}(t)e^{i\omega t}. \tag{C.3}$$

χ_{AB} is called the *generalized susceptibility*, and is a complex function of the form

$$\chi(\omega) = \chi_{\mathrm{R}}(\omega) + i\chi_{\mathrm{i}}(\omega). \tag{C.4}$$

Note the indices have been dropped for simplicity. From (C.3) it is clear that

$$\chi(-\omega) = \chi^{*}(-\omega). \tag{C.5}$$

Therefore, for the real and imaginary parts of $\chi(\omega)$ we find

$$\chi_{\mathrm{R}}(-\omega) = \chi_{\mathrm{R}}(\omega) \tag{C.6}$$

$$\chi_{\mathrm{i}}(-\omega) = -\chi_{\mathrm{i}}(\omega). \tag{C.7}$$

This shows us that $\chi_{\mathrm{R}}(\omega)$ is an even function, and $\chi_{\mathrm{i}}(\omega)$ an odd function for real values of ω.

The definition of $\chi(\omega)$ (C.3) implies causality between the perturbation of a system and its response. This allows us to derive two very important properties of the linear response functions. We begin by considering the response functions on the complex ω plane $\omega_{\mathrm{R}} + i\omega_{\mathrm{i}}$. The first thing to note is that $\chi(\omega)$ is analytic in the upper half of the complex plane (i.e. has no poles). More importantly, there is a fundamental relationship between the real and imaginary parts of $\chi(\omega)$.

We assume an arbitrary value of $\omega = \omega_0$ and evaluate the integral

$$I = \int_{\mathcal{C}} \frac{\chi(\omega)}{\omega - \omega_0} d\omega, \tag{C.8}$$

where $\mathcal{C}$ is a path taken around an infinite semicircle in the upper half of the complex ω-plane. The pole at $\omega = \omega_0$ is excluded by an infinitely small semicircle along the path (see Fig.C.1). Since $\chi(\omega)$ is analytic along and within the region bounded by $\mathcal{C}$, the value of the integral is zero. The contribution of the remaining infinitely small semicircle around the pole at $\omega = \omega_0$ is $-i\pi\chi(\omega_0)$. Equation C.8 can thus be rewritten in the form

$$I = \lim_{\rho \to 0} \left\{ \int_{-\infty}^{\omega_0 - \rho} \frac{\chi(\omega_{\mathrm{R}})}{\omega_{\mathrm{R}} - \omega_0} d\omega_{\mathrm{R}} + \int_{\omega_0 + \rho}^{\infty} \frac{\chi(\omega_{\mathrm{R}})}{\omega_{\mathrm{R}} - \omega_0} d\omega_{\mathrm{R}} \right\} - i\pi\chi(\omega_0) = 0. \tag{C.9}$$

The expression within the curly brackets is known as the *principal value* $\mathcal{P}$ of the integral from $-\infty$ to ∞. Relabeling ω_{R} as ω, we now have the expression for the complex dispersion relation

$$\chi(\omega_0) = -\frac{i}{\pi} \mathcal{P} \int \frac{\chi(\omega)}{\omega - \omega_0} d\omega. \tag{C.10}$$

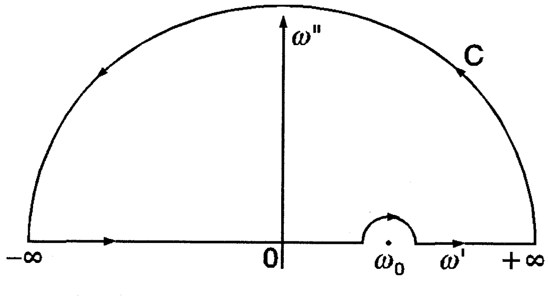

Figure C.1: Contour of the Cauchy principal value integral.

We now separate out the real and imaginary parts of C.10 to obtain the *Kramers-Kronig relations*

$$\chi_{\mathrm{R}}(\omega) = \frac{1}{\pi}\mathcal{P}\int \frac{\chi_{\mathrm{i}}(\omega)}{\omega - \omega_0} d\omega \tag{C.11}$$

$$\chi_{\mathrm{i}}(\omega) = -\frac{1}{\pi}P\int \frac{\chi_{\mathrm{R}}(\omega)}{\omega - \omega_0} d\omega \tag{C.12}$$

These relations enable us to find the real part of the response of a linear passive system if we know the imaginary part of the response at all frequencies, and vice-versa. They are central to the analysis of optical experiments on solids.

Bibliography

[1] H. W. Kroto, J. R. Heath, S. C. O'Brien, R. F. Curl, R. E. Smalley, C_{60}: Buckminsterfullerene, Nature 318 (1985) 162–163.

[2] S. Iijima, T. Ichihashi, Single-shell carbon nanotubes of 1-nm diameter, Nature 363 (1993) 603–605.

[3] D. S. Bethune, C. H. Kiang, M. S. D. Vries, G. Gorman, R. Savoy, J. Vasquez, R. Beyers, Cobalt-catalysed growth of carbon nanotubes with single-atomic-layer walls, Nature 363 (1993) 605–606.

[4] S. Iijima, Helical microtubules of graphitic carbon, Nature 354 (1991) 56–58.

[5] A. Oberlin, M. Endo, T. Koyama, Filamentous growth of carbon through benzene decomposition, J. Cryst. Growth 32 (1976) 335–349.

[6] R. Saito, G. Dresselhaus, M. S. Dresselhaus, Physical Properties of Carbon Nanotubes, Imperial College Press, London, 1998.

[7] M. S. Dresselhaus, G. Dresselhaus, P. Avouris, Carbon Nanotubes: Synthesis, Structure, Properties, and Applications, Vol. 80, Springer, Berlin, 2001.

[8] S. Reich, C. Thomsen, J. Maultzsch, Carbon Nanotubes: Basic Concepts and Physical Properties, Wiley, 2004.

[9] L. C. Venema, J. W. G. Wildöer, C. Dekker, G. A. Rinzler, R. E. Smalley, STM atomic resolution images of single-wall carbon nanotubes, Appl. Phys. A 66 (1998) S153–S155.

[10] J. W. G. Wildöer, L. C. Venema, A. G. Rinzler, R. E. Smalley, C. Dekker, Electronic structure of atomically resolved carbon nanotubes, Nature 391 (1998) 59–62.

[11] T. W. Odom, J.-L. Huang, P. Kim, C. Lieber, Atomic structure and electronic properties of single-walled carbon nanotubes, Nature 391 (1998) 62–64.

[12] G. G. Samsonidze, R. Saito, A. Jorio, M. A. Pimenta, A. G. S. Filho, A. Grüneis, G. Dresselhaus, M. S. Dresselhaus, The concept of cutting lines in carbon nanotube science, J. Nanosci. Nanotechnol. 3 (2003) 431–458.

[13] R. Saito, A. Grüneis, G. G. Samsonidze, G. Dresselhaus, M. S. Dresselhaus, A. Jorio, L. G. Cançado, M. A. Pimenta, A. G. S. Filho, Optical absorption of graphite and single-wall carbon nanotubes, Appl. Phys. A 78 (2004) 1099–1105.

[14] H. Ajiki, T. Ando, Aharonov-Bohm effect in carbon nanotubes, Physica B 201 (1994) 349–352.

[15] H. Kuzmany, Solid-State Spectroscopy: An Introduction, Springer, 2006.

[16] H. Kuzmany, M. Hulman, R. Pfeiffer, F. Simon, Raman scattering of carbon nanotubes, in: Carbon Nanotubes, V. N. Popov and P. Lambin (Eds.), Springer, 2006.

[17] S. Chiashi, Single-walled carbon nanotube synthesis in an environmental AFM and in situ Raman spectroscopy (in Japanese), Ph.D. thesis, The University of Tokyo (2005).

[18] M. S. Dresselhaus, P. C. Eklund, Phonons in carbon nanotubes, Adv. in Phys. 49 (2000) 705–814.

[19] M. Lazzeri, S. Piscanec, F. Mauri, A. C. Ferrari, J. Robertson, Phonon linewidths and electron-phonon coupling in graphite and nanotubes, Phys. Rev. B 73 (2006) 155426.

[20] V. N. Popov, P. Lambin, Radius and chirality dependence of the radial breathing mode of the G-band phonon modes of single-walled carbon nanotubes, Phys. Rev. B 73 (2006) 085407.

[21] Y. Kawashima, G. Katagiri, Observation of the out-of-plane mode in the Raman scattering from the graphite edge plane, Phys. Rev. B 59 (1999) 62–64.

[22] S. Bandow, T. Hiraoka, T. Yumura, K. Hirahara, H. Shinohara, S. Iijima, Raman scattering study on fullerene derived intermediates formed within single-wall carbon nanotube: from peapod to double-wall carbon nanotube, Chem. Phys. Lett. 384 (2004) 320–325.

[23] P. T. Araujo, S. K. Doorn, S. Kilina, S. Tretiak, E. Einarsson, S. Maruyama, H. Chacham, M. A. Pimenta, A. Jorio, Third and fourth optical transitions in semiconducting carbon nanotubes, Phys. Rev. Lett. 98 (2007) 067401.

[24] A. Grüneis, R. Saito, J. Jiang, G. G. Samsonidze, M. A. Pimenta, A. Jorio, A. G. S. Filho, G. Dresselhaus, M. S. Dresselhaus, Resonant Raman spectra of carbon nanotube bundles observed by perpendicularly polarized light, Chem. Phys. Lett. 387 (2004) 301–306.

[25] Y. Murakami, S. Chiashi, E. Einarsson, S. Maruyama, Polarization dependence of resonant Raman scatterings from vertically aligned SWNT films, Phys. Rev. B 71 (2005) 085403.

[26] S. Maruyama, R. Kojima, Y. Miyauchi, S. Chiashi, M. Kohno, Low-temperature synthesis of high-purity single-walled carbon nanotubes from alcohol, Chem. Phys. Lett. 360 (2002) 229–234.

[27] C. Journet, W. K. Maser, P. Bernier, A. Loiseau, M. L. de la Chapelle, S. Lefrant, P. Deniard, R. Lee, J. E. Fischer, Large-scale production of single-walled carbon nanotubes by the electric-arc technique, Nature 388 (1997) 756–758.

[28] A. Thess, R. Lee, P. Nikolaev, H. Dai, P. Petit, J. Robert, C. Xu, Y. H. Lee, S. G. Kim, A. G. Rinzler, D. T. Colbert, G. E. Scuseria, D. Tomànek, J. E. Fischer, R. E. Smalley, Crystalline ropes of metallic carbon nanotubes, Science 273 (1996) 483–487.

[29] H. Dai, A. G. Rinzler, P. Nikolaev, A. Thess, D. T. Colbert, R. E. Smalley, Single-wall nanotubes produced by metal-catalyzed disproportionation of carbon monoxide, Chem. Phys. Lett. 260 (1996) 471–475.

[30] P. Nikolaev, M. J. Bronikowski, R. K. Bradley, F. Rohmund, D. T. Colbert, K. A. Smith, R. E. Smalley, Gas-phase catalytic growth of single-walled carbon nanotubes from carbon monoxide, Chem. Phys. Lett. 313 (1999) 91–97.

[31] Y. Murakami, S. Chiashi, Y. Miyauchi, M. Hu, M. Ogura, T. Okubo, S. Maruyama, Growth of vertically aligned single-walled carbon nanotube films on quartz substrates and their optical anisotropy, Chem. Phys. Lett. 385 (2004) 298–303.

[32] Y. Murakami, Y. Miyauchi, S. Chiashi, S. Maruyama, Characterization of single-walled carbon nanotubes catalytically synthesized from alcohol, Chem. Phys. Lett. 374 (2003) 53–58.

[33] Y. Shibuta, S. Maruyama, Molecular dynamics simulation of formation process of single-walled carbon nanotubes by CCVD method, Chem. Phys. Lett. 382 (2003) 381–386.

[34] Y. Murakami, Y. Miyauchi, S. Chiashi, S. Maruyama, Direct synthesis of high-quality single-walled carbon nanotubes on silicon and quartz substrates, Chem. Phys. Lett. 377 (2003) 49–54.

[35] M. Hu, Y. Murakami, M. Ogura, S. Maruyama, T. Okubo, Morphology and chemical state of Co-Mo catalysts for growth of single-walled carbon nanotubes vertically aligned on quartz substrates, J. Catal. 225 (2004) 230–239.

[36] Y. Homma, Y. Kobayashi, T. Ogino, D. Takagi, R. Ito, Y. J. Jung, P. M. Ajayan, Role of transition metal catalysts in single-walled carbon nanotube growth in chemical vapor deposition, J. Phys. Chem. B 44 (2003) 12161–12164.

[37] Y. Murakami, E. Einarsson, T. Edamura, S. Maruyama, Polarization dependent optical absorption properties of single-walled carbon nanotubes and methodology for the evaluation of their morphology, Carbon 43 (2005) 2664–2676.

[38] T. de los Arcos, F. Vonau, M. G. Garnier, V. Thommen, H. G. Boyen, P. Oelhafen, M. Düggelin, D. Mathis, R. Guggenheim, Influence of iron-silicon interaction on the growth of carbon nanotubes by chemical vapor deposition, Appl. Phys. Lett. 80 (2002) 2383–2385.

[39] S. Maruyama, E. Einarsson, Y. Murakami, T. Edamura, Growth process of vertically aligned single-walled carbon nanotubes, Chem. Phys. Lett. 403 (2005) 320–323.

[40] Y. Murakami, CVD growth of single-walled carbon nanotubes and their anisotropic optical properties, Ph.D. thesis, The University of Tokyo (2005).
URL `www.photon.t.u-tokyo.ac.jp/thesis/2005/2005murakami.pdf`

[41] Y. Murakami, S. Maruyama, Evidence for root growth of vertically aligned single-walled carbon nanotube films determined by XPS analysis, to be submitted.

[42] G. Zhong, T. Iwasaki, K. Honda, Y. Furukawa, I. Ohdomari, H. Kawarada, Very high yield of vertically aligned single-walled carbon nanotubes by point-arc microwave plasma CVD, Chem. Vap. Dep. 11 (2005) 127–130.

[43] D. N. Futaba, K. Hata, T. Yamada, K. Mizuno, M. Yumura, S. Iijima, Kinetics of water-assisted single-walled carbon nanotube synthesis revealed by a time-evolution analysis, Phys. Rev. Lett. 95 (2005) 056104.

[44] Y. Murakami, E. Einarsson, T. Edamura, S. Maruyama, Polarization dependence of the optical absorption of single-walled carbon nanotubes, Phys. Rev. Lett. 94 (2005) 087402.

[45] T. Ando, Physics of Carbon Nanotubes, Springer, Berlin, 2003.

[46] J. Jiang, R. Saito, A. Grüneis, G. Dresselhaus, M. S. Dresselhaus, Optical absorption matrix elements in single-wall carbon nanotubes, Carbon 42 (2004) 3169–3176.

[47] H. Kataura, Y. Kumazawa, Y. Maniwa, I. Umezu, S. Suzuki, Y. Ohtsuka, Y. Achiba, Optical properties of single-wall carbon nanotubes, Synth. Met. 103 (1999) 2555–2558.

[48] T. Pichler, M. Knupfer, M. S. Golden, J. Fink, A. Rinzler, R. E. Smalley, Localized and delocalized electronic states in single-wall carbon nanotubes, Phys. Rev. Lett. 80 (1998) 4729–4732.

[49] A. G. Marinopoulos, L. Reining, A. Rubio, N. Vast, Optical and loss spectra of carbon nanotubes: Depolarization effects and intertube interactions, Phys. Rev. Lett. 91 (2003) 046402.

[50] B. W. Reed, M. Sarikaya, Electronic properties of carbon nanotubes by transmission electron energy-loss spectroscopy, Phys. Rev. B 64 (2001) 195404.

[51] R. Kuzuo, M. Terauchi, M. Tanaka, Electron energy-loss spectra of carbon nanotubes, Jpn. J. Appl. Phys. 31 (1992) L1484 – L1487.

[52] J. R. Lakowicz, Principles of Fluorescence Spectroscopy, Plenum Publishing Corp., New York, 1999.

[53] M. F. Islam, D. E. Milkia, C. L. Kane, A. G. Yodh, J. M. Kikkawa, Direct measurement of the polarized optical absorption cross section of single-wall carbon nanotubes, Phys. Rev. Lett. 93 (2004) 037404.

[54] H. A. Haus, Mode-locking of lasers, J. on Select. Top. in Quantum Electron. 6 (2000) 1173–1185.

[55] S. Y. Set, H. Yaguchi, Y. Tanaka, M. Jablonski, Ultrafast fiber pulsed lasers incorporating carbon nanotubes, J. on Select. Top. in Quantum Electron. 10 (2004) 137–146.

[56] Y.-W. Song, C. S. Goh, S. Y. Set, K. H. Fong, S. Yamasita, Enhanced passive mode-locking of fiber lasers using carbon nanotubes deposited onto D-shaped fiber, Vol. Proceedings, Optical Fiber Communication Conference / National Fiber Optic Engineers Conference, 2006, pp. 3–4.

[57] Y.-W. Song, S. Yamashita, E. Einarsson, S. Maruyama, All-fiber pulsed lasers passively mode-locked by transferable vertically aligned carbon nanotube film, submitted (2007).

[58] J. Stöhr, D. A. Outka, Determination of molecular orientations on surfaces from the angular dependence of near-edge X-ray-absorption fine-structure spectra, Phys. Rev. B 36 (1987) 7891–7905.

[59] W. Schattke, M. A. V. Hove, Solid-State Photoemission and Related Methods: Theory and Experiment, Wiley, 2003.

[60] S. Hüfner, Photoelectron Spectroscopy, Springer, Berlin, 1995.

[61] M. Bockrath, D. H. Cobden, J. Lu, A. G. Rinzler, R. E. Smalley, L. Balents, P. L. McEuen, Luttinger-liquid behaviour in carbon nanotubes, Nature 397 (1999) 598–601.

[62] J. Voit, A brief introduction to Luttinger liquids, cond-mat 1 (2000) 0005114.

[63] H. Ishii, H. Kataura, H. Shiozawa, H. Yoshioka, H. Otsubo, Y. Takayama, T. Miyahara, S. Suzuki, Y. Achiba, M. Nakatake, T. Narimura, M. Higashiguchi, K. Shimada, H. Namatame, M. Taniguchi, Direct observation of Tomonaga-Luttinger-liquid state in carbon nanotubes at low temp, Nature 426 (2003) 540–544.

[64] H. Rauf, T. Pichler, M. Knupfer, J. Fink, H. Kataura, Transition from a Tomonaga-Luttinger liquid to a Fermi liquid in potassium-intercalated bundles of single-wall carbon nanotubes, Phys. Rev. Lett. 93 (2004) 096805.

[65] J. Fink, P. Lambin, Electron spectroscopy studies of carbon nanotubes, in: Carbon Nanotubes: Synthesis, Structure, Properties, and Applications M. S. Dresselhaus and G. Dresselhaus and Ph. Avouris (Eds.), Springer-Verlag, 2001.

[66] J. Fink, Recent development in energy-loss spectroscopy, Adv. Electron. Electron Phys. 75 (1989) 121.

[67] Y. Murakami, S. Maruyama, Detachment of vertically aligned single-walled carbon nanotube films from substrates and their re-attachment to arbitrary surfaces, Chem. Phys. Lett. 422 (2006) 575–580.

[68] D. N. Futaba, K. Hata, T. Yamada, T. Hiraoka, Y. Hayamizu, Y. Kakudate, O. Tanaike, H. Hatori, M. Yumura, S. Iijima, Shape-engineerable and highly densely packed single-walled carbon nanotubes and their applications as super-capacitor electrodes, Nature Mater. 5 (2006) 987–994.

[69] X. Liu, T. Pichler, M. Knupfer, M. S. Golden, J. Fink, D. A. Walters, M. J. Casavant, J. Schmidt, R. E. Smalley, An electron-loss study of the structural and electronic properties of magnetically aligned single wall carbon nanotubes, Synth. Met. 121 (2001) 1183–1186.

[70] B. W. Smith, Z. Benes, D. E. Luzzi, D. A. Walters, M. J. Casavant, J. Schmidt, R. E. Smalley, J. E. Fischer, Structural anisotropy of magnetically aligned single wall carbon nanotube films, Appl. Phys. Lett. 77 (2000) 663–665.

[71] S. Rols, A. Righi, L. Alvarez, E. Anglaret, R. Almairac, C. Journet, P. Bernier, L. J. Sauvajol, A. M. Benito, W. K. Maser, E. M. noz, M. T. Martinez, G. F. de la Fuente, A. Girard, J. C. Ameline, Diameter distribution of single wall carbon nanotubes in nanobundles, Eur. Phys. J. B 18 (2000) 201–205.

[72] L. Henrad, E. Hernández, P. Bernier, A. Rubio, van der Waals interaction in nanotube bundles: Consequence on vibrational modes, Phys. Rev. B 60 (1999) R8521.

[73] K. H. An, C.-M. Yang, J. S. Park, S. Y. Jeong, Y. H. Lee, Intercalant-induced superbundle formation of single-wall carbon nanotubes, J. Phys. Chem. B 109 (2005) 10004–10008.